UNIVERSITY OF CALIFORNIA
RIVERSIDE

Theoretical Insight Towards Uranium Extraction from Seawater

A Dissertation submitted in partial satisfaction
of the requirements for the degree of

Doctor of Philosophy

in

Chemistry

by

Chad Wheeler Priest

June 2018

Dissertation Committee:

Dr. De-en Jiang, Chairperson
Dr. Gregory Beran
Dr. Ming Lee Tang

The Dissertation of Chad Wheeler Priest is approved:

_____

_____

_____

Committee Chairperson

University of California, Riverside

Acknowledgement of Copyright

Acknowledgements

To all of you who have helped me grow into an accomplished scientist I want to give acknowledgement. I have been very fortunate to have been obliged by the many support and the good fortunes of my academic mentors, fellow family, friends, and lab-mates through this notable journey.

I want to first thank my PI, Dr. De-en Jiang, for his support and guidance through this journey. Also, Dr. Jingsong Zhang helping me explore the field of chemistry. Thank you Dr. Gregory Beran for always being easy-going, personable, and great committee member. Thank you to the many professors who inspired me at the University California, San Diego (UCSD), Dr. David Hendrickson, Dr. Lindenberg, Dr. George Anderson, and Dr. Pomeroy.

Consuelo, I love you very much and thank you for believing in me! Dr. Ziqi Tian, I really, want to give an immense THANK YOU for being a really good friend. Also, I want to thank my dogs, Lily, Ollie, and Betty for their constant love, I will see you when I get home. Finally, a big thanks to the University of California, Riverside (UCR), for their continual support through my entire Ph. D. career.

ABSTRACT OF THE DISSERTATION

Theoretical Insight Towards Uranium Extraction from Seawater

by

Chad Wheeler Priest

Doctor of Philosophy, Graduate Program in Chemistry
University of California, Riverside, June 2018
Dr. De-en Jiang, Chairperson

Uranium's economical consumption is based on the industrial nuclear fuel cycle. Today there remains 4-6 million tons of terrestrial uranium in Earth's ores. However, as the projected population is estimated to double by 2040, current uranium reserves are only estimated to provide nuclear fuel for the next century. Unconventional methods for acquiring uranium are, therefore, required to maintain longevity and sustainability for future economic nuclear energy demands.

One unconventional alternative for mining uranium is diving from land and into the open seas. Although uranium resides uniformly in the oceans at very low concentrations of 3.3 ppb, in a vast body of Earths water, there exists an untapped reserve of uranium at an astounding 4.5 billion ton. Uranium exists in aqueous environment as the stable oxo-cation, in the hexavalent (VI) state called uranyl, UO_2^{2+}, and as the neutral ternary-uranyl-carbonato, $Ca_2UO_2(CO_3)_3$, in seawater.

After six generations of research and development, current extraction methods rely on a polymer grafter amidoxime-based (poly(AO)) material for uranium recovery from seawater. One chemical advancement in adsorption capacity is from the inclusion the hydrophilic group carboxylate (Ac). However, displacing coordinating carbonates with poly(amidoxime) from uranyl, which is both at low concentrations and existing in soup of various metal-ions in a seawater matrix, still remains a formidable challenge. One of the multifaceted efforts involved with increasing adsorption selectivity is by the theoretical insight into uranium's coordination chemistry with interacting ligands in seawater-related environments.

Herein we utilize current state-of-the-art, advanced computing technology to investigate coordinating uranium species in a completely explicit model. First, we employ a pure quantum mechanical (QM) simulations to pry into the chemistry of surrounding water molecules' influence on the dominant $Ca_2[UO_2(CO_3)_3]$ specie. Furthermore, large scale classical molecular dynamics (CMD) simulations are assisted with umbrella sampling to develop computational techniques for investigating coordinating uranyl-AO from calculating binding free-energies (ΔG_{bind}). Furthermore, we investigate the influence of capacity by inspecting the interactions of mix-ligand containing AO/Ac. Additionally, employing umbrella sampling method coupled with WHAM, we investigate the sodium ion solvation environment of one of the most competing vanadium-containing species, HVO_4^{2-}.

Table of Contents

Chapter Four:

LIST OF FIGURES

LIST OF TABLES

CHAPTER ONE

Introduction

1.1 Overview

The general focus of this thesis is on theoretical insight to uranium seawater recovery. Coordinated metal species are investigated utilizing an explicit aqueous model for seawater related environments from the perspective of quantum molecular dynamics (QMD) and classical mechanical dynamics (CMD). The direction considers exploring uranium/vanadium solvation influence on related coordinated metal species in seawater relevant conditions. Chapter 1 sets the foundation of the overall work by introducing the nuclear fuel cycle with regard to conventional uranium-mining methods, unconventional seawater mining, and challenges presented in mining uranium from seawater. Chapter 2 provides background and theory to computational methods utilized in this work from basic QM-MD to CMD background, along with background and formalism of post-processing methods. The thesis begins in Chapter 3 with a pure QM –based molecular dynamic, DFT-MD, to explore the solvation influence of the dominant uranium specie $Ca_2[UO_2(CO_3)_3]$ in explicit water. Chapter 4 then explores coordinating uranyl with amidoxime-type (AO) ligands utilizing CMD assisted umbrella sampling to calculate and compare binding free-energy of coordinating AO-type ligands. Chapter 5 takes a step further in ligand model designs by constructing a bifunctional ligand by including a carboxylate functional group.

A combination of CMD and DFT-MD is employed to investigate solvation influence and relative stability of coordinating uranyl-bifunctional ligand using a 1:1 ratio. Chapter 6 divulges theoretical insight to the complicated network of solvating sodium-ions and water around HVO_4^{2-} specie in water and seawater conditions. Vanadium is known to bind competitively with current poly(AO) material. Chapter 7 explores technetium to understand the nanocluster evolution, Tc_n (n = 4-20). Chapter 8 summarizes the conclusions and proposes future work.

1.2 Terrestrial Uranium: Mining and Reserves

Uranium's economical reserves depends on the nuclear fuel cycle, which consists of mining, refinement, purification, enrichment, employment, and disposal and restoration. Uranium, which has the shorthand electron configuration of [Rn] $5f^3$ $6d^1$ $7s^2$, resides in terrestrial ores as uranium oxide (uranite) with the chemical formula U_3O_8. It exists as multi-valent states of U(V) and U(VI). Two radioactive isotopes exist as ores, with U-238 having a percent abundance of 99.27%, and U-235 having a percent abundance of 0.73%. Contemporary terrestrial mining comprises of different techniques such as underground mining, open-pit, heap leaching, and in-situ leeching.

Nuclear reactors that utilize natural uranium as U_3O_8 concentrate need to refine and convert this directly to uranium dioxide ($^{235}U(VI)O_2^{2+}$) before usage. Once uranium oxide has been mined it is transported to a plant for milling and refining in order to prepare a uranium oxide powder concentrate called, "yellow cake". After "yellow cake" is formed, it is transferred to a conversion plant to be further purified and converted to UF_6. The UF_6 is then sent to an enrichment facility where the two main radio isotopes U(VI)-235 and

U(VI)-238 are separated by one of either two isotope isolation methods: gaseous diffusion or gas centrifugation. Once 235-U(VI)F_6 is enriched, the material is transported to a reconversion plant to be chemically converted to U(VI)O_2. In the last step, enriched uranium is converted to fuel in a fuel fabrication plant. In this process, U-235 is prepared as a powder and pressed sintered into ceramic form or pellets for usage.

Terrestrial uranium is a limited resource existing at approximately 4-6 million metric tons. Nuclear fuel is a rising source that is currently nourishing 11% of the global electrical grid outputted from 450 power reactors.[1] However, it is estimated the world energy consumption will increase 56% by 2050.[2] This estimates terrestrial reserves at current rates of consumption will deplete in the next 80 – 120 years.

1.3 Mining Uranium from Seawater

To sustain the current and future global energy consumptions and demands for nuclear energy, alternate reserves need to be considered. The next best uranium reserve is going from land to sea. Quantitatively, uranyl resides in the open sea conservatively or uniformly at a low concentration of 3.3 μg L^{-1}.[3] Although it exists at very minute concentrations, an astounding 4.4 billion tons remain untapped. For this reason, scientists have been motivated to research alternate mining methods for sustaining reserves of nuclear energy for future economic longevity and prosperity.

Uranium extraction from seawater is not a new concept. In fact, uranium recovery from seawater has been an off-and-on practice for about the past six decades. The attraction to this method of mining was fomented in the 1960s when Davis et al. estimated the overwhelming and enticing amount of uranium in the Earth's oceans.[3] Since then, many

extraction methods have been studied, such as ionic-liquid methods, ion-exchange methods, hydrogels, chitin-based materials and metal-oxides. Among the early adsorbent materials studied, inorganic-based adsorbents were the dominant extraction method, such as titanium oxide. Although these showed promising adsorption performance, they lacked structural integrity or mechanical strength upon usage.[4] It wasn't until the 1980s when a Japanese group discovered that amidoxime-functionalized, resin-based adsorbents showed superior relative performance in simulated and marine aqueous environments.[5,6] Even after screening more than 200 functionalized adsorbents amidoxime (AO) group, RC(-NH_2)(=NOH), showed highly selective towards uranium.[7, 8]

1.4 Uranium's Seawater Composition

In aqueous solution, uranium exists as a linearly stable oxo-cation form, UO_2^{2+}(aq), bearing a hexavalent state U(VI) or U(VI) called, uranyl. UO_2^{2+} has been experimentally and computationally studied in aqueous solution, and studies have demonstrated uranyl ion exist as a symmetrical and linear specie.[9,10] It was once believed that uranyl existed as a stable anionic $[UO_2(CO_3)_3]^{4-}$ complex ion in seawater.[11,12] However, seminal work by Bernhard et al. shifted the consensus by providing spectroscopic experimental evidence that suggested the existence of the neutral $Ca_2[UO_2(CO_3)_3]$.[13,14] Most recently, utilizing calcium selective electrode potentiometry and optical absorption spectrophotometry experimental methods, Ebdrizzi et al. provided equilibrium constants for Ca and Mg complexation with $[UO_2(CO_3)_3]^{4-}$.[15] Their calculated binding constants provide thermochemical perspective calculations that illustrate 90% of the dissolved uranium is mainly coordinated as the neutral $Ca_2[UO_2(CO_3)_3]$, followed by $Ca/Mg[UO_2(CO_3)_3]^{2-}$.

From this, Chapter 1 pries into the electrostatic of surrounding waters effect on the dominant $Ca_2[UO_2(CO_3)_3]$ from the pure perspective of ab initio calculations.[16] It is noteworthy that elucidating the dominant uranium's composition in seawater pushes the direction of research and design because it depicts the chemistry needed mechanistic for displacement of calcium and coordinating carbonate ligands.

1.5 Computational Ligand Design

Amidoxime-based polymers can be chemically synthesized by two methods: Radiation induced graft polymerization (RIGP) and atoms transfer radical polymerization (ATRP). RIGP is the oldest polymeric fabrication method, being used since the 1980s.[17] The general process can be separated into four steps: i) production of radicals on polymer fibers (i.e. polyethylene) through radiation (electron beam); ii) grafting of monomers; iii) ligand conversion; and iv) conditioning with alkaline treatment to regenerate the polymer. Both polymer preparation methods are graft with commoners acrylonitrile and hydrophilic acids, like carboxylate ($R\text{-}CO_2^-$).[18] Studies have shown hydrophilic groups enhance uranium capacity and uptake. This is probably because the inclusion of hydrophilic functional groups swells polymer fibers by coulombic interaction of neighboring carboxylate functional groups.[19, 20] State-of-the-art methods are designed to perform with optimal AO/Ac ratios. Nonetheless, the strategy for designing simulation models need to require AO-type with and without the inclusion of carboxylate (Ac) functional based ligands to understand their relative uranyl-ligand coordination in seawater related conditions.

Upon grafting AO-functionals onto a polyethylene polymer fibers, open-chain and cyclic structures can be formed. The "open-form" has been modeled experimentally with a small molecule, glutardiamidoxime.[21] It has two AO functional groups AO-$(CH_2)_3$-AO. The "cyclic form" has also been studied experimentally with glutarimidoxime molecules. It is shown in Figure 1.1 as the tridentate binding mode (HA^-). The binding of the cyclic form and its relative stability has been studied both experimentally and computationally.[21,22] Between the two forms, the cyclic has been shown to exhibit the strongest binding affinity.[21,23] There exists more controversy over the Uranyl-AO-open than the Uranyl-AO-cyclic because the open-chain binding modes are more complicated. In this thesis Chapter 3 utilizes various computational methods to explore coordination and solvation of uranyl-AO open-type by utilizing classical molecular dynamics assisted umbrella sampling.[24] This computational method is pragmatic method for comparing relative binding strengths towards ligand rational for efficient uranium selectivity.

Coordinating uranyl-AO type ligands, like the open-chain, have been shown to exhibit various types of binding modes. Figure 1.1 illustrates the different type of binding modes along with their unconventional names. The first binding mode shows an eta1 (η^1) type of binding, also known as the monodentate binding mode. In this binding mode the oxime-oxygen singly binds to uranium of the uranyl. The second type of binding mode is called eta2 (η^2), where the simultaneous binding of the oxime-nitrogen and oxime-oxygen bind to uranium of the uranyl specie along the plane (Figure 1.1). Continually, amidoxime has been suggested to bind through a kappa_2 (κ^2) binding motif, where the amine functional groups binding simultaneously with the oxime-oxygen to uranyl (Figure 1.1).

Lastly, a cyclic form has been seen to interact strongly to the uranyl specie which interacts through a two-fold oxime-oxygen binding along with a single imide bond.[25] Amidoxime oxygens have a relatively large pK_a of 13, suggesting the occurrence of the removal or deprotonation of oxime-oxygen to occur posteriorly amid binding in seawater pH conditions. However, many approximations can be made by assuming the formation of amidoximate ($-C=N-O^-$) structure. Chapters 3 and 4 illustrates suggested binding modes.[24]

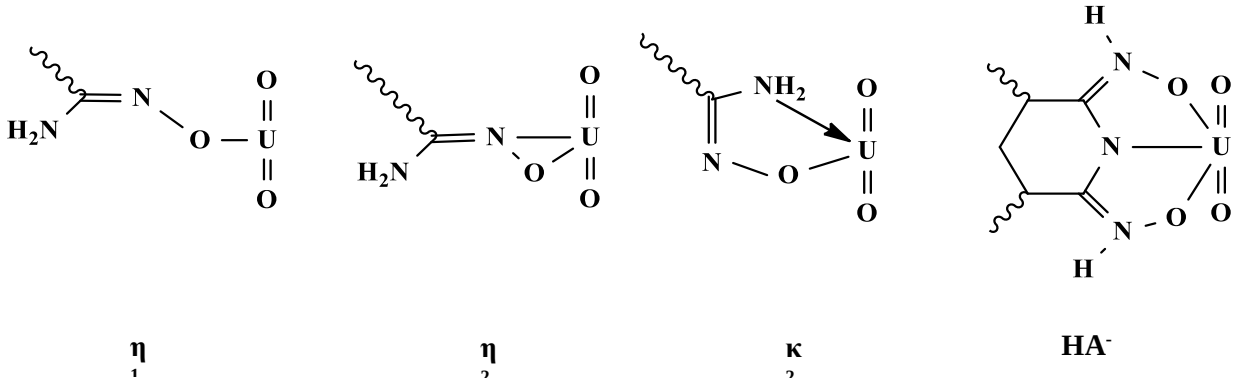

Figure 1.1 Are illustrations of the different types of binding modes for amidoxime and uranyl.

1.6 Challenges

In order for uranium extraction from seawater to be a viable alternative or commercially feasible it must be cost competitive with current terrestrial methods. Today, terrestrial uranium fluctuates above and below market price between 45-160$ per kg of uranium while seawater extraction is around 400 - 500$/kg of uranium.[26]

Even after six decades on the research topic, the endeavor remains an immense challenge. Many of the challenges arise due to the innate complexity of seawater containing many chemical ions at various concentrations coupled with the sparse concentration of uranium that resides within the waters. Seawater is vast, containing a soup of various types of ions at relatively higher or low concentrations compared to uranium. Adsorbing many superfluous ions impedes uranium adsorption sites, which decreases adsorption capacity. Among the many ions, vanadium remains the strongest adsorbing metal-ion, so much that it can irreversibly destroy polymer integrity for reuse. Chapter 6 explores one of the dominant vanadium species solvation in pure water and seawater related environments.[27] Additional challenges include the fact that seawaters contain a large amount of bio-marine living organisms (algae), which can interfere with uranium adsorption. Seawater complexity, such as its pH (8.0 – 8.3), temperature fluctuations, salinity, trace and abundant elements, also presents a challenge. Furthermore, the calcium and carbonate ions in $Ca_2[UO_2(CO_3)_3]$ all need to be displaced, which is also challenging due to the high concentrations of each of these ions in seawater.

1.7 Conclusion

This work utilizes the combination of quantum-based calculations and classical molecular dynamic (CMD) to explore uranium systems in gas-phase, pure water, and seawater related environments to investigate water effects on the dominant uranium specie and the uranyl-ligand complex. DFT perspective is utilized to investigate water effects on calcium binding on the ternary uranium complex, $Ca_2[UO_2(CO_3)_3]$. CMD assisted umbrella sampling is used to devise a method for exploring relative binding strengths of AO-type ligands, as well as to explore metal-ion interactions with seawater related species like HVO_4^{2-}. Finally, related to the nuclear fuel cycle, technetium nanostructure evolution properties are explored by using a global minimization technique called Basin-hopping.

1.8 References

1. Association, W. N. Nuclear Power in the World Today.

2. Tvehlov, Y. Energy, electricity, and nuclear power estimates for the period up to 2020; Nuclear power reactors in the world. 2002.

3. Davies, R. V.; Kennedy, J.; Hill, K. M.; Mcilroy, R. W.; Spence, R. Extraction of Uranium from Sea Water. Nature 1964, 203 (495), 1110-& DOI: Doi 10.1038/2031110a0.

4. Rodman, M. R. G., L.I.; Chen, A.C.T. Extraction of uranium from seawater: evaluation of uranium resources and plant siting. 1979, DOI: doi:10.2172/6191296.

5. Egawa, H.; Harada, H. Recovery of Uranium from Sea-Water by Using Chelating Resins Containing Amidoxime Groups. Nippon Kagaku Kaishi 1979, (7), 958-959 DOI: DOI 10.1246/nikkashi.1979.958.

6. Egawa, H.; Harada, H.; Shuto, T. Studies on Selective Adsorption Resins .13. Recovery of Uranium from Sea-Water by the Use of Chelating Resins Containing Amidoxime Groups. Nippon Kagaku Kaishi 1980, (11), 1773-1776 DOI: DOI 10.1246/nikkashi.1980.1773.

7. Astheimer, L.; Schenk, H. J.; Witte, E. G.; Schwochau, K. Development of Sorbers for the Recovery of Uranium from Seawater .2. The Accumulation of Uranium from Seawater by Resins Containing Amidoxime and Imidoxime Functional-Groups. Sep Sci Technol 1983, 18 (4), 307-339 DOI: Doi 10.1080/01496398308068568.

8. Schenk, H. J.; Astheimer, L.; Witte, E. G.; Schwochau, K. Development of Sorbers for the Recovery of Uranium from Seawater .1. Assessment of Key Parameters and Screening Studies of Sorber Materials. Sep Sci Technol 1982, 17 (11), 1293-1308 DOI: Doi 10.1080/01496398208056103.

9. Buhl, M.; Wipff, G. Insights into Uranyl Chemistry from Molecular Dynamics Simulations. Chemphyschem 2011, 12 (17), 3095-3105 DOI: 10.1002/cphc.201100458.

10. Jones, L. H.; Penneman, R. A. Infrared Spectra and Structure of Uranyl and Transuranium (V) and (Vi) Ions in Aqueous Perchloric Acid Solution. J Chem Phys 1953, 21 (3), 542-544 DOI: Doi 10.1063/1.1698941.

11. Cinneide, S. O.; Scanlan, J. P.; Hynes, M. J. Equilibria in Uranyl Carbonate Systems .1. Overall Stability Constant of Uo2(Co3)34-. J Inorg Nucl Chem 1975, 37 (4), 1013-1018 DOI: Doi 10.1016/0022-1902(75)80689-0.

12. Scanlan, J. P. Equilibria in Uranyl Carbonate Systems .2. Overall Stability Constant of Uo2(Co3)22- and 3rd Formation Constant of Uo2(Co3)34-. J Inorg Nucl Chem 1977, 39 (4), 635-639 DOI: Doi 10.1016/0022-1902(77)80578-2.

13. Bernhard, G.; Geipel, G.; Brendler, V.; Nitsche, H. Speciation of uranium in seepage waters of a mine tailing pile studied by time-resolved laser-induced fluorescence spectroscopy (TRLFS). Radiochim Acta 1996, 74, 87-91.

14. Bernhard, G.; Geipel, G.; Reich, T.; Brendler, V.; Amayri, S.; Nitsche, H. Uranyl(VI) carbonate complex formation: Validation of the Ca2UO2(CO3)(3)(aq.) species. Radiochim Acta 2001, 89 (8), 511-518 DOI: DOI 10.1524/ract.2001.89.8.511.

15. Endrizzi, F.; Rao, L. F. Chemical Speciation of Uranium(VI) in Marine Environments: Complexation of Calcium and Magnesium Ions with [(UO2)(CO3)(3)](4-) and the Effect on the Extraction of Uranium from Seawater. Chem-Eur J 2014, 20 (44), 14499-14506 DOI: 10.1002/chem.201403262.

16. Priest, C.; Tian, Z. Q.; Jiang, D. E. First-principles molecular dynamics simulation of the Ca2UO2(CO3)(3) complex in water. Dalton T 2016, 45 (24), 9812-9819 DOI: 10.1039/c5dt04576b.

17. Okamoto, J.; Sugo, T.; Katakai, A.; Omichi, H. Amidoxime-Group-Containing Adsorbents for Metal-Ions Synthesized by Radiation-Induced Grafting. J Appl Polym Sci 1985, 30 (7), 2967-2977 DOI: DOI 10.1002/app.1985.070300720.

18. Ladshaw, A. P.; Wiechert, A. I.; Das, S.; Yiacoumi, S.; Tsouris, C. Amidoxime Polymers for Uranium Adsorption: Influence of Comonomers and Temperature. Materials 2017, 10 (11), DOI: Artn 126810.3390/Ma10111268.

19. Kawai, T.; Saito, K.; Sugita, K.; Kawakami, T.; Kanno, J.; Kakakai, A.; Seko, N.; Sugo, T. Preparation of hydrophilic amidoxime fibers by cografting acrylonitrile and methacrylic acid from an optimized monomer composition. Radiat Phys Chem 2000, 59 (4), 405-411 DOI: Doi 10.1016/S0969-806x(00)00298-X.

20. Kawai, T.; Saito, K.; Sugita, K.; Katakai, A.; Seko, N.; Sugo, T.; Kanno, J.; Kawakami, T. Comparison of amidoxime adsorbents prepared by cografting methacrylic acid and 2-hydroxyethyl methacrylate with acrylonitrile onto polyethylene. Industrial & Engineering Chemistry Research 2000, 39 (8), 2910-2915 DOI: Doi 10.1021/Ie990474a.

21. Tian, G. X.; Teat, S. J.; Rao, L. F. Thermodynamic studies of U(VI) complexation with glutardiamidoxime for sequestration of uranium from seawater. Dalton T 2013, 42 (16), 5690-5696 DOI: Doi 10.1039/C3dt32940b.

22. Kang, S. O.; Vukovic, S.; Custelcean, R.; Hay, B. P. Cyclic Imide Dioximes: Formation and Hydrolytic Stability. Industrial & Engineering Chemistry Research 2012, 51 (19), 6619-6624 DOI: 10.1021/ie300492z.

23. Endrizzi, F.; Melchior, A.; Tolazzib, M.; Rao, L. Complexation of uranium(VI) with glutarimidoxioxime: thermodynamic and computational studies. Dalton T 2015, 44 (31), 13835-13844 DOI: 10.1039/c5dt00261c.

24. Priest, C.; Li, B.; Jiang, D. E. Uranyl-Glutardiamidoxime Binding from First-Principles Molecular Dynamics, Classical Molecular Dynamics, and Free-Energy Simulations. Inorg Chem 2017, 56 (16), 9497-9504 DOI: 10.1021/acs.inorgchem.7b00711.

25. Kobuke, Y.; Tanaka, H.; Ogoshi, H. Imidedioxime as a Significant Component in So-Called Amidoxime Resin for Uranyl Adsorption from Seawater. Polym J 1990, 22 (2), 179-182 DOI: DOI 10.1295/polymj.22.179.

26. Parker, B. F.; Zhang, Z.; Rao, L.; Arnold, J. An overview and recent progress in the chemistry of uranium extraction from seawater. Dalton T 2018, 47 (3), 639-644 DOI: 10.1039/c7dt04058j.

27. Priest, C.; Zhou, J. W.; Jiang, D. E. DSolvation of the vanadate ion in seawater conditions from molecular dynamics simulations. Inorg Chim Acta 2017, 458, 39-44 DOI: 10.1016/j.ica.2016.12.027.

CHAPTER TWO

Computational Methods & Formalism

2.1 Introduction

In this chapter, computational methods and theoretical background is provided for uranium related systems. A succinct description of the theoretical background of the quantum mechanics molecular dynamic (QM-MD) tool Vienna ab initio software package (VASP), which solves the Schrodinger equation under the Kahn-Sham DFT (KS-DFT) that utilizes plan-wave all-electron that employs projector-augmented wave (PAW) method to describe the all electron core is presented.[1] Classical molecular dynamic (CMD) force field details for uranium-related systems within the realm of AMBER software package[2], along with procedural setups, is also introduced. Other software discussed include a brief description of the quantum mechanical software used for structure optimization, TURBOMOLE. Moreover, a theoretical description from statistical mechanical point of view on calculating binding free-energies (ΔG_{bind}) from sampling method called umbrella sampling is discussed, as well as its parameter considerations. Continually, some mathematical formulas for applied tools are provided, i.e. radial distribution function (RDF) for fluid systems. Lastly, a list of software and hardware details are included.

2.2 Molecular Dynamics

Molecular dynamics is the practice of computationally modeling atoms or molecules chemically interacting with each other. The chemical behavior of interaction can be

performed both quantum mechanically and classically with molecular dynamic simulations. In both methods, their movements are described by Newton's second law of motion; the rate of change of velocity of an object is proportional to the force acting upon it.[3] Acceleration (a) of each atom in a system can be determined in terms of mass (m) and potential energy (U) relative to position (Equation 2.1).

$$F = ma = -\frac{\partial U}{\partial r}\ , \qquad a = -\frac{1}{m}\frac{\partial U}{\partial r} \qquad \text{Eq. 2.1}$$

We can prescribe the varying positions (r) and velocity (v) of particles at a given time-stamp by the integration of velocity and acceleration that give the following equations:

$$v = \frac{\partial r}{\partial t} \text{ and } a = \frac{\partial v}{\partial t} \qquad \text{Eq. 2.2}$$

$$v = vt + r_o \text{ and } v = at + v_o \qquad \text{Eq. 2.3}$$

$$r = at^2 + v_o t + r_o = -\frac{t^2}{m}\frac{\partial U}{\partial r} + v_o t + r_o \qquad \text{Eq. 2.4}$$

This represents a single MD trajectory can be computed from a particles' initial position, initial velocity, and acceleration that is calculated from the gradient of the potential energy, which describes the force. The state of the system can be evolving in time once the forces have been calculated.

Integration Algorithm

Using a Taylor series expansion:

$$r(t + \delta t) = r(t) + v(t)\,\delta t + \frac{1}{2}a(t)\,\delta t^2 + \ldots \qquad \text{Eq. 2.5}$$

$$v(t + \delta t) = v(t) + a(t)\,\delta t + \frac{1}{2}b(t)\,\delta t^2 + \ldots \quad \text{Eq. 2.6}$$

$$a(t + \delta t) = a(t) + b(t)\delta t + \ldots \quad \text{Eq. 2.7}$$

Verlet Integration

To determine the next trajectory, a value for the electronic structure (next electronic step) needs to be calculated. Once the coefficients from the acceleration are determined, the equation of motion also needs to be determined for a basis set by using the Verlet algorithm. The algorithm is derived from a second-order difference equation for the second derivative (Equations 2.8 and 2.9).[4]

$$r(t + \delta t) = r(t) + v(t)\,\delta t + \frac{1}{2}a(t)\,\delta t^2 \quad \text{Eq. 2.8}$$

$$r(t - \delta t) = r(t) - v(t)\,\delta t + \frac{1}{2}a(t)\,\delta t^2 \quad \text{Eq. 2.9}$$

Summing Equations 2.8 and 2.9 results in the following:

$$r(t + \delta t) = 2r(t) - r(t - \delta t) + a(t)\,\delta t^2 \quad \text{Eq. 2.10}$$

2.2.1 Quantum Molecular Dynamics & Classical Molecular Dynamics

The general difference between QMD and CMD is how the forces are calculated, $F = -\nabla V$ and $F = H(\psi(r))$, respectively. Thus, the evolution of the electronic state can be determined from the perspective of quantum mechanics and classical molecular dynamics. In ab initio MD, instead of using some prescribed potentials, one solves the interatomic forces at a given time by solving the time independent Schrödinger equation. From a quantum-mechanical perspective, the system at a fixed time can be parametrized in terms

of the coordinates of the nuclei and the relevant electrons. By invoking the Born-Oppenheimer approximation, one can regard the nuclei fixed at the instantaneous positions of the atoms. Solving the Schrödinger equation under Hartree-Fock or KS-DFT limit the energy is calculated as a function of the nuclear coordinates that were fixed earlier, and it can thus act as the interatomic potential that is needed to compute the forces in Newton's equation of motion for the nuclei quantum mechanically. Computing the gradients of the DFT energy at this fixed point with respect to the nuclear coordinates, the forces are obtained and the nuclei are moved accordingly to get to the next time step. The DFT process is then repeated with these new nuclear coordinates.

Despite the differences in interatomic representation between QM-MD and CMD methods satisfactory qualitative agreement can provide meaningful conclusions can be drawn regardless of specific model used.

2.2.2 Implicit & Explicit Aqueous Models

In molecular dynamics, one has the feasibility to either fully represent a system with explicit water molecules or as an implicitly by representing the solvent as a continuous medium. Implicit model subjects a solute system to a continuous medium described by a cavity containing a dielectric constant that describes the surrounding solvent. Although a cheaper alternative, an implicit modeling fails to describe contribution imposed by hydrogen bonding in the surrounding medium. To fully represent a real system it is prudent to consider an explicit system because it is able to describe hydrogen-bonding contribution and also polarization effects for interacting systems. However, QM-based calculation

becomes very computational rigorous and costly for larger systems. In this work, we limit ourselves to 100-150 water molecules for QM perspective.

2.2.2 Quantum Mechanics Background

Quantum mechanical formalization for molecular dynamics is provided in this section.

2.2.2.1 Born-Oppenheimer Approximation

One of the main goals is in computational chemistry to solve the time-independent and non-relativist Schrödinger equation. The Schrodinger equation is described as an Eigenvalue problem written in simple terms given in Equation 2.11.

$$\hat{H}\Psi = E\Psi \qquad \text{Eq. 2.11}$$

In Equation 2.11, $\hat{H}$ is the Hamiltonian, Ψ is the wave function, E is the energy. When the Hamiltonian operator acts on a certain wave function (Ψ) and the result yields the same wave function (Ψ, where Ψ is a static state) and the energy (E) is the energy of the state Ψ, the relatively large mass difference between the electron and nuclei make a simplification. The masses of the nuclei can be thought of slow moving particles relative to the electron, meaning we can consider the electrons as moving in the field of fixed nuclei.[5] This gives rise to the Born-Oppenheimer approximation and is described in Equation 2.12.

$$\hat{H}_{total}\Psi_{total}\,(r, R) = E_{total}\Psi_{total}\,(r, R) \qquad \text{Eq. 2.12}$$

The Born-Oppenheimer approximation allows the "separation of variables" of the total wave function nuclear and electronic (due to very large nuclei mass relative to electron), as shown in Equation 2.13.

$$\Psi_{total}\,(r, R) = \Psi_{nuclear}\,(R)\,\Psi_{electronic}\,(r; R) \qquad \text{Eq. 2.13}$$

This suggests the total Hamiltonian can be given the sum of the kinetic energies of the nuclei and the electronic Hamiltonian, given as follows:

$$\hat{H}_{total} = T_{nuc} + H_{elec} \quad \text{Eq. 2.14}$$

where,

$$H_{elec} = T_{elec} + V_{nuc\text{-}elec} + V_{elec\text{-}elec} + V_{nuc\text{-}nuc} \quad \text{Eq. 2.15}$$

and,

$$(T_{nuc} + H_{elec})\Psi_{nuclear}\,\Psi_{electronic} = E_{total}\Psi_{nuclear}\Psi_{electronic} \quad \text{Eq. 2.16}$$

The repulsive $V_{elec\text{-}elec}$ and $V_{nuc\text{-}nuc}$ interaction between like charges are considered. However, the interaction between the electron and nuclei is attractive, since the particles have opposite charges. Equation 2.16 can be simplified to Equation 2.17.

$$(T_{nuc} + H_{elec})\Psi_{nuclear} = E_{total}\Psi_{nuclear} \quad \text{Eq. 2.17}$$

This means that within the approximation we only need the instantaneous positions of the nuclei, not how they are moving, in order to find an electronic wave function. This approximation allows the calculated potential of a mean surface, a 3-dimensional surface on which the N-nuclei move.

2.2.2.2 Approximation Method: Variational Principle

The Schrödinger equation cannot be solved exactly for molecular systems more complicated than a hydrogen atom. To overcome this, variational and perturbation methods are the two most widely used approximation devices, shown in Equation 2.18.

$$E_{\Phi} = \frac{\int \psi^{*}\hat{H}\psi d\tau}{\int \psi^{*}\psi d\tau} = \frac{\langle \psi^{*}|\hat{H}|\psi\rangle}{\langle \psi^{*}|\psi\rangle} \quad \text{Eq. 2.18}$$

E_Φ will be greater than the ground-state energy E_0. In the equation, we have the variational principle (Equation 2.19).

$$E_\Phi \geq E_0 \qquad \text{Eq. 2.19}$$

The variational principle states an upper bound can be calculated to E_0 by utilizing trial functions. The closer Φ is to ψ_0, the closer E_Φ will be to E_0. The full minimization of the functional E_Φ with respect to N-body electrons will yield the true ground-state of ψ_0 and energy, E_0.[6]

2.2.2.3 Electronic Structure

A discussion of methods for solving the electronic structure from QM is discussed in this section with regard to solving the Kahn-Sham DFT (KS-DFT) that utilizes plan-wave all-electron that employs projector-augmented wave (PAW) method.

2.2.2.3.1 Hartree-Fock

A major objective in computational chemistry is to determine the electronic structure in order to map out the potential energy surface of a molecular system. Different approaches have been developed with variable success in correctness and reliability. Many of these approaches utilize the Born-Oppenheimer approximation to reduce the problem of solving the electronic Hamiltonian (Equation 2.14). In theory, if we know the wave function of a system at hand, we can determine its electronic structure and more.

One method is the Hartree-Fock theory, in which the electronic structure approximation is based on the wavefunctions. However, the real wavefunction are troublesome to determine directly. The Hartree-Fock method is based on the mean-field theory that introduces an effective one-particle problem by introducing the description of a mean-field potential generated by all other particles. The mean-field approximation treats

each electron separately and the effect of all other electrons are considered. The Hartree-Fock method is a self-consistent field method that takes on an iterative method that solves the Hamiltonian with an appropriate approximation to obtain a reasonable set of orbitals, and then solving the Schrödinger equation repeatedly until results converge. The wavefunctions are described as a slater determinant made up of one electron orbitals. For instance, we can look at a two-body example (Equation 2.20).

$$\hat{H} = -\frac{1}{2}\sum_{i=1}^{2N}\nabla_i^2 - \sum_{i=1}^{2N}\sum_{1>j}\frac{1}{r_{ij}} + \sum_{A}^{M}\sum_{B<A}^{M}\frac{Z_A Z_B}{R_{AB}} \qquad \text{Eq. 2.20}$$

The first term represents the kinetic energy of the electrons, the second term is the interaction of each electron with each nucleus, the third term is the electron-electron interactions, and the fourth term represents the internuclear interaction. One of the postulates of quantum mechanics is that total wavefunction must be antisymmetric with respect to the interchange of electron coordinates. The Pauli Exclusion Principle states that wavefunctions be antisymmetric with respect to the interchange between two electrons. The antisymmetrized wavefunction or the Hartree-Fock wave function, can be written as a slater determinant.

$$\Psi(1,2\ldots,2N) = \frac{1}{\sqrt{2N!}}\begin{vmatrix} \psi_1\alpha(1) & \psi_1\beta(1) & \cdots & \psi_N\alpha(1) & \psi_1\beta(1) \\ \psi_1\alpha(2) & \psi_1\beta(1) & \cdots & \psi_N\alpha(2) & \psi_1\beta(1) \\ \vdots & \vdots & \ddots & \vdots & \vdots \\ \psi_1\alpha(2N) & \psi_1\beta(2N) & \cdots & \psi_N\alpha(1) & \psi_1\beta(2N) \end{vmatrix} \qquad \text{Eq. 2.21}$$

. The Hartree-Fock is given from the energy of the slater determinant (Equation 2.22),

$$E = 2\sum_{j=1}^{N} I_j + \sum_{i=1}^{N}\sum_{j=1}^{N}(2J_{ij} - K_{ij}) \qquad \text{Eq. 2.22}$$

Where J is the coulomb integrals and K is the exchange integral. The use of slater determinants include fermi correlation arising due to the Pauli Exclusion Principle. In order to find the best wavefunctions approximation methods like the variational principle (Eq. 2.18), as mentioned above, can be applied to determine the spatial orbitals $\psi_i(r_i)$. The ground state wavefunction is one that variationally minimizes the electronic energy.[7]

2.2.2.3.2 Kohn-Sham Density Functional Theory

Density functional theory (DFT) investigates the electronic structure of many-body systems by mapping an all electron as a one electron description. In particular, the Kohn-Sham-DFT (KS-DFT) is, in principle, an exact method, while its predecessors, such as the Hohenberg-Kohn theorem, are inherently an approximation method. In fact, KS-DFT establishes how to compute kinetic energy as a function of density (Equation 2.23),

$$E[\rho(r)] = Ts[\rho] + \int dr v_{ext}(r)\rho(r) + E_H[\rho] + E_{xc}[\rho] \qquad \text{Eq. 2.23}$$

Where the kinetic energy T_s is represented as a function of density, E_H is the Hartree energy, v_{ext} is the external potential acting on the interacting system or electron-nuclei interaction. In this, the kinetic energy is computed in terms of density by assuming that the density corresponds to a wavefunction containing a single slater determinant. Interacting electron density is made up from molecular orbitals of the non-interacting electrons. Non-interacting electrons subject to an external potential such that the ground state density of the non-interacting system is the same as that of an interacting system, v_{ext}. The molecular KS-orbitals are calculated following the variational principle, which seeks to minimize the energy with respect to the density to find the ground state energy. To find the ground state energy, a self-consistent field procedure is used. Unfortunately, the exact exchange-

correlation functional is not known. Many approximate methods for the exchange-correlation energy functional have been devised.[8]

2.2.2.3.2.1 Exchange-correlation Approximation

In principle the exchange-correlation approximations depends on the electron densities, given by the sum of the exchange energy and the correlation energy (Eq. 2.24). It describes an electron moving through a system, moving around itself while interacting electrostatically with an exchange-hole.[9]

$$E_{xc} = E_{exchange} + E_{correlation} \qquad \text{Eq. 2.24}$$

Local Density Approximation (LDA)

One of the oldest and widely used exchange-correlation functional assumes a form that is a linear functional of the density (Equation 2.25),

$$E_{xc}^{LDA}\left[\rho_{\alpha}, \rho_{\beta}\right] = \int \varepsilon_{xc}\left(\rho_{\alpha}, \rho_{\beta}\right)\rho(r)d^{3}r \qquad \text{Eq. 2.25}$$

Where ε_{xc} is the exchange and the correlation energy per electron ($\varepsilon_x + \varepsilon_c$). It is known to yield successful local approximations derived from homogenous electron gas model. A downside of the functional is that it favors homogeneous systems and tends to over-bind molecules and solids.

Gradient Generalized Approximation (GGA)

Gradient Generalized Approximation (GGA) is constructed from first-principles by starting with a second-order density-gradient expansion for the exchange-correlation hole that is surrounded by slowly varying local "spin-up" densities, ρ_{α} and "spin-down" densities, ρ_{β} (Equation 2.26).

$$E_{xc}^{GGA}\left[\rho_{\alpha}, \rho_{\beta}\right] = \int f\left(\rho_{\alpha}, \rho_{\beta}, \nabla\rho_{\alpha}, \nabla\rho_{\beta}\right)d^{3}r \qquad \text{Eq. 2.26}$$

To make practical calculations *f* have to be parameterized analytic functions that describes the functional of a system. The choice of functional greatly depends on the trade-off of accuracy and speed. Typically, GGA favors density inhomogeneity more than LSD. In this project, the PBE functional is utilized because it yields reasonable results in a timely manner and the computational cost is reasonable, especially for fully explicit systems.[10] However, PBE is known to over-bind and over-structure water solvated systems.[11]

Hybrid Functional

The Hybrid functional is a mixture of DFT and Hartree-Fock calculations. This hybrid incorporates the Hartree-Fock equations minimization with respect to the single particle wave functions from constructed slater determinant many-body wave functions, while KS-DFT is derived minimization with respect to density.

$$\mathrm{E_x^{B3LYP}} = 0.8\mathrm{E_x^{LDA}} + 0.2\mathrm{E_x^{HF}} + 0.72\mathrm{E_x^{B88}} + 0.8\mathrm{E_c^{VXN3}} + 0.81\mathrm{E_c^{LYP}}$$

Eq. 2.27

2.2.2.3.2.2 Pseudopotentials

Pseudopotentials are an effective potential constructed to replace the all-electron potentials or the full-potential by eliminating core states, while the valence electrons are described by a pseudo-wavefunction with lesser minimums or nodes. Replacing the complicated effects of motion of the cores electrons and atom and its nucleus with an effective potential called a pseudopotential. The valence electrons are handled explicitly and the core electrons are treated as "frozen," and considered combined with nuclei as a rigid non-polarizable ion core. This reduces complexity of the Schrodinger equation by replacing the Coulombic potential term for the core electrons with the effective potential.

The projector augmented wave methods (PAW) is a generalized method of the pseudopotential the assists in DFT to performed with greater computational efficiency. Compared to other PP methods PAW improves accuracy for magnetic materials alkali and alkali earth elements, 3d elements, lanthanides and actinides.

2.2.2.3.2.3 Plane-wave Basis Sets & Periodic Boundary Conditions (PBC)

Software packages like VASP adopts a planewaves basis set to expand the Kohn-Sham orbitals. In periodic systems, the software uses Bloch's theorem to represent the planewave character of a wave-function. According to Bloch's theorem, a one electron-wavefunction obeys the following:

$$\psi_{nk}(r) = \exp(ik * r)u_{nk}(r) \qquad \text{Eq. 2.28}$$

Where r is a position vector and k is a wave-vector that has certain allowed values defined by the size of the unit cell. If a periodic function $u_{nk}(r)$ is expanded as planewaves that is determined from wave-vectors in reciprocal space, then the variable **G** can be expressed as the sum of the plane waves (Equation 2.29).

$$\sum_{G} c_{i,k+G}\exp(i(k+G)+r) \qquad \text{Eq. 2.29}$$

Plane wave basis is robust for periodic boundary conditions makes utilizing plane wave nature to explicitly solvated systems more efficient.

2.2.3 Classical Molecular Dynamics

CMD methods have the advantage of large scale simulations containing many atoms or large solvated systems. The simulations can be cheaper, also while calculating large scale systems if a GPU is implemented. In the present work, all the CMD calculations are implemented with a GPU.

In classical MD, the force on each atom is calculated as a gradient from a prescribed interatomic potential function called a force field. In principle, the force fields include many terms describing interatomic properties such as bond stretching, angels, dihedral angels, non-bonded terms or Van der Waals (VdW), and electrostatic interactions. There are many CMD software packages that are designed with these interatomic parameters. For example, classical MD package AMBER describes forcefields interatomic parameters as follows:

$$E_{total} = E_{bond} + E_{angle} + E_{dihedral} + E_{electrostatic} + E_{vdw} + E_{improper} \quad \text{Eq. 2.30}$$

The first and second term both bonding and vibrational modes are described quadratically in the following equations:

$$E_{bond} = \sum_{bonds} K_r\left(r - r_{eq}\right)^2 \quad \text{Eq. 2.31}$$

$$E_{angles} = \sum_{angles} K_r\left(\theta - \theta_{eq}\right)^2 \quad \text{Eq. 2.32}$$

In equation 2.31, E_{bonds} represents the energy between covalently bonded atoms relative to an equilibrium distance. This term represents the stretching nature of chemical bonds. We should note that AMBER does not scale the force constant by ½. Classical force fields are described by four interatomic parameters. These parameters are needed to describe the molecular motion of molecules.[2]

The third term represents the dihedral potential, which is defined at the sum of the dihedrals giving the following equation:

$$E_{Dihedrals} = \sum_{Dihedrals} \frac{V_n}{2}[1 + \cos(n\phi - \gamma)] \quad \text{Eq. 2.33}$$

The last two terms are considered the nonbonding terms. The first nonbinding term is the Van der Waals term, or nonbonded, which is described by the Lennard Jones equations (Equation 2.34).

$$\mathrm{E_{vdw}} = \sum_{i<j} \left[\frac{A_{ij}}{R_{ij}^{12}} + \frac{B_{ij}}{R_{ij}^{6}} \right] \qquad \text{Eq. 2.34}$$

The second nonbonding functional represents the electrostatic interaction between atoms of a molecule (Equation 2.35).

$$\mathrm{E_{electrostatic}} = \sum_{i<j} \left[\frac{q_i q_j}{4\pi\varepsilon R_{ij}} \right] \qquad \text{Eq. 2.35}$$

The electrostatic term are the more dominant terms that describes the charges on a nuclei interaction that dictate the atoms charge interaction.

The nature of bonds moving in-and-out of the plane is described by the energy contribution called the improper. As described below in Equation 2.36 as the quadratic term, similarly to that of the bond component of the force field.

$$\mathrm{E_{improper}} = \sum_{\text{improper}} \mathrm{K_{\omega}} \left(\omega - \omega_{\mathrm{eq}} \right)^2 \qquad \text{Eq. 2.36}$$

2.2.3.1 Uranyl Force field

Some challenges in uranyl force field modeling are due to the treatment of electron correlation and relativity, where the use of an adequate solvation model is important especially for highly charged complexes in a polar solvent like water. However, much work has been contributed to the fine tuning of the parametrization of uranyl. In this work, we adopt parameters by Guilbaud et al. that are devised with Free-energy perturbation method based on the difference in hydration free energies between of uranyl.[12] Utilizing high-level

ab initio calculations like DFT or CPMD force field parameters can be fitted to reproduce quantum based calculations with classical molecular dynamics. A mini review on the topic can be found elsewhere.[13]

2.2.3.2 Generalized Amber Force Field (GAFF)

Force fields are the cornerstone of molecular dynamics. When not describing a system by quantum mechanical based calculations, a successful force field is prudent for describing molecular motion of interaction for metal-ligand systems, such as the uranium-ligand systems. Atom types in GAFF are more general and cover most of the organic chemical space. In this work, we first employ GAFF to provide metal-ligand interface description from the perspective of GAFF.

2.2.4 Classical Molecular dynamic Preparation procedure

When desired force fields are achieved one needs to run test simulations to determine if the parameters are reasonable. Steps for setting up a classical MD simulation is described in this section. First, reasonable structures of choice need to be calculated, followed by three minimizations and a heating procedure. Density and production all will be described.

2.2.4.1 Structure Optimizations

Before any classical molecular dynamic simulations, appropriate structures need to be constructed via optimization. Much of this work utilizes software package TURBOMOLE, because of its robust optimization scheme. Uranium is a heavy actinide element and a relatively large basis set is need along with high-level theory. def-TZVP is the basis set of choice for quantum mechanical optimization because it describes 5f/6d

orbitals. Its orbital are represented as a set of split valence, triple zeta valence and quadruple zeta valence quality. Furthermore, small-core (60 electron) atoms were implemented for the optimizations because including all electrons would require longer optimization time. These optimizations still yield reasonable results. Effective core potentials (ECPs) provide a simple and efficient way to account for scalar relativistic effects in electronic structure calculations. Scalar relativistic ECPs are available for all Turbomole functionalities except nuclear magnetic shielding calculations. Turbomole's recommended ECPs for Rb-Rn are the Dirac–Fock ECPs by the Stuttgart–Köln group.[14]

2.2.4.2 Simulation Set-up and Procedure

The minimization procedure contains three steps to ensure a fully relaxed system that is omitted by close contact interactions within the molecule, within the surrounding waters, and a full relaxation for the whole system. First Minimization- 4000 cycles of minimization (2000 cycles of steepest descent and 2000 cycles of conjugate gradient) are carried out to relax the solvent, while solute atoms are constrained by a potential of 3000 kcal/(mol Å). This ensures surrounding waters alleviate close contact with itself. Second Minimization- solute is allowed to slowly interact with surrounding water molecules with a smaller constrained 500 kcal/mol-Å. Third minimization- the solute constraint is turned off and full relaxation of surrounding water molecules with the solute is allowed. After, this three-step minimization is complete a heating protocol is enabled to allow the slow temperature rise of the system from 0 K to a desired temp. In this work, our desired temperature is is 300 K. The heating step is usually short (about 500 ps). Next, a density

process is carried out in an NPT ensemble. This allows for the equilibration of the density and the lattice parameters.

2.2.5 Binding Free-energy Calculations via Umbrella Sampling

Calculating binding free-energy differences are determined for studying the most stable binding motifs, especially for ligand design or mechanistic studies. It is usually taken as the Helmholtz (NVT) or Gibbs free-energy (NPT) ensemble. One of the biggest challenges in free-energy differences is sufficient sampling within phase space. In this work, free-energy is calculated with the bias umbrella sampling method. The harmonic potential allows the exploration in forbidden regions by forcing a system with added potential. Sampling a reaction coordinate is described by a specified collective variable (CV) where the binding energy can be prescribed. The collective variable corresponds to a designated point along the reaction path from a reference molecule using the harmonic biasing potential. After, the binding free-energy can be derived from the potential of the mean force (PMF) of a specified reaction pathway. The PMF can be extracted from the time series data set with an algorithm called weighted histogram analysis method (WHAM). WHAM is a useful method for combining sets of simulations with different biasing potentials in a manner such that the unbiased potential of mean force (PMF) can be found the windows must allow for slight overlap of the ligand positions for proper reconstruction of the PMF curve. The following are the steps taken for the WHAM method:

1. Construct a series of windows describing a reaction coordinate.
2. Run umbrella sampling simulations on each restrained window corresponding to a collective variable.

3. Centralize window simulations.
4. Use the weighted histogram analysis method (WHAM) to extract the PMF and calculate ΔG_{bind}.

2.3 Statistical Mechanics: Application to Free-energy

Essentially, what umbrella sampling allows us to do is extract non-bias probability from a series of performed bias simulations. The unbias probability can allow the further determination of free-energy of a specific reaction pathway. Umbrella sampling is derived from the statistical mechanical Helmholtz canonical ensemble. The Helmholtz statistical ensemble can be equated as followed:

$$F = -\frac{1}{\beta} \ln Q \qquad \text{Eq. 2.37}$$

F = Helmholtz free-energy (kJ/mol or kcal/mol)

Q = Partition function

$\beta = \frac{1}{kT}$

k = Boltzmann constant

T= Temperature (K)

The connection between the molecular view to the macroscopic thermodynamic property is related by the canonical partition function Q.. The energy for the partition function, Q, is defined as:

$$Q = \int \exp[-\beta E(r)] d^N r \qquad \text{Eq. 2.38}$$

Where $\beta = (kT)^{-1}$. A parameter that defines the difference between states can be defined as a variable, ξ. This variable is a continuous function that is described as a collective variable

(CV). This CV is used to thermodynamically connect the initial and final states along a reaction coordinate. A CV can be described by more than one reaction coordinate. In sophisticated practice one can use a linear combination to describe a reaction coordinate, usually called an LCOD. Once an adequate CV along with bias potential, ξ will act to connect between the initial and final states. The unbias partition can be defined as follow:

$$Q_{\text{unbias}}(\xi)=\frac{\int \delta[\xi(r)-\xi]\exp[-\beta E(r)\mathrm{d}^{N}r]}{\int \exp[-\beta E(r)]\mathrm{d}^{N}r} \qquad \text{Eq. 2 39}$$

In general, a bias, additional energy term, is applied to the system to ensure efficient sampling along the reaction coordinate (RC). This is usually achieved with different simulations set to a reason interval or spacing along the RC. A reasonable interval or spacing along the reaction coordinate assures distributions among neighboring windows can achieve overlapping probability distributions. By adding a potential bias, the equation can be realized. Where the bias is the sum of the unbias and the applied potential. The bias energy can be defined as follows:

$$E_{\text{bias}}(r) = E_{\text{unbias}}(r) + \omega(\xi) \qquad \text{Eq. 2.40}$$

Obtaining an unbias free-energy from an applied bias potential can be achieved by relating an unbias distribution and a bias distribution. We can first describe bias and unbias distribution. The overlap between each bias window connects energetically separated regions in phase space. Equation 2.41 defines the unbias distribution. The bias distribution can be defined by adding the applied potential term as defined:

$$P_{\text{unbias}}(\xi) = \frac{\int \exp[-\beta E(r)]\delta[\xi(r)-\xi']\mathrm{d}^{N}r]}{\int \exp[-\beta E(r)]\mathrm{d}^{N}r} \qquad \text{Eq. 2.41}$$

$$P_{\text{bias}}(\xi) = \frac{\int \exp\{-\beta\left[E(r)+wi\left(\xi'(r)\right)\right]\delta[\xi(r)-\xi']\}\mathrm{d}^{N}r}{\int \exp\{-\beta[E(r)+wi(\xi'(r))]\}\mathrm{d}^{N}r} \qquad \text{Eq. 2.42}$$

Probability distribution can be simplified to Equation 2.43.

$$P_{unbias}(\xi) = P_{b,i} \exp[\beta\omega_i(\xi)]\langle\exp[-\beta\omega_i(\xi)]\rangle \quad \text{Eq. 2.43}$$

It should be noted that the third term in Equation 2.43 is the average of the potential. The $P_{i,b}$ is determined from a MD simulation. This allows the readily determination of Helmholtz free-energy. The estimate of unbias free-energy is given by the following:

$$A_i(\xi) = -\frac{1}{\beta}\ln P_{i,b}(\xi) - w_i(\xi) + F_i \quad \text{Eq. 2.44}$$

When the free-energy require the combination of more than one window to determine $A(\xi)$, Fi needs to be determined. Fi is associated by introducing a bias potential and connecting a trail of different windows along a reaction coordinate. This derivation is adopted from an advanced review.[15]

2.3 Harmonic Potential

One of the most important ingredients to a successful PMF is a good potential restraint. Once the reaction space has been divided into many windows, a potential must be applied to each window. The applied potential or force constant required for US is a harmonic restraint defined as the following:

$$\omega(\xi) = \frac{k}{2}(\xi - \xi_{ref})^2 \quad \text{Eq. 2.45}$$

Each independent window allows to only sample within a specified region. The dependency of the harmonic potential allows the probability distribution of that specified window. The harmonic restraint allows neighboring windows distribution tails to overlap. It is very important to check the all neighboring overlaps to ensure reliable results. In general, one needs a large enough force constant to drive the system over barriers.

However, there are some caveats when choosing a force constant, increasing the force constant to “high,” will develop narrow windows that will create poor overlap and too small will create too much overlap that will cost information. Every system is different and many barriers can be experienced. A nice attribute of umbrella sampling is that the force constant can be varied along a reaction coordinate. Varying the harmonic restraint allows control overlap of neighboring windows, especially in highly energetic regions at the barriers. From experience a uniform height and width of the overlapping distributions along the entire reaction coordinate ensures reliable information.

2.3 Weighted Histogram Analysis Method for PMF Construction

Each window has different free-energies and are off-set. To stitch these different windows with their relative free-energies a method needs to be applied. After all windows have been simulated and windows probability distribution is acquired according to the aforementioned criteria, a PMF curve can be constructed with different methods, but the most applied is the weighted histogram method or WHAM, which is an analytical method for stitching.

2.3 Calculating Binding Energy from PMF Curve

Applying the above-mentioned recipe for calculating a PMF, W(r), can be related to the radial distribution function (RDF). Methods for calculating binding energy can be found in reference.[16] The post-processing workflow is described below.

When the PMF has been determined with umbrella sampling coupled with WHAM[17], the radial distribution function can be determined,

$$W(r) = -RT\ln[g(r)] \qquad \text{Eq. 2.46}$$

Where R is the ideal gas constant (8.314 J/mol-K), T is temperature (K), and g(r) is the radial distribution function (RDF). After the RDF is determined, the corresponding equilibrium constant for the relative reaction pathway can be calculated by integrating the RDF constructed from the PMF. Since K_a of association (binding) is independent of composition and to avoid activity coefficients, the molecular-based calculation can be analyzed in an approximated infinite dilute solution to where salt concentration,ρ, goes to zero and results in the integrand:

$$K_a = 4\pi \int g(r) r^2 dr \qquad \text{Eq. 2.47}$$

The calculated equilibrium constant can then be applied to determine the binding free-energy of a specified reaction pathway.

$$\Delta G_{bind} = -RT\ln K_a \qquad \text{Eq. 2.48}$$

A bias sampling method, like umbrella sampling, that uses a harmonic bias can be used to construct a PMF curve from a series of simulated windows. In short, the binding free-energy can easily be determined from a constructed PMF curve that is devised from umbrella sampling, coupled with WHAM.

2.2.6 Radial Distribution Function (RDF)

In some cases when performing molecular dynamics, one needs to garner information about the molecular structure of the coordination sphere of metal-ligand interactions and its surrounding aqueous environment. In solid state, the molecular crystal structure is important for determining the molecular coordinating environment, while in solution phase coordination and hydration can be pried into with an algorithmic function

called the radial distribution function (RDF). RDF is determined by binning the distance between particle pairs into a histogram. For 3D, the normalization is defined as the number density of the system multiplied by the spherical shell, $\rho\pi r^2 dr$. For a fluid, the RDF can be derived from the description below, which is adopted from McQuarries Statistical Mechanics textbook.[6]

Considering all possible combinations particles positions, a canonical ensemble (N, V, T) with a configurational integral is defined as, $Z_N = \int \dots \int e^{-\beta U_N} \, dr_1 \dots dr_N$. The probability that molecule 1 is dr_1 at r_1, molecule 2 in dr_2 at r_2 is given by,

$$P^{(N)}(r_1,\dots,r_N)\, dr_1 \dots dr_N = \frac{e^{-\beta U_N}\, dr_1 \dots dr_N}{Z_N} \qquad \text{Eq. 2.49}$$

Treating positions only n < N particles fixed for $r_1 \dots r_n$ having no constraints on the remaining N – n molecules, which is obtained by integrating Equation 2.50.

$$P^{(n)}(r_1, \dots, r_n) = \frac{\int \dots \int e^{-\beta U_N}\, dr_{n+1} \dots dr_N}{Z_N} \qquad \text{Eq. 2.50}$$

Assuming identical particles, the probability that any molecule is in dr_1 at r_1 or any molecule is in dr_n at r_n is

$$\rho^{(n)}(r1, \dots, rn) = \frac{N!}{(N-n)!} \text{ x } P^{(n)}(r_1, \dots, r_n) \qquad \text{Eq. 2.51}$$

A one particle density for a crystal with a periodic function exhibits a sharp maximum at lattice sites, when n = 1. For homogeneous liquids, all points in the volume (V) are equivalent and thus $\rho^{(n)}$ is independent of r_1. For fluids, we can then write the following,

$$\frac{1}{V} \int \rho^{(1)}(r_1) dr_1 = \rho^{(1)} = \frac{N}{V} = \rho \qquad \text{Eq. 2.52}$$

Where Eq. 2.49 and Eq. 2.51 are used to equate the integral of $\rho^{(1)}$ to N. The *correlation function* $g(r)^{(n)}$ is defined as,

$$\rho^{(n)}(r_1, \ldots, r_n) = \rho^n g^{(n)}(r_1, \ldots, r_n) \qquad \text{Eq. 2.53}$$

Where $g^{(n)}$ is called the correlation function because if we treat the molecules as independent of each other, $\rho^{(n)}$ would equal ρ^n, and so the factor $g^{(n)}$ corrects for the "dependence" or the correlation between the molecules. We can rearrange the correlation function as follows:

$$g^{(n)}(r_1, \ldots, r_n) = \frac{V^n N!}{N^n (N-n)!} \text{ x } \frac{\int \ldots \int e^{-\beta U_N} dr_{n+1} \ldots dr_N}{Z_N} \qquad \text{Eq. 2.54}$$

$$g^{(n)}(r_1, \ldots, r_n) = V^n(1 + O(N^{-1})) \text{ x } \frac{\int \ldots \int e^{-\beta U_N} dr_{n+1} \ldots dr_N}{Z_N} \qquad \text{Eq. 2.55}$$

$$\int_0^\infty \rho g(r) 4\pi r^2 \, dr = N - 1 \sim N \qquad \text{Eq. 2.56}$$

2.2.7 Hydrogen Bond Analysis (Time Autocorrelation)

Hydrogen bonding kinetics can be analyzed by hydrogen bonding lifetimes. A lifetime is defined as the length of time something remain present. The time correlation function is defined as follows,

$$\tau = \int_0^\infty C(\tau) d\tau \qquad \text{Eq. 2.57}$$

$$C_{HB}(t) = \left\langle \frac{p(t)_{ij} p(0)_{ij}}{p(0)_{ij}^{\,2}} \right\rangle \qquad \text{Eq. 2.58}$$

where $p_{ij}(t)$ equals 0 or 1 depending on the hydrogen bond state of a given atoms pair i and j. If atoms i and j are hydrogen bonded at times 0 and t for periods longer than t $p_{ij}(t) = 1$. Otherwise, $p_{ij}(t) = 0$.[18]

2.3 Basin-hopping

Basin-hopping is a global optimization technique in which the potential energy surface is transformed into a collection of interpenetrating staircases. It is a Monte-Carlo-

minimization technique to explore a global minimum structure for a nanocluster system comprising of few to few hundred uniform cluster systems. A diagram for its computational algorithm is shown in Figure 2.1.[19]

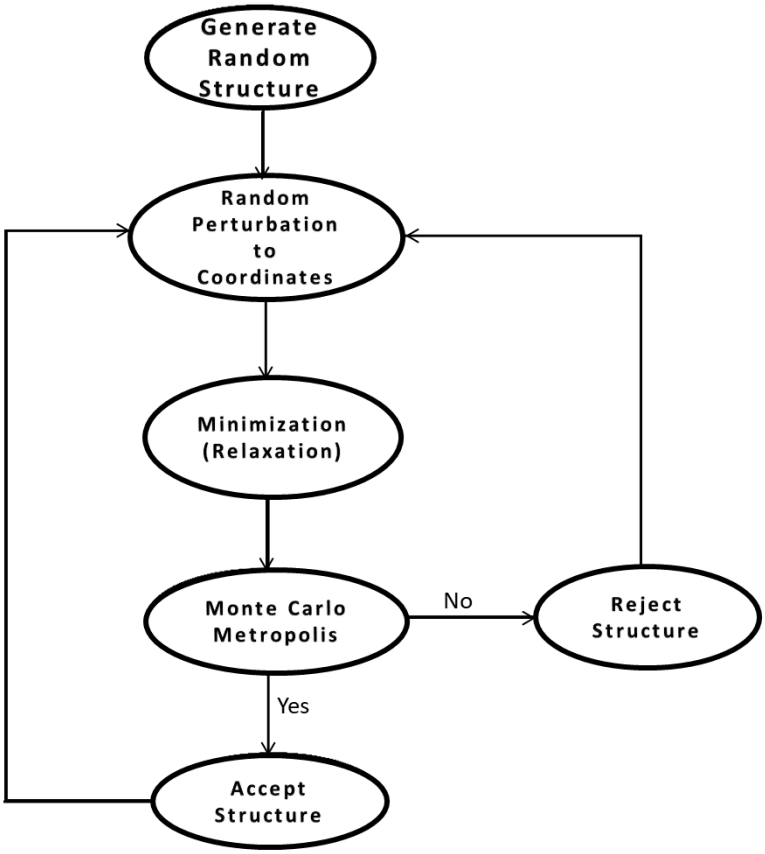

Figure 2.1 Is flow diagram for computational algorithm for basin-hopping.

2.4 Software and Hardware

The following is a list of software and hardware utilized throughout this work.

Quantum mechanical packages

1. Vienna Ab initio simulation package (VASP) 5.3.1

2. TURBOMOLE

3. Gaussian09 patch C.1

Classical molecular dynamic simulation packages

1. AMBER 14

2. AMBER16

Visualization & analysis programs

1. VMD (Visual molecular dynamics) – visualization program for displaying and analyzing molecular dynamic and optimization

2. Molden – visualization program for displaying structures

3. Jmol - visualization program for displaying structures

4. cpptraj – interactive AMBER tool for processing trajectory files for post-processing

CPU hardware

Linux cluster built by Aspen systems that has a node of 16 AMD Opteron cores and 64 GB Memory. It has 16 compute nodes each containing 64 AMD Opteron cores and 128 GB memory. Total it has 1040 cores and 2176 GB memory.

GPU hardware

Two different GPU servers.

First: is a linux GPU server built by Exxact, that contains two intel Xeon E5-2620 6-core CPUs with eight Nvidia GTX 980 GPU cards.

Second: is a linux GPU server built by Exaact, containing two intel Xeon E5-2620 6-core CPUs with eight Nvidia GTX 1080 GPU cards.

2.5 References

1. Hafner, J. Ab-initio simulations of materials using VASP: Density-functional theory and beyond. J. Comput. Chem., 2008, 29 (13), 2044-2078 DOI: 10.1002/jcc.21057.

2. D.A. Case, V. B., J.T. Berryman, R.M. Betz, Q. Cai, D.S. Cerutti, T.E. Cheatham, III, T.A. Darden, R.E.; Duke, H. G., A.W. Goetz, S. Gusarov, N. Homeyer, P. Janowski, J. Kaus, I. Kolossváry, A. Kovalenko,; T.S. Lee, S. L., T. Luchko, R. Luo, B. Madej, K.M. Merz, F. Paesani, D.R. Roe, A. Roitberg, C. Sagui,; R. Salomon-Ferrer, G. S., C.L. Simmerling, W. Smith, J. Swails, R.C. Walker, J. Wang, R.M. Wolf, X.; Kollman, W. a. P. A. AMBER 14, University of California, San Francisco, 2014.

3. Leggett, C. J.; Parker, B. F.; Teat, S. J.; Zhang, Z.; Dau, P. D.; Lukens, W. W.; Peterson, S. M.; Cardenas, A. J. P.; Warner, M. G.; Gibson, J. K.; Arnold, J.; Rao, L. Structural and spectroscopic studies of a rare non-oxido V(v) complex crystallized from aqueous solution. Chem. Sci. 2016, 7 (4), 2775-2786 DOI: 10.1039/c5sc03958d.

4. Hairer, E.; Lubich, C.; Wanner, G. Geometric numerical integration : structure-preserving algorithms for ordinary differential equations. Springer: Berlin ; New York, 2002; p xiii, 515 pages.

5. Born, M.; Oppenheimer, R. Quantum theory of molecules. Ann Phys-Berlin 1927, 84 (20), 0457-0484.

6. McQuarrie, D. A. Statistical Mechanics. University Science Books: 2000.

7. McQuarrie, D. A. Quantum Chemistry. University Science Books: 2008.

8. Kohn, W.; Sham, L. J. Self-Consistent Equations Including Exchange and Correlation Effects. Phys. Re.,v 1965, 140 (4A), 1133-& DOI: DOI 10.1103/PhysRev.140.A1133.

9. Ziesche, P.; Kurth, S.; Perdew, J. P. Density functionals from LDA to GGA. Comp Mater. Sci., 1998, 11 (2), 122-127 DOI: Doi 10.1016/S0927-0256(97)00206-1.

10. Perdew, J. P.; Burke, K.; Ernzerhof, M. Generalized gradient approximation made simple. Phys. rev. letts. 1996, 77 (18), 3865.

11. Lin, I. C.; Seitsonen, A. P.; Tavernelli, I.; Rothlisberger, U. Structure and Dynamics of Liquid Water from ab Initio Molecular Dynamics-Comparison of BLYP, PBE, and revPBE Density Functionals with and without van der Waals Corrections. J. Chem. Theo. Comput., 2012, 8 (10), 3902-3910 DOI: 10.1021/ct3001848.

12. Guilbaud, P.; Wipff, G. MD simulations on UO2 (2+) and Sr2+ complexes with CMPO derivatives in aqueous solution and at a water/chloroform interface. N. J. Chem. 1996, 20 (6), 631-642.

13. Buhl, M.; Wipff, G. Insights into Uranyl Chemistry from Molecular Dynamics Simulations. Chemphyschem. 2011, 12 (17), 3095-3105 DOI: 10.1002/cphc.201100458.

14. Furche, F.; Ahlrichs, R.; Hattig, C.; Klopper, W.; Sierka, M.; Weigend, F. Turbomole. Wires. Comput. Mol. Sci., 2014, 4 (2), 91-100 DOI: 10.1002/wcms.1162.

15. Kastner, J. Umbrella sampling. Wires. Comput. Mol. Sci. 2011, 1 (6), 932-942 DOI: 10.1002/wcms.66.

16. Chialvo, A. A.; Cummings, P. T.; Cochran, H. D.; Simonson, J. M.; Mesmer, R. E. Na+-Cl- Ion-Pair Association in Supercritical Water. J. Chem. Phys. 1995, 103 (21), 9379-9387 DOI: Doi 10.1063/1.470707.

17. Kumar, S.; Bouzida, D.; Swendsen, R. H.; Kollman, P. A.; Rosenberg, J. M. The Weighted Histogram Analysis Method for Free-Energy Calculations on Biomolecules .1. The Method. J. Comput. Chem., 1992, 13 (8), 1011-1021 DOI: DOI 10.1002/jcc.540130812.

18. Chen, C.; Li, W. Z.; Song, Y. C.; Weng, L. D.; Zhang, N. Hydrogen Bonding Analysis of Hydroxyl Groups in Glucose Aqueous Solutions by a Molecular Dynamics Simulation Study. B. Korean. Chem. Soc., 2012, 33 (7), 2238-2246 DOI: 10.5012/bkcs.2012.33.7.2238.

19. Wales, D. J.; Doye, J. P. K. Global optimization by basin-hopping and the lowest energy structures of Lennard-Jones clusters containing up to 110 atoms. J. Phys. Chem. A 1997, 101 (28), 5111-5116 DOI: Doi 10.1021/Jp970984n.

CHAPTER THREE

First-principles molecular dynamics simulation of the $Ca_2[UO_2(CO_3)_3]$ complex in water.

3.1 Abstract

Recent experiments have shown that the neutral $Ca_2UO_2(CO_3)_3$ complex is the dominant species of uranium in many uranyl-containing streams. However, the structure and solvation of such a species in water has not been investigated from first principles. Herein we present a first principles molecular dynamics perspective of the $Ca_2UO_2(CO_3)_3$ complex in water based on density functional theory and Born–Oppenheimer approximation. We find that the $Ca_2UO_2(CO_3)_3$ complex is very stable in our simulation timeframe for three different concentrations considered and that the key distances from our simulation are in good agreement with the experimental data from extended X-ray absorption fine structure (EXAFS) spectroscopy. More important, we find that the two Ca ions bind differently in the complex, as a result of the hydrogen-bonding network around the whole complex. This finding invites confirmation from time-resolved EXAFS and has implications in understanding the dissociative equilibrium of the $Ca_2UO_2(CO_3)_3$ complex in water.

3.2 Introduction

The concentration of uranium in seawater is very minute at about 3.3 ppb, but the large mass of seawater contains about 4.5 billion metric tons of uranium.1 Mining uranium

from seawater can provide an ideal sustainable alternative to current uranium mining methods (open pit, underground, and leaching) that create much environmental concern. In addition, extraction from seawater can provide a price ceiling for uranium that is of strategic importance in evaluating the economics of long-term supply of uranium for nuclear energy.[2,3] Much research has been focused on the development of selective methods for mining uranium in seawater. Currently, the most viable method is utilizing an amidoxime-functionalized polymer sorbent known as poly(acrylamidoxime) fibers.[1–6] However, to make the uranium extraction from seawater economically viable, sorbent performance in terms of uranium uptake and uranium/vanadium selectivity needs to be further improved.[1,7] To design a better ligand and sorbent for uranium extraction, it is necessary to understand the fundamentals about uranium speciation in seawater.

In aqueous solution, uranium exists as the stable oxocation with an oxidation state of U(VI), called uranyl – $UO2^{2+}$. Early work has focused on prying into the prominent equilibrium species bound to the uranyl complex in seawater8 and suggested the anionic $[UO_2(CO_3)_3]^{4-}$ complex to be the dominant species in seawater. However, over the past two decades experimental data has shifted the consensus to cationbalanced complexes.[9–13] Concentrations of magnesium (Mg^{2+}) and calcium (Ca^{2+}) in seawater are overwhelmingly larger than the concentration of U(VI), so the ternary $Ca–UO_2–CO_3$ or $Mg– UO_2–CO_3$ exists predominately in seawater. The complexation of Ca^{2+} with $[UO_2(CO_3)_3]^{4-}$ has been validated experimentally by Bernhard et al.[10] and Kelly et al.[11] with extended X-ray absorption fine structure (EXAFS) spectroscopy. Most recently, Rao et al.[13] examined the thermodynamics of uranium in seawater and the complexation between Ca/Mg and

$[UO_2(CO_3)_3]^{4-}$. They concluded that in seawater pH (8.2) $Ca_2UO_2(CO_3)_3$ accounts for 58% of the total uranium in the solution while $CaUO_2(CO_3)_3^{2-}$ and $MgUO_2(CO_3)_3^{2-}$ account for 18% each and $[UO_2(CO_3)_3]^{4-}$ accounts for only 6%.[13] In addition, Rao et al. studied the binding of U(VI) with various types of ligands and the subsequent leaching process.[14–19] In addition, the stability constant for the speciation of calcium is larger than magnesium.[13]

On the theoretical and computational side, work has been done on the binding of $UO2^{2+}$ with ligands using a cluster model[18,20–23] and on the structure and dynamics of $[UO_2(CO_3)_3]^{4-}$ in aqueous environment using molecular dynamics (MD) simulations.[24–27] Hofer et al. examined the structure and dynamics of $[UO_2(CO_3)_3]$ 4− in water using quantum mechanical charge field molecular dynamics (QMCF-MD).[24,25] Kerisit et al. investigated the structure and dynamics of $Ca_2UO_2(CO_3)_3$ in aqueous solution with classical MD simulations based on non-polarizable force fields.26 Given the highly charged nature of Ca^{2+} ions and $[UO_2(CO_3)_3]^{4-}$, polarization may be important in describing the interaction between Ca^{2+} ions and $[UO_2(CO_3)_3]^{4-}$ and between the complex and the water molecules. First principles MD at the electronic structure would be desirable, as the polarization effect is taken into account automatically. However, no such work has been done on $Ca_2UO_2(CO_3)_3$ in aqueous solution, to the best of our knowledge. The present work seeks to describe the structure and solvation of $Ca_2UO_2(CO_3)_3$ in water using first principles MD based on density functional theory (DFT-MD for short) for the first time. Our goal is to provide a fundamental baseline understanding of the structure and solvation of $Ca_2UO_2(CO_3)_3$ in water in terms of Ca–$UO_2(CO_3)_3$ and Ca–water interactions. The other

goal is to compare DFT-MD simulations with the previous EXAFS data and classical MD simulations.

3.3 Computational methods

First-principles molecular dynamics simulations based on density functional theory (DFT-MD) and Born–Oppenheimer approximation were carried out using the Vienna ab initio simulation package with plane wave basis and periodic boundary conditions.[28,29] The Kohn–Sham equations are solved with the all-electron projected augmented wave (PAW) method.[30,31] We have chosen the Perdew–Burke–Ernzerhof (PBE) functional of the generalized-gradient approximation (GGA) for electron exchange and correlation.[32] PBE is one of the most popular GGA functionals, providing a balanced description for diverse molecules and materials, instead of being designed for a special class of molecules or interactions. In the case of liquid water, it has been shown that the PBE functional can describe well the peak positions in the radial distribution functions of g_{OO} and g_{OH} for the liquid structure of water but it overestimates the peak heights, in comparison with the experiment, leading to over-structuring.[33,34] Using hybrid functionals together with van der Waals interactions can soften the water structure, giving a better agreement with the experiment. But hybrid functionals are usually about two orders of magnitude more expensive than a pure DFT method such as GGA-PBE. We think that PBE is a reasonable choice in balancing accuracy and efficiency. In the ESI,† we provide an orbital-resolved local density of states for the U atom (Fig. S1†) from a snapshot of the $Ca_2UO_2(CO_3)_3$ complex in water to show that the bonding picture from the PBE functional is consistent with previous theoretical studies.[35,36]

The MD calculations were carried out at 298 K in a canonical NVT ensemble for a periodic cubic box that contains one $Ca_2UO_2(CO_3)_3$ complex in a fixed number of water molecules. Three concentrations were examined: 0.53 M, 0.42 M, and 0.36 M, corresponding to one $Ca_2UO_2(CO_3)_3$ complex in a periodic box containing 100, 125, and 150 water molecules, respectively; the corresponding simulation box sizes and densities are also compared in Table 1. Here we note that since there is only one complex in the simulation box for the three concentrations, this approach cannot probe the correlations between complexes but serves more to test the potential presence of size artifacts. We determined the densities from constant-pressure classical MD simulations using force-field parameters from a previous study.[26] The temperature was kept constant via a Nose–Hoover thermostat. A Verlet algorithm was used to integrate Newton's equation of motion with a time step of 1 femtosecond. After equilibration at 298 K for 15 ps, another 15 ps of production run was followed. Graphical visualization and analysis of the liquid structure packing of the uranium complex was examined with VMD.[3]

Table 3.1 Three concentrations of $Ca_2UO_2(CO_3)_3$, the corresponding water molecules in the simulation boxes, the box sizes, and the densities, examined in the present work.

Concentration (M)	Water molecules	Simulation box size (Å)	Density (g cm^{-3})
0.36	150	17.5	1.13
0.42	125	16.7	1.14
0.53	100	15.7	1.21

3.4 Results & Discussion

3.4.1 Interaction between calcium and carbonate

The most important structural feature of the $Ca_2UO_2(CO_3)_3$ species is the binding between the two Ca ions and the $[UO_2(CO_3)_3]^{4-}$ ion. This interaction is mediated by the carbonate groups. As shown in Fig. 3.1, the three carbonate groups bind to the uranyl group on the equatorial plane in a bidentate mode; this structural model has been established from the crystal structure of the naturally occurring mineral Liebigite $[Ca_2UO_2)(CO_3)_3{\cdot}11H_2O]$,[38] fitting of the EXAFS data,[10,11] and quantum mechanical modeling.[20] There are three different oxygens in the uranium complex: the two axial oxygens (O_{ax}) triple-bonded to U in the uranyl structure,[35] six equatorial carbonate oxygens (O_{eq}) that are bonded to U, and three distal carbonate oxygens (O_{dis}) not directly interacting with U. The two Ca^{2+} ions bind to the carbonate groups on the same plane; each Ca^{2+} ion binds to two equatorial oxygen atoms from two neighboring carbonate groups. In our DFT-MD simulations, interaction of the Ca ions to the $[UO_2(CO_3)_3]^{4-}$ complex was monitored by the four Ca–O_{eq} distances (dashed lines in Fig. 3.1): Ca1–O1, Ca1–O2, Ca2–O3, and Ca2–O4.

We placed an initial structure of the uranium complex as shown in Fig. 3.1 into a periodic water box at a concentration of 0.53 M. After equilibration at 298 K, a production run of 15 ps was used for statistical analysis. Fig. 3.2 shows the four Ca–O_{eq} distances during the 15 ps production trajectory. One can see that Ca1–O1 and Ca1–O2 distances exhibit fluctuations around 2.45–2.50 Å (Fig. 3.2a), while Ca2–O3 and Ca2–O4 around 2.35–2.40 Å (Fig. 3.2b). So in our simulation timeframe, the $Ca_2UO_2(CO_3)_3$ complex is

very stable and maintains steady Ca–O_{eq} addition, there is a slight difference between the two O_{eq} atoms binding to each Ca^{2+}. For Ca1, Ca1–O1 is slightly shorter than Ca1–O2; for distances about 2.45 Å with a standard deviation of about 0.12 Å. Another important observation is that there exists asymmetry between the two Ca ions: Ca2 binds to $[UO_2(CO_3)_3]^{4-}$ stronger than Ca1, as evidenced by the shorter average Ca2–O_{eq} distance (2.37 Å; Fig. 3.2b) than Ca1–O_{eq} (2.47 Å; Fig. 3.2a). Here we note that initially, we placed the $Ca_2UO_2(CO_3)_3$ complex randomly inside a water box. To test the robustness of the asymmetric structure, we tried several different initial configurations of water solvation around the $Ca_2UO_2(CO_3)_3$ complex and found that they always equilibrated to the asymmetric configuration after about 5 ps.

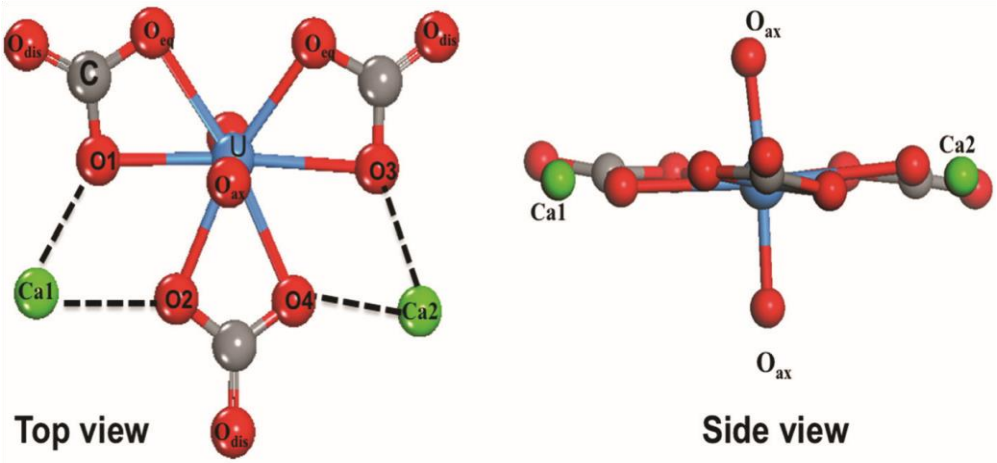

Figure 3.1 Top view and side view of the $Ca_2UO_2(CO_3)_3$ complex in water.

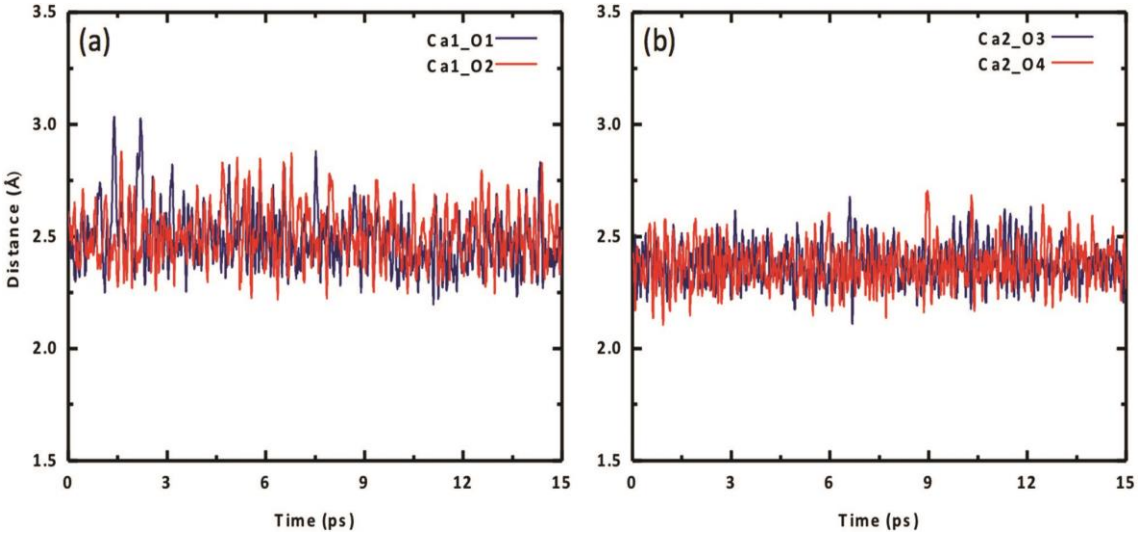

Figure 3.2 Change of Ca–O distances with time for the $Ca_2UO_2(CO_3)_3$ complex in water (0.53 M): (a) Ca1–O1 and Ca1–O2; (b) Ca2–O3 and Ca2–O4. See Fig. 3.1 for atom labels.

To further examine the difference between the two Ca ions, we plot the radial distribution function (RDF) of carbonate O_{eq} atoms around each of the two Ca ions in Fig. 3.3. One can see that the stronger binding Ca^{2+} has a narrower and higher O_{eq} distribution (Fig. 3b), while the weaker Ca^{2+} has a broader and lower O_{eq} distribution (Fig. 3.3a). In addition, there is a slight difference between the two O_{eq} atoms binding to each Ca^{2+}. For Ca1, Ca1–O1 is slightly shorter than Ca1–O2; for Ca2, Ca2–O4 is slightly shorter than Ca2–O3.

To confirm the stability of the $Ca_2UO_2(CO_3)_3$ complex and the asymmetry of the two Ca^{2+} ions, we further simulated two lower concentrations (0.42 M and 0.36 M) and arrived at the same conclusions. The $Ca_2UO_2(CO_3)_3$ complex in the two lower concentrations is also stable in our simulation time frame, as shown by the steady maintaining of the binding of the two Ca^{2+} ions with the $[UO_2(CO_3)_3]^{4-}$ complex. More interestingly, we found that the asymmetry between the two Ca^{2+} ions also persists in the two lower concentrations, indicating that this is likely an intrinsic feature of the $Ca_2UO_2(CO_3)_3$ complex in water. Fig. 3.4 displays the four Ca–O_{eq} distances as a function of the U concentration. Both the asymmetry between the two Ca^{2+} ions and the small difference between the two O_{eq} atoms for each Ca^{2+} ion is evident.

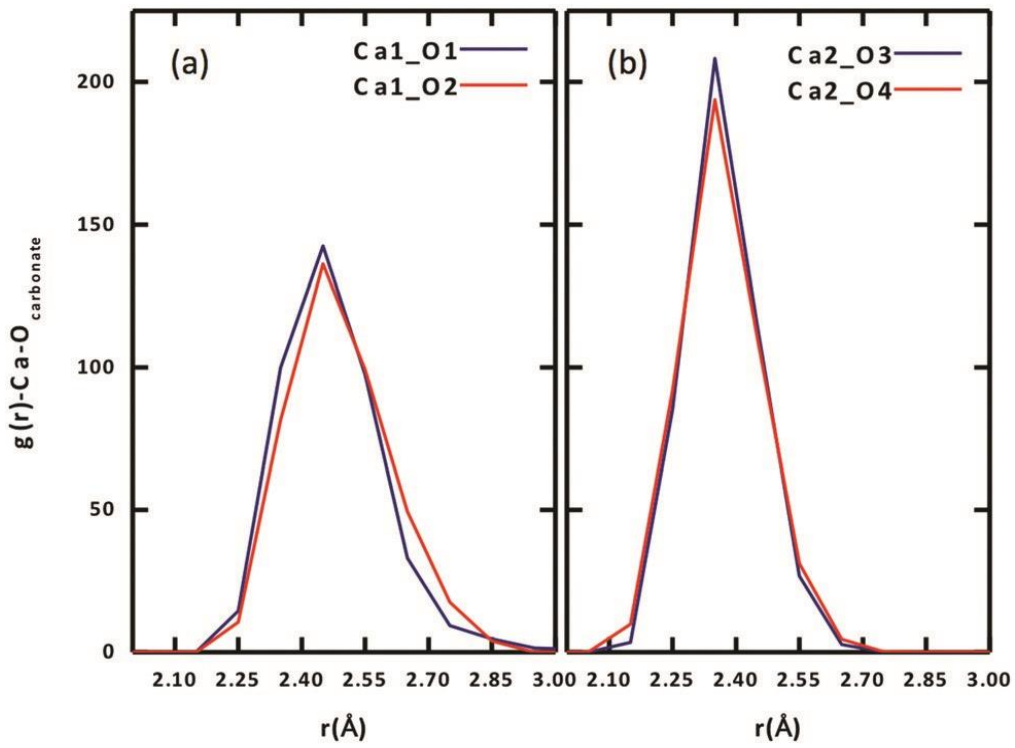

Figure 3.3 Radial distribution functions of equatorial carbonate oxygen (Oeq) around each Ca ion of the $Ca_2UO_2(CO_3)_3$ complex in water (0.53 M): (a) Ca1; (b) Ca2. See Fig. 1 for atom labels.

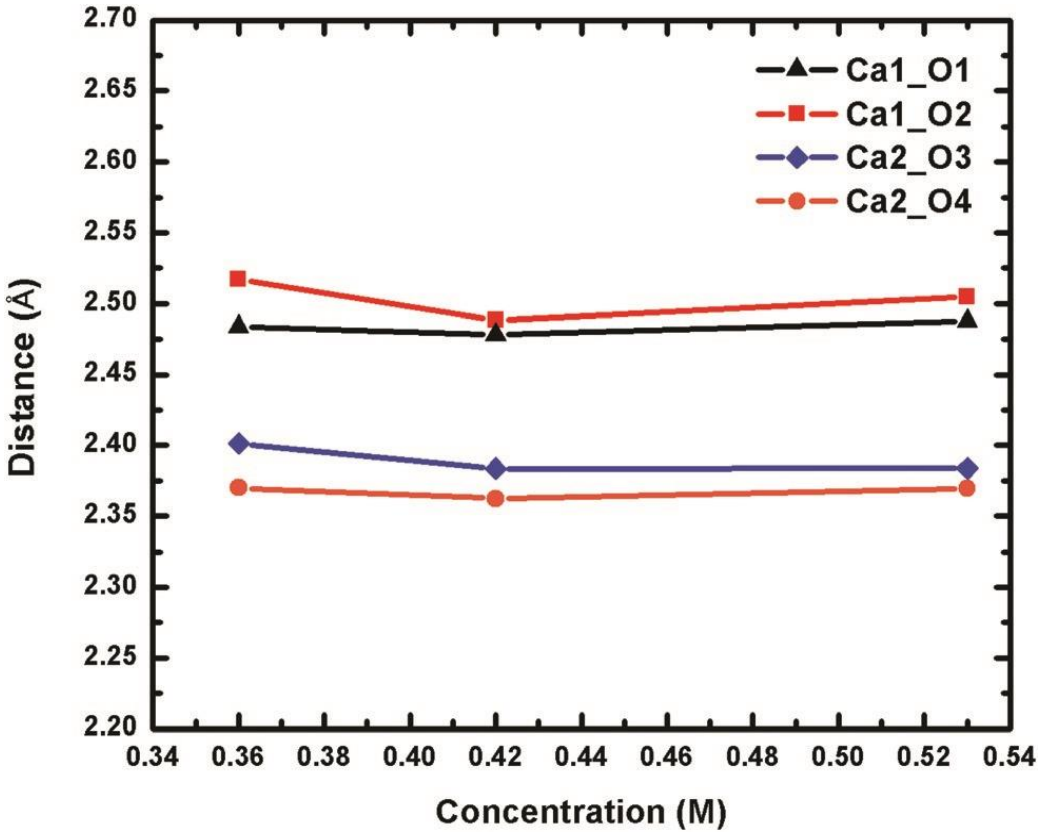

Figure 3.4 Change of the four Ca–Oeq distances of the $Ca_2UO_2(CO_3)_3$ complex in water at three different concentrations. See Fig. 3.1 for atom labels. The distances are averages over 15 ps trajectories.

3.4.2 Interaction between calcium and water

The interaction between calcium and carbonate in the $Ca_2UO_2(CO_3)_3$ complex is the most important information that we obtained from our DFT-MD simulations. The asymmetry between the two Ca^{2+} ions must be closely related to the water molecules around the $Ca_2UO_2(CO_3)_3$ complex. We now analyze the interaction between the two Ca^{2+} ions and the water molecules. Fig. 3.5 shows radial distribution functions (RDFs) of oxygen atoms from the water molecules around the two Ca^{2+} ions both separately and together. One can see that the solvation shell around Ca1 has an average $Ca–O_{water}$ distance of 2.45 Å (with a standard deviation of 0.12 Å) and the integrated RDF (with a cutoff at 3.0 Å) gives the coordination number of five; in other words, there are five molecules around Ca1 in addition to the two O_{eq} atoms from two carbonate groups. On the other hand, Ca2 has four water molecules in the solvation shell with an average $Ca–O_{water}$ distance of 2.35 Å (with a standard deviation of 0.09 Å). So together, the average coordination number of the two Ca^{2+} ions is 4.5 in terms of water molecules. We further examined the RDF of water oxygens around Ca^{2+} ions for the two lower concentrations and found the same trend of five water molecules around Ca1 and four water molecules around Ca2. In comparison, previous classical MD simulations predicted that both calcium ions have five water molecules in the first hydration shell,[26] similar to the case of Ca1 in our simulation.

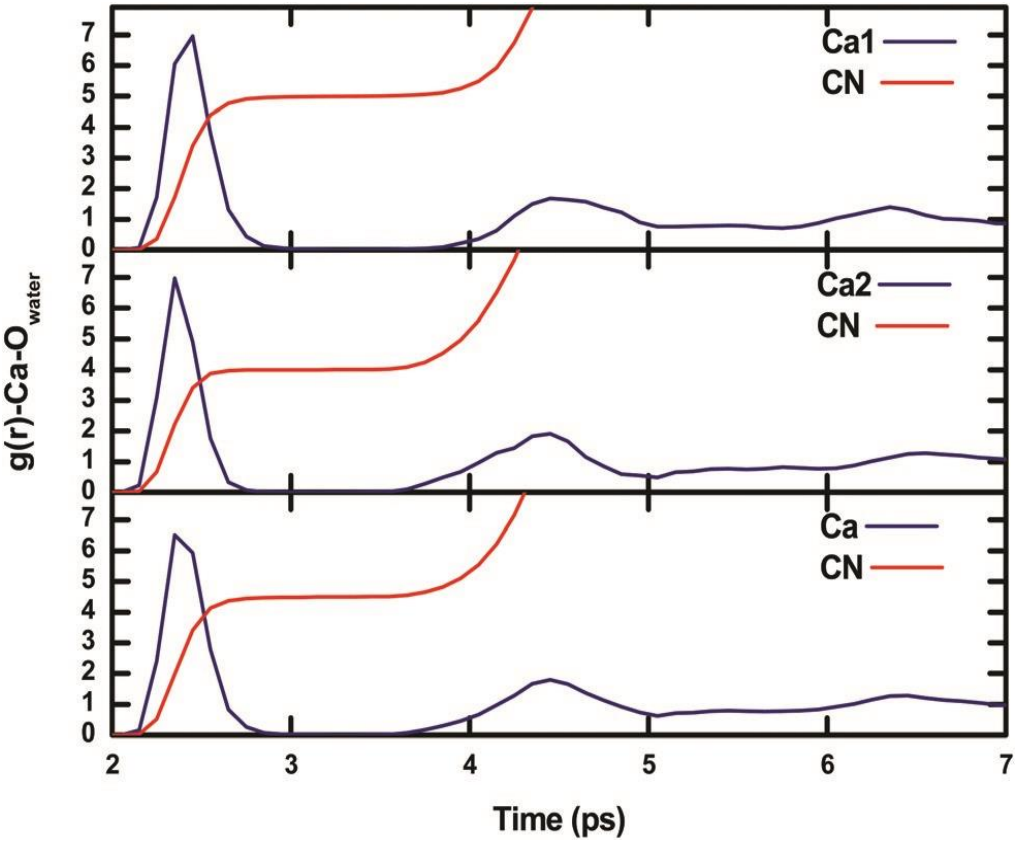

Figure 3.5 Radial distribution function (blue) and its integration (coordination number, CN; red) of water oxygen atoms around Ca1 and Ca2 separately (top two panels) and together (bottom panel), for 0.53 M $Ca_2UO_2(CO_3)_3$ in water.

3.4.3 Solvation environments of the two calcium ions

From the above discussion of the $Ca_2UO_2(CO_3)_3$ complex in water, we can clearly see that the difference between the two Ca ions is reflected in both the Ca–carbonate and the Ca– water interactions. The two interactions are in fact correlated: Ca1 has weaker binding with the $[UO_2(CO_3)_3]^{4-}$ complex, five molecules in the solvation shell, and a total of seven coordination bonds; Ca2 has stronger binding with the $[UO_2(CO_3)_3]^{4-}$ complex, four molecules in the solvation shell, and a total of six coordination bonds. Ca2 has a tighter solvation shell, so both average Ca2–O_{water} and Ca2–$O_{carbonate}$ distances are shorter than Ca1–O_{water} and Ca1–$O_{carbonate}$ distances, respectively.

What causes the asymmetry of binding and solvation between the two Ca ions in the $Ca_2UO_2(CO_3)_3$ complex? To answer this question, we analyzed the solvation environment of the complex from the views of Ca–carbonate, Ca–water, and carbonate–water interactions together, as shown in Fig. 3.6. One can see that there are three water molecules in the equatorial plane coordinating to Ca1, instead of two in the case of Ca2. The reason why Ca1 can have one more water molecule in the equatorial plane is that two of the three water molecules (water1 and water2 in Fig. 3.6) are interacting with both Ca1 and the carbonates. From Fig. 3.6, one can see that both water1 and water2 form hydrogen bonding (hb1 and hb2) with the two distal oxygen atoms of the two carbonate groups. These two (W2), while W1 is hydrogen bonded to O5 of carbonate1 (C1) and W2 is hydrogen bonded to O6 of carbonate2 (C2). As a result, the hydrogen bonding pulls the two carbonate groups closer (indicated by the two black arrows), so Ca1 is “squeezed” a little further away from hydrogen bonds pull water1 and water2 closer to the $Ca_2UO_2(CO_3)_3$ complex,

thereby leaving space for a third water molecule to enter the equatorial plane. In other words, it is the hydrogen-bonding network around the $Ca_2UO_2(CO_3)_3$ complex that leads to the difference in solvation and binding between the two Ca ions. We further examined the two lower concentrations and found the same solvation environment around the $Ca_2UO_2(CO_3)_3$ complex that confirmed the role of the hydrogen-bonding network in differentiating the two Ca ions in the $Ca_2UO_2(CO_3)_3$ complex.

To further explain the asymmetry between the two Ca ions, we show a schematic drawing (Fig. 3.7) of the equatorial plane around U. One can see that Ca1 is coordinated by both water1 (W1) and water2 O1 and O2. On the other hand, the O3–U–O4 angle becomes wider (indicated by the red double arrow), thereby allowing Ca2 to come closer to O3 and O4. Another way to think about this is via carbonate1. If Ca1 and Ca2 were symmetric in binding, the hydrogen bonding around carbonate1 (C1) would be symmetric. But as shown in Fig. 3.7, the hydrogen bonding around carbonate1 is asymmetric that eventually leads to the asymmetry in binding between Ca1 and Ca2.

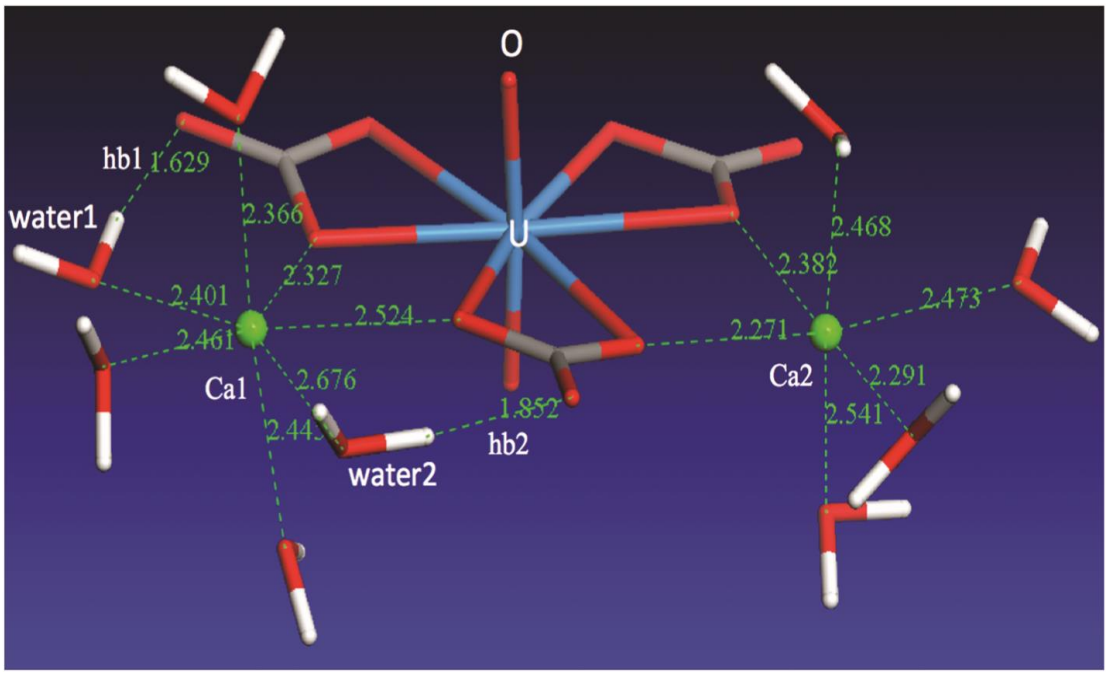

Figure 3.6 A snapshot of the $Ca_2UO_2(CO_3)_3$ complex in water at 0.53 M, showing only the water molecules directly interacting with the two Ca ions; hb1 and hb2 denote hydrogen bonding between the two water molecules (water1 and water2) and the two distal oxygen atoms of the two carbonate groups around Ca1; atom–atom distances are labeled in Å.

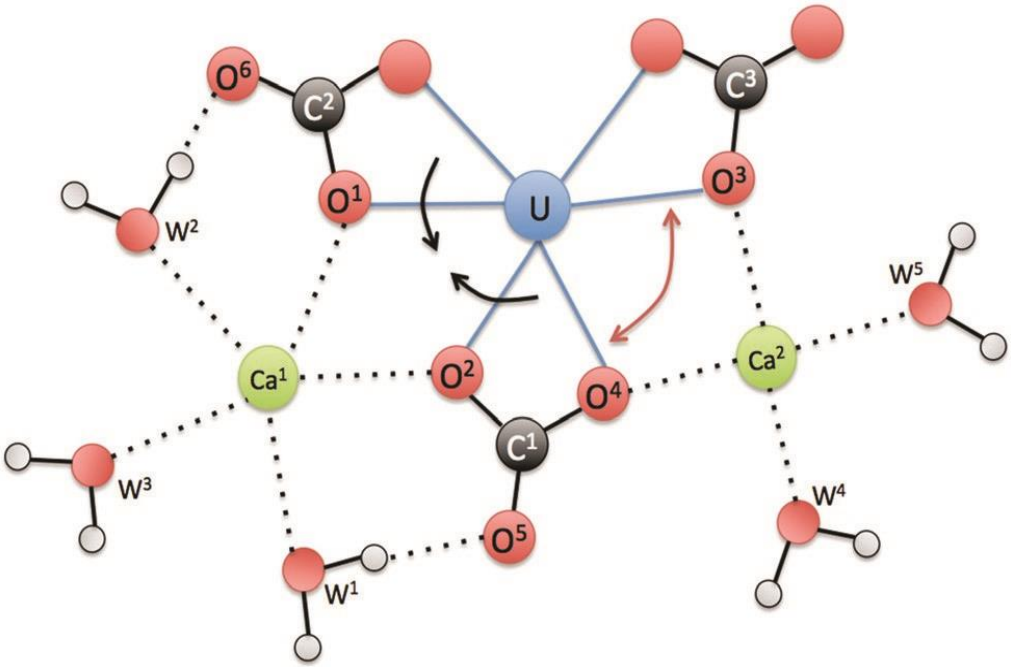

Figure 3.7 A schematic view of the equatorial plane around U for the $Ca_2UO_2(CO_3)_3$ complex in water. W stands for water.

3.4.4 Solvation environments of the whole complex

The discussion above shows the importance of the hydrogen bonding network in dictating the complex geometry. To further analyze this network, we examined the first solvation shell of the whole complex, namely, the water molecules in direct interaction with the complex. Since we have analyzed the water solvation around the two Ca ions, here we focus our discussion on the carbonate and uranyl oxygens. One can see from Fig. 3.8 that the top uranyl oxygen (OA1) has two water molecules hydrogen-bonded to it, while the bottom uranyl oxygen (OA2) has one. Moreover, one can see strong solvation of the carbonate distal oxygens by water: OD1 is hydrogen bonded by three water molecules, OD2 by four, OD3 by two. In addition, the two carbonate equatorial oxygens not interacting with the Ca ions are also solvated by water. Together with the water molecules around the two Ca ions, we found that there are 21 molecules in the first solvation shell. This large solvation shell indicates the necessity of using the explicit solvation model to address the structure, thermodynamics, and chemistry of the aqueous $Ca_2UO_2(CO_3)_3$ complex.

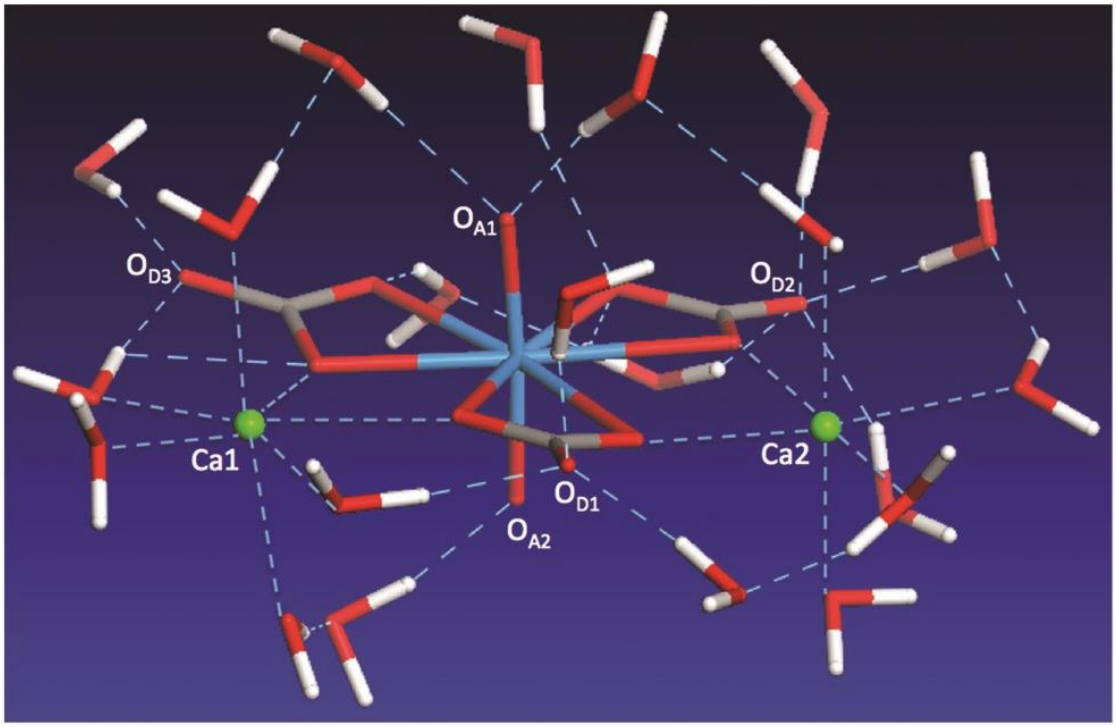

Figure 3.8 A snapshot of the first solvation shell of water molecules around the $Ca_2UO_2(CO_3)_3$ complex.

3.4.5 Ca–U distances

Besides speciation studies based on thermodynamics,10,12,13 the most direct characterization of the $Ca_2UO_2(CO_3)_3$ complex in water has been EXAFS studies of the coordination shells around the central U atom.10,11 Since the Ca–U distance is a key piece of information available from fitting the EXAFS spectra, we examined in detail the Ca–U distances for the network, we examined the first solvation shell of the whole complex, namely, the water molecules in direct interaction with the complex. Since we have analyzed the water solvation around the two Ca ions, here we focus our discussion on the carbonate and uranyl oxygens. One can see from Fig. 3.8 that the top uranyl oxygen (O_{A1}) has two water molecules hydrogen-bonded to it, while the bottom uranyl oxygen (O_{A2}) has one. Moreover, one can see strong solvation of the carbonate distal oxygens by water: O_{D1} is hydrogen bonded by three water molecules, O_{D2} by four, O_{D3} by two. In addition, the two carbonate equatorial oxygens not interacting with the Ca ions are also solvated by water. Together with the water molecules around the two Ca ions, we found that there are 21 molecules in the first solvation shell. This large solvation shell indicates the necessity of using the explicit solvation model to address the structure, thermodynamics, and chemistry of the aqueous $Ca_2UO_2(CO_3)_3$ complex.

$Ca_2UO_2(CO_3)_3$ complex in water. Fig. 3.9 shows the RDF of Ca ions around the U atom at three different concentrations. One can see that the asymmetry between the two Ca ions is also reflected in the Ca–U distances: the stronger-binding Ca2 is about 4.05 Å away from U and has a narrower distribution of the Ca2–U distance (standard deviation: 0.10 Å), while the weaker-binding Ca1 is about 4.15 Å away from U and has a broader distribution

of the Ca1–U distance (standard deviation: 0.12 Å). In addition, the three concentrations show very consistent distributions of Ca–U distances (Fig. 3.9).

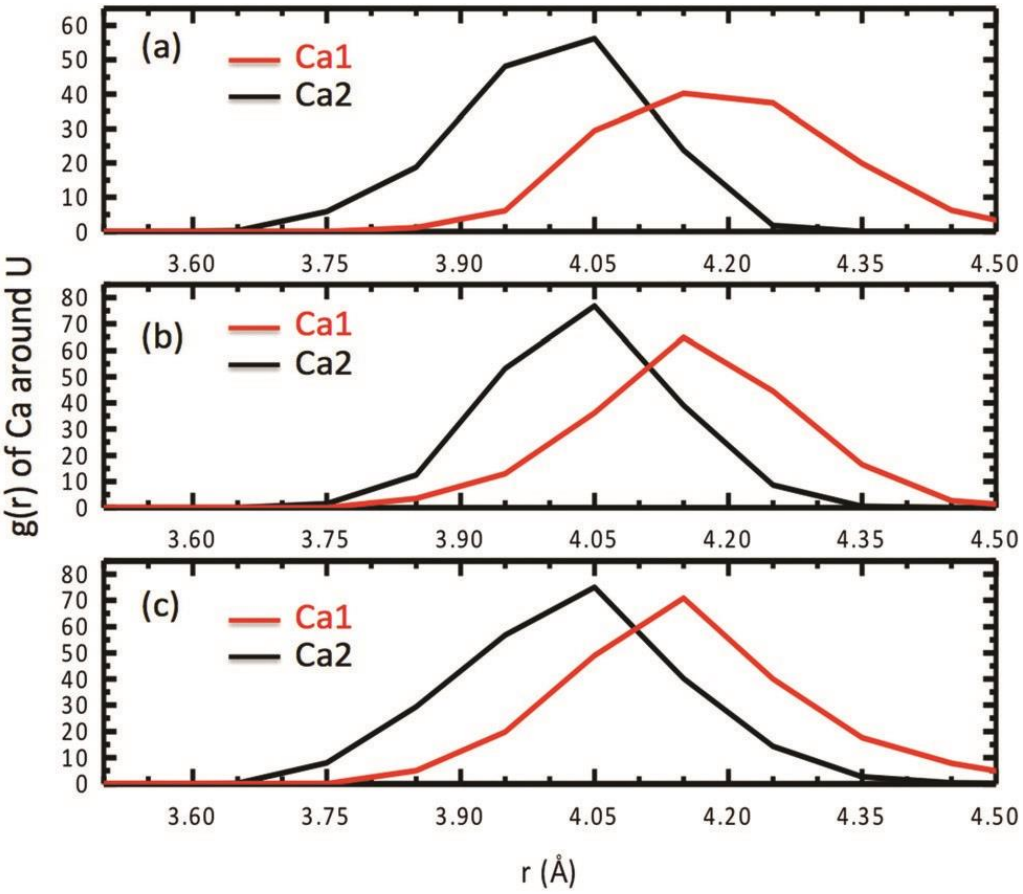

Figure 3.9 Radial distribution functions of Ca ions around the U atom for three different concentrations of $Ca_2UO_2(CO_3)_3$ in water: (a) 0.53; (b) 0.42; (c) 0.36 M.

3.4.6 Comparison with the literature

To our knowledge, the present study is the first DFT-MD simulation of the $Ca_2UO_2(CO_3)_3$ complex in water. It would be very informative to compare the present DFT-MD results with previous experiments and molecular-mechanical MD simulations (MM-MD) based on empirical force fields. For comparison with the experiment, we focus mainly on the liquid-phase EXAFS analysis on the structure of the $Ca_2UO_2(CO_3)_3$ complex from Kelly et al.[11] and Bernhard et al.[10] In the model fitting of the EXAFS spectra, they assumed that the two U–Ca distances are the same. To directly compare with their data, we therefore computed the total RDF of Ca ions around U and obtained an average Ca–U distance of about 4.07 Å at the peak of the RDF. Table 2 compares our DFT-MD simulation with the EXAFS data (EXAFS-1 from Kelly et al.[11] and EXAFS-2 from Bernhard et al.[10]) and the MM-MD simulations[26,39] for the key distances, including the U–Ca distance. One can see that the DFT-MD results are in good agreement with experiment. Our U–Ca distance is closer to the value from Kelly et al. (4.02 Å) than the one from Bernhard et al. (3.94 Å). Compared with the MM-MD simulation from Kerisit and Liu (MM-MD-1),[26] our DFT-MD simulation gives a U–O_{dis} distance much closer to the experiment. Compared with the MM-MD simulation from Doudou et al. (MM-MD-2),[39] our DFT-MD simulation yields a U–Ca distance in better agreement with the experiment.

Table 3.2 Comparison of key distances (in Å) for the $Ca_2UO_2(CO_3)_3$ complex in water among the present DFT-MD simulation, previous EXAFS data, and previous molecular-mechanical MD (MM-MD) simulations

Method	U–O_{eq}	U–O_{ax}	U–O_{dis}	U–Ca	U–C	Ref.
DFT-MD[a]	2.45 ± 0.12	1.85 ± 0.04	4.15 ± 0.14	4.07 ± 0.15	2.85 ± 0.10	p.w.
EXAFS-1	2.45 ± 0.01	1.78 ± 0.01	4.11 ± 0.07	4.02 ± 0.02	2.89 ± 0.01	11
EXAFS-2	2.44 ± 0.07	1.81 ± 0.03	4.22 ± 0.04	3.94 ± 0.09	2.90 ± 0.02	10
MM-MD-1	2.43	1.83	3.97	4.00	2.88	26
MM-MD-2i[b]	2.41	n/a	n/a	4.12	n/a	39
MM-MD-2ii[c]	2.41	n/a	n/a	4.18–4.84	n/a	39

a Present work (p.w.) for the concentration of 0.36 M: the distances are the peak positions in the radial distribution functions; the error bars are the standard deviations of the distances averaged over 15 ps trajectories. [b] A modified force field for calcite was used for the carbonate ion (ref. 39). [c] The AMBER GAFF force field was used for the carbonate ion (ref. 39). n/a: not provided in the reference.

3.4.7 Implications of the present findings

As we discussed above, a key finding from the present DFT-MD simulation is the asymmetry between the two Ca ions in the $Ca_2UO_2(CO_3)_3$ complex. A key issue here is whether and how often the two Ca ions can switch their bonding environments, namely, from Ca1-weak binding/Ca2-strong binding to Ca1strong binding/Ca2-weak binding. Such switching will be closely related to water exchange in the first solvation shell of the Ca ions. In our limited simulation timeframe (~50 ps), we did not observe such switching. This implies that our bruteforce DFT-MD is unlikely to address this issue due to its limited accessible timescale that is too short in comparison with the timescale of such switching. We are currently pursuing two lines of research to address this issue that will be published in the near future: (a) DFT-MD coupled with metadynamics to estimate the free-energy profile of such switching; (b) classical MD based on force fields to increase the timescale to about ~100 ns.

Despite the limited timescale of the present DFT-MD simulation, our finding of the asymmetry between the two Ca ions in the aqueous $Ca_2UO_2(CO_3)_3$ complex in the timescale of 10 to 100 ps may be confirmed by time-resolved EXAFS that can measure the variation in bond length in ps timescale.[40] Here we suggest an experiment to use time-resolved EXAFS to measure the Ca–U distances of the aqueous $Ca_2UO_2(CO_3)_3$ complex at ps snapshots. Another implication from our finding concerns dissociation of $Ca_2UO_2(CO_3)_3$ to $CaUO_2(CO_3)_3^{2-}$. Rao et al. found that in seawater conditions, $Ca_2UO_2(CO_3)_3$ and $CaUO_2(CO_3)_3^{2-}$ account for 58% and 18% of total U(VI), respectively.[13] In other words, $Ca_2UO_2(CO_3)_3$ is in equilibrium with $CaUO_2(CO_3)_3^{2-}$ and free Ca^{2+} in seawater. Our finding

suggests that Ca1 is much more likely to break away from $Ca_2UO_2(CO_3)_3$ than Ca2, to form $CaUO_2(CO_3)_3^{2-}$. This information will be useful for studies of the mechanism of $Ca_2UO_2(CO_3)_3$ dissociation with or without an attacking ligand. We plan to also use DFT-MD coupled with metadynamics to examine the free-energy profile of the dissociation mechanism. We suspect that there may exist some intermediate states of the $Ca_2UO_2(CO_3)_3$ complex before it becomes $[CaUO_2(CO_3)_3]^{2-}$ and free Ca^{2+}. For example, one likely configuration can have one Ca ion coordinating to one equatorial and one distal oxygen from the same carbonate group, while the other Ca ion coordinates "normally" to two equatorial oxygens of two different carbonate groups.

3.5 Conclusion

We have simulated the neutral $Ca_2UO_2(CO_3)_3$ complex in water using first principles molecular dynamics based on density functional theory (DFT-MD). Three concentrations (0.53, 0.42, and 0.36 M) feasible to DFT-MD simulations were examined. In the accessible timescale (~30 ps), we found that the structure of the $Ca_2UO_2(CO_3)_3$ complex is very stable where the two Ca ions bind to the carbonate groups on the same equatorial plane. We found that one Ca ion binds to the center $UO_2(CO_3)_3^{4-}$ anion more stronger than the other Ca ion. This asymmetry of binding between the two Ca ions is reflected in several aspects: the stronger binding Ca has shorter $Ca–O_{carbonate}$ bonds, shorter Ca–U distance, and four coordinating water molecules, while the weaker binding Ca has longer $Ca–O_{carbonate}$ bonds, longer Ca–U distance, and five coordinating water molecules. This finding suggests that using timeresolved EXAFS spectra may confirm the asymmetry in binding of the two Ca ions in the aqueous $Ca_2UO_2(CO_3)_3$ complex, since our DFT-MD

simulation shows in general good agreement in terms of key distances with the EXAFS experiments.

3.6 References

1. J. Kim, C. Tsouris, R. T. Mayes, Y. Oyola, T. Saito, C. J. Janke, S. Dai, E. Schneider and D. Sachde, Sep. Sci. Technol., 2013, 48, 367–387.

2. J. Kim, C. Tsouris, Y. Oyola, C. J. Janke, R. T. Mayes, S. Dai, G. Gill, L. J. Kuo, J. Wood, K. Y. Choe, E. Schneider and H. Lindner, Ind. Eng. Chem. Res., 2014, 53, 6076–6083.

3. S. Das, W. P. Liao, M. Flicker Byers, C. Tsouris, C. J. Janke, R. T. Mayes, E. Schneider, L. J. Kuo, J. R. Wood, G. A. Gill and S. Dai, Ind. Eng. Chem. Res., 2015, DOI: 10.1021/acs. iecr.5b03210.

4. T. Kago, A. Goto, K. Kusakabe and S. Morooka, Ind. Eng. Chem. Res., 1992, 31, 204–209.

5. A. Katakai, N. Seko, T. Kawakami, K. Saito and T. Sugo, J. Atom. Energy Soc. Jpn., 1998, 40, 878–880.

6. N. Seko, A. Katakai, S. Hasegawa, M. Tamada, N. Kasai, H. Takeda, T. Sugo and K. Saito, Nucl. Technol., 2003, 144, 274–278.

7. S. P. Kelley, P. S. Barber, P. H. K. Mullins and R. D. Rogers, Chem. Commun., 2014, 50, 12504–12507.

8. J. W. Morse, P. M. Shanbhag, A. Saito and G. R. Choppin, Chem. Geol., 1984, 42, 85–99.

9. G. Bernhard, G. Geipel, V. Brendler and H. Nitsche, Radiochim. Acta, 1996, 74, 87–91.

10. G. Bernhard, G. Geipel, T. Reich, V. Brendler, S. Amayri and H. Nitsche, Radiochim. Acta, 2001, 89, 511–518.

11. S. D. Kelly, K. M. Kemner and S. C. Brooks, Geochim.

12. Cosmochim. Acta, 2007, 71, 821–834.

13. J. Y. Lee and J. I. Yun, Dalton Trans., 2013, 42, 9862–9869. 13 F. Endrizzi and L. F. Rao, Chem. – Eur. J., 2014, 20, 14499– 14506.

14. 14 P. Di Bernardo, P. L. Zanonato, F. Benetollo, A. Melchior, M. Tolazzi and L. F. Rao, Inorg. Chem., 2012, 51, 9045–9055.

15. G. X. Tian, S. J. Teat and L. F. Rao, Dalton Trans., 2013, 42, 5690–5696.

16. C. Xu, G. X. Tian, S. J. Teat and L. F. Rao, Inorg. Chem., 2013, 52, 2750–2756.

17. H. B. Pan, W. S. Liao, C. M. Wai, Y. Oyola, C. J. Janke, G. X. Tian and L. F. Rao, Dalton Trans., 2014, 43, 10713– 10718.

18. X. Q. Sun, G. X. Tian, C. Xu, L. F. Rao, S. Vukovic, S. O. Kang and B. P. Hay, Dalton Trans., 2014, 43, 551–557.

19. C. J. Leggett and L. F. Rao, Polyhedron, 2015, 95, 54–59.

20. J. D. Kubicki, G. P. Halada, P. Jha and B. L. Phillips, Chem. Cent. J., 2009, 3, 10.

21. S. Vukovic, L. A. Watson, S. O. Kang, R. Custelcean and B. P. Hay, Inorg. Chem., 2012, 51, 3855–3859.

22. S. Vukovic and B. P. Hay, Inorg. Chem., 2013, 52, 7805–7810.

23. C. W. Abney, S. B. Liu and W. B. Lin, J. Phys. Chem. A, 2013, 117, 11558–11565.

24. A. O. Tirler, A. K. H. Weiss and T. S. Hofer, J. Phys. Chem. B, 2013, 117, 16174–16187.

25. A. O. Tirler and T. S. Hofer, J. Phys. Chem. B, 2014, 118, 12938–12951.

26. S. Kerisit and C. X. Liu, Geochim. Cosmochim. Acta, 2010, 74, 4937–4952.

27. S. Kerisit and C. X. Liu, J. Phys. Chem. A, 2013, 117, 6421– 6432.

28. G. Kresse and J. Hafner, Phys. Rev. B: Condens. Matter, 1993, 47, 558.

29. G. Kresse and J. Furthmuller, Comput. Mater. Sci., 1996, 6, 15–50.

30. P. E. Blöchl, Phys. Rev. B: Condens. Matter, 1994, 50, 17953.

31. G. Kresse and D. Joubert, Phys. Rev. B: Condens. Matter, 1999, 59, 1758.

32. J. P. Perdew, K. Burke and M. Ernzerhof, Phys. Rev. Lett., 1996, 77, 3865.

33. R. A. DiStasio, B. Santra, Z. F. Li, X. F. Wu and R. Car, J. Chem. Phys., 2014, 141, 084502.

34. K. Forster-Tonigold and A. Gross, J. Chem. Phys., 2014, 141, 064501.

35. R. G. Denning, J. Phys. Chem. A, 2007, 111, 4125–4143.

36. N. Kaltsoyannis, Inorg. Chem., 2000, 39, 6009–6017.

37. W. Humphrey, A. Dalke and K. Schulten, J. Mol. Graphics Modell., 1996, 14, 33–38.

38. K. Mereiter, Tscher. Miner. Petrog., 1982, 30, 277–288.

39. S. Doudou, K. Arumugam, D. J. Vaughan, F. R. Livens and N. A. Burton, Phys. Chem. Chem. Phys., 2011, 13, 11402– 11411.

40. J. Chen, H. Zhang and P. M. Rentzepis, J. Phys. Chem. A, 2010, 114, 2751–2756.

3.7 Supplementary

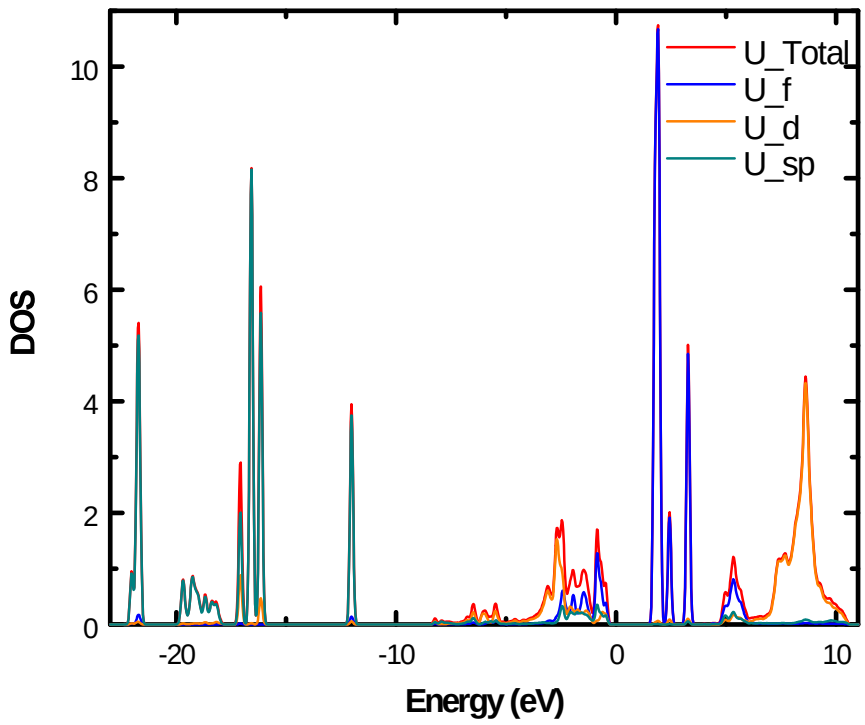

Figure S3.1 The orbital-resolved local density of states on the U atom from a snapshot of the $Ca_2UO_2(CO_3)_3$ complex in water. (Energy is relative to the Fermi level).

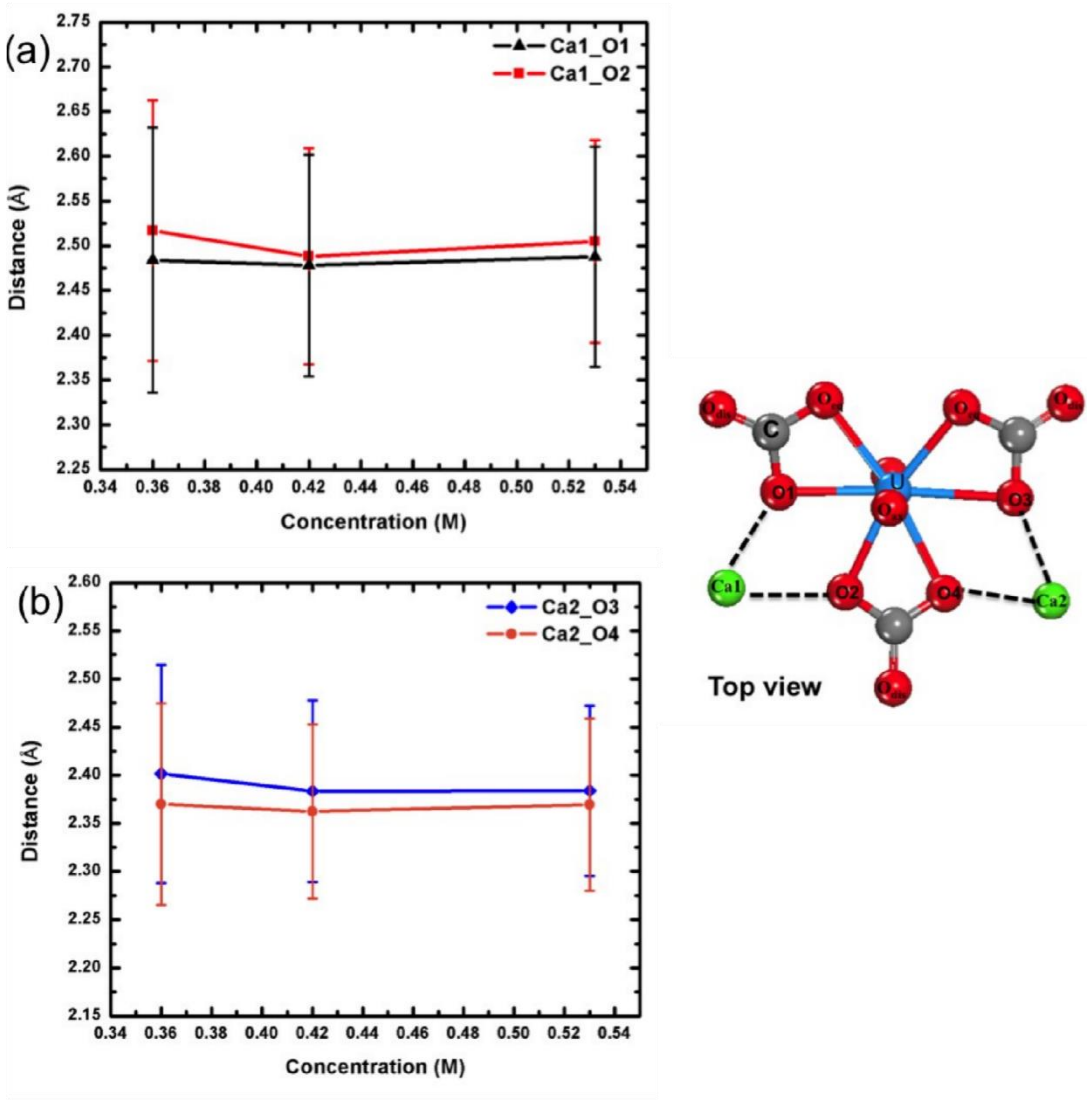

Figure S3.2. Averages and standard deviations of the four Ca-O_{eq} distances of the $Ca_2UO_2(CO_3)_3$ complex in water at three different concentrations over 15ps trajectories.

O H C U Ca
1.000000000000
14.603519439697 0.000000000000 0.000000000000
0.000000000000 14.603519439697 0.000000000000
0.000000000000 0.000000000000 14.603519439697
111 200 3 1 2
Direct
0.593620061874 0.933021485806 0.453137755394
0.554327249527 0.536954998970 0.011466519907
0.465799689293 0.697317838669 0.798811137676
0.006576189771 0.709684431553 0.184698224068
0.034945778549 0.957455396652 0.410463690758
0.233890354633 0.881254017353 0.163284704089
0.000695570023 0.063856616616 0.714212775230
0.914174795151 0.682639002800 0.452466398478
0.233282133937 0.082968249917 0.560798943043
0.730129182339 0.017852980644 0.676662623882
0.271041899920 0.140544354916 0.288121849298
0.466705471277 0.252164781094 0.454904764891
0.383879184723 0.793161153793 0.636618554592
0.255446940660 0.475655317307 0.128726825118
0.487190037966 0.911555051804 0.302578061819
0.634892463684 0.770762979984 0.828211963177
0.960335373878 0.172360792756 0.565022945404
0.228462114930 0.991124749184 0.845363438129
0.960539638996 0.980310857296 0.006558449939
0.982719004154 0.324289888144 0.852511644363
0.270570844412 0.588114559650 0.894954741001
0.892221987247 0.265639752150 0.006988190114
0.600026965141 0.279498606920 0.718969285488
0.443568527699 0.197150766850 0.292170792818
0.634455323219 0.206620395184 0.012221680023
0.197879523039 0.219460979104 0.426232576370
0.013574119657 0.417263209820 0.258487552404
0.444868952036 0.996420025826 0.020466219634
0.259789735079 0.911100685596 0.494928210974
0.129476085305 0.827666699886 0.589805722237
0.833791434765 0.663008689880 0.178773552179
0.168486014009 0.131094202399 0.730229914188
0.811612486839 0.103107392788 0.972420632839
0.951686382294 0.160817310214 0.251567751169
0.057818572968 0.902500271797 0.224847182631
0.660932302475 0.491055309772 0.863172590733
0.744669020176 0.998864471912 0.364622592926

0.270974308252 0.003794440068 0.032231688499
0.042458418757 0.133257478476 0.415059268475
0.253377318382 0.606188356876 0.558030545712
0.553100109100 0.704435765743 0.257722675800
0.720425546169 0.728602945805 0.657164931297
0.968072056770 0.895668983459 0.670366525650
0.545547068119 0.088229201734 0.904703915119
0.153376698494 0.303295969963 0.795864045620
0.529688596725 0.093957707286 0.541495680809
0.340605229139 0.466857194901 0.765215039253
0.597265481949 0.719727337360 0.986274063587
0.966428518295 0.790270388126 0.817973792553
0.488124638796 0.303822249174 0.124240331352
0.318161308765 0.313955008984 0.063308238983
0.211700931191 0.406521767378 0.460194230080
0.827234506607 0.728298842907 0.902440965176
0.373710513115 0.550024449825 0.027057329193
0.220050513744 0.162926226854 0.106102079153
0.755057930946 0.419595003128 0.213310912251
0.515285372734 0.057129830122 0.178837761283
0.997174203396 0.502014219761 0.900718748569
0.375130087137 0.307059735060 0.620615422726
0.143890276551 0.745301485062 0.760577559471
0.778153717518 0.411022305489 0.039664421231
0.573348164558 0.451201766729 0.183197200298
0.841519474983 0.110778808594 0.798037707806
0.774414300919 0.242296516895 0.284755706787
0.309774518013 0.958006143570 0.316936701536
0.421401083469 0.201340973377 0.776952207088
0.059191647917 0.580192923546 0.739947378635
0.753782749176 0.941349387169 0.179545074701
0.105675503612 0.581349730492 0.290479242802
0.921915888786 0.623748958111 0.618477284908
0.095661640167 0.887048423290 0.937078595161
0.853419601917 0.579591453075 0.008691160008
0.062085188925 0.709329009056 0.007088969927
0.411956220865 0.686487138271 0.141792893410
0.801371037960 0.576060295105 0.791602432728
0.314769834280 0.762434422970 0.875143706799
0.707206845284 0.125789806247 0.157725408673
0.396643459797 0.076543606818 0.655088484287
0.396432727575 0.927043616772 0.752234756947
0.159270584583 0.445514470339 0.667725026608
0.923000931740 0.995053589344 0.182015687227

0.686134696007 0.314061760902 0.858598887920
0.258474946022 0.714179217815 0.249887585640
0.913076996803 0.418977081776 0.401168316603
0.132140994072 0.555959761143 0.002264650073
0.557075977325 0.786905705929 0.548786997795
0.824069917202 0.407062649727 0.603165090084
0.836751461029 0.285355746746 0.743191242218
0.012507839128 0.376665860415 0.563445627689
0.685150325298 0.759295105934 0.143039301038
0.039185140282 0.157519221306 0.090830549598
0.335614353418 0.725673735142 0.440732598305
0.311517149210 0.312411248684 0.887952506542
0.801714539528 0.178947895765 0.460254371166
0.411806076765 0.817283749580 0.017807940021
0.605255544186 0.953776538372 0.791547775269
0.681513667107 0.167878285050 0.602160990238
0.869583010674 0.864192187786 0.407254278660
0.109015524387 0.675877034664 0.463604807854
0.821869492531 0.869565188885 0.585992515087
0.586342036724 0.389011472464 0.459951162338
0.507172465324 0.627530813217 0.465533643961
0.460192710161 0.497107416391 0.319706708193
0.718608498573 0.565661072731 0.482892304659
0.617708027363 0.517544388771 0.619365155697
0.391261100769 0.467371165752 0.451439321041
0.526138901711 0.531527757645 0.746589660645
0.653124213219 0.543181240559 0.345700532198
0.304984450340 0.472712069750 0.319055140018
0.806516766548 0.561506092548 0.353508412838
0.471238017082 0.503351688385 0.603055179119
0.653331696987 0.951024293900 0.429677277803
0.572684288025 0.993498444557 0.482234358788
0.575148642063 0.600326299667 0.005296160001
0.570418119431 0.516165435314 0.075731031597
0.526409924030 0.730952441692 0.793263852596
0.480694025755 0.637929618359 0.778434455395
0.017089420930 0.771388530731 0.207610026002
0.938067078590 0.702095627785 0.186847925186
0.074748232961 0.918731093407 0.444329679012
0.046188678592 0.025207549334 0.425499826670
0.272349745035 0.910243809223 0.212782993913
0.243238121271 0.914831101894 0.106423392892
0.956525385380 0.076945587993 0.764502882957
0.057532303035 0.093207232654 0.731005549431

0.894799470901 0.739156901836 0.420963734388
0.879328548908 0.639436185360 0.416910290718
0.264542013407 0.025192100555 0.540560364723
0.246768057346 0.131468564272 0.505541205406
0.762302100658 0.973801612854 0.634877443314
0.781295120716 0.044875584543 0.712905347347
0.338332086802 0.167222231627 0.285018503666
0.277631610632 0.072421222925 0.299022644758
0.501477420330 0.203890711069 0.489343345165
0.518063366413 0.297244995832 0.459557652473
0.442131340504 0.792281389236 0.597491383553
0.405993878841 0.750314891338 0.684528052807
0.264125823975 0.489809304476 0.195987984538
0.301908493042 0.511270284653 0.095779359341
0.528073132038 0.929039001465 0.351479917765
0.484696805477 0.846529006958 0.294693022966
0.623158514500 0.836623489857 0.826980888844
0.633688509464 0.751747190952 0.899548292160
0.900495350361 0.176495403051 0.544650495052
0.968339443207 0.128396674991 0.618534564972
0.284219294786 0.973956346512 0.811352431774
0.205218777061 0.045176770538 0.812497198582
0.940819263458 0.974504530430 0.073059290648
0.906136393547 0.022966399789 0.993739366531
0.952803492546 0.302275508642 0.907955586910
0.981406092644 0.392625033855 0.861274063587
0.267635405064 0.659223854542 0.892229557037
0.211457446218 0.571026623249 0.926979303360
0.847655713558 0.320018976927 0.021507278085
0.939409673214 0.265879899263 0.056753490120
0.539756178856 0.256909966469 0.730981171131
0.629996240139 0.295307815075 0.780874013901
0.461756169796 0.211948782206 0.358560234308
0.481214195490 0.147011935711 0.270428925753
0.601718544960 0.167368873954 0.967599928379
0.582431554794 0.242584496737 0.040027130395
0.223863780499 0.203773185611 0.360668927431
0.204819276929 0.284411549568 0.442634731531
0.974299669266 0.415295571089 0.317650556564
0.017408909276 0.353848904371 0.236820399761
0.468097090721 0.025093570352 0.081721641123
0.376066625118 0.013443060219 0.019031459466
0.222235634923 0.893197476864 0.549566447735
0.308195561171 0.864264130592 0.482849866152

0.149391397834 0.800951838493 0.649727642536
0.130000323057 0.776531457901 0.543150603771
0.775115787983 0.709546804428 0.175209790468
0.823989927769 0.611186444759 0.222344532609
0.173553377390 0.199742242694 0.745331883430
0.201700493693 0.116220742464 0.671299695969
0.687562584877 0.163609877229 0.104310646653
0.758722007275 0.098200730979 0.016322940588
0.888887465000 0.189258113503 0.266171216965
0.985824227333 0.162114351988 0.309252589941
0.122450441122 0.910789072514 0.208209693432
0.061788730323 0.925037443638 0.294803291559
0.620966792107 0.499033957720 0.918451786041
0.617044627666 0.507646143436 0.815047144890
0.725786387920 0.967934429646 0.303667604923
0.795153081417 0.951496005058 0.382024765015
0.247700482607 0.998584747314 0.966863274574
0.239938795567 0.055785380304 0.065858930349
0.012552860193 0.151894941926 0.471875905991
0.099606439471 0.168969750404 0.415907293558
0.282744288445 0.652688860893 0.516707777977
0.192062184215 0.622649252415 0.547313034534
0.510866641998 0.692444860935 0.204539999366
0.567618608475 0.647387504578 0.284870058298
0.700661301613 0.753708899021 0.720654070377
0.662431180477 0.752199053764 0.621631383896
0.019080210477 0.870226085186 0.631949365139
0.987602531910 0.964418053627 0.686627268791
0.503783941269 0.054195411503 0.949429214001
0.495610833168 0.117431469262 0.864648640156
0.209084615111 0.305352091789 0.840677201748
0.093992091715 0.308420985937 0.831775248051
0.478813201189 0.079757072031 0.586195588112
0.591048717499 0.120192393661 0.571676969528
0.299228399992 0.508326172829 0.797999441624
0.408154577017 0.487773239613 0.762548029423
0.533456802368 0.742153644562 0.981925547123
0.615657687187 0.749467849731 0.047092080116
0.004751259927 0.828094601631 0.860278308392
0.952491700649 0.822199821472 0.755842268467
0.481333047152 0.253620684147 0.168246775866
0.428946763277 0.305571526289 0.088103666902
0.285700500011 0.366510450840 0.093771293759
0.275781869888 0.264631509781 0.078363098204

0.147467717528 0.413749098778 0.455208063126
0.242002919316 0.425009936094 0.397778987885
0.773531615734 0.763864636421 0.893182396889
0.886122941971 0.759583473206 0.871737122536
0.438795715570 0.537881970406 0.010609920137
0.333777666092 0.562566161156 0.971317172050
0.149480417371 0.171444833279 0.102924473584
0.235828161240 0.162333205342 0.175611779094
0.686816632748 0.438396364450 0.220313087106
0.785433888435 0.457338035107 0.260530173779
0.514150738716 0.999864339828 0.218813598156
0.750521361828 0.189754635096 0.507601439953
0.055023331195 0.515844702721 0.943068146706
0.947671055794 0.536407113075 0.932224333286
0.406871736050 0.279627770185 0.568575501442
0.394397079945 0.270558089018 0.675563633442
0.081493683159 0.746375322342 0.795498073101
0.197032839060 0.747725069523 0.800114572048
0.845201909542 0.164963155985 0.989892423153
0.790340125561 0.467047065496 0.010484299622
0.786429464817 0.420152932405 0.110416457057
0.528440415859 0.480387926102 0.222403153777
0.827332973480 0.103818103671 0.865666687489
0.826790153980 0.172891974449 0.774375796318
0.765114247799 0.305231720209 0.256163597107
0.767941594124 0.236311465502 0.352106273174
0.265520960093 0.922983050346 0.354661613703
0.375166684389 0.935926973820 0.322644948959
0.405940443277 0.148966670036 0.740257382393
0.373208969831 0.221276164055 0.822364151478
0.093938104808 0.636199951172 0.752158641815
0.040151663125 0.564333796501 0.804487049580
0.821187555790 0.950970053673 0.195039421320
0.735506296158 0.006155760027 0.165894314647
0.072097286582 0.628029882908 0.255314350128
0.074557662010 0.520041167736 0.285541474819
0.978018581867 0.614401817322 0.657297968864
0.948344886303 0.640471339226 0.559945881367
0.039664469659 0.922744393349 0.955551743507
0.145026832819 0.917634606361 0.905475616455
0.849734067917 0.602053880692 0.073982648551
0.830898761749 0.632362544537 0.974239647388
0.027051009238 0.719680190086 0.069258756936
0.086563520133 0.769888341427 0.986338913441

0.412796467543 0.638794660568 0.094056181610
0.360477656126 0.668347239494 0.179482921958
0.755506098270 0.535710930824 0.827277541161
0.809460580349 0.633355796337 0.828243196011
0.337341398001 0.792206883430 0.931482613087
0.374400436878 0.740043759346 0.849018931389
0.582045078278 0.071931198239 0.171642050147
0.729858815670 0.161169454455 0.208821341395
0.400610953569 0.015099588782 0.689889431000
0.335251092911 0.084586687386 0.623035371304
0.392456084490 0.881062448025 0.702537715435
0.457117408514 0.921679615974 0.776449084282
0.121160343289 0.490139633417 0.697319030762
0.162863463163 0.397372156382 0.719359815121
0.917004942894 0.053063441068 0.221608489752
0.982762992382 0.963555395603 0.196487545967
0.685403466225 0.380648344755 0.868296086788
0.674911439419 0.280727773905 0.913427889347
0.212335392833 0.662701725960 0.241317883134
0.236225023866 0.770597815514 0.209804266691
0.888936996460 0.479029089212 0.388829886913
0.953771889210 0.424505233765 0.454043090343
0.155714869499 0.523223459721 0.055247820914
0.110746227205 0.623251020908 0.020103041083
0.568249344826 0.841310322285 0.511090397835
0.534776449203 0.734309852123 0.511048734188
0.825487971306 0.369842499495 0.661464273930
0.546069145203 0.391346484423 0.155189558864
0.899758398533 0.298422157764 0.772374808788
0.790743649006 0.299468845129 0.788793742657
0.997102260590 0.309039294720 0.568359732628
0.064736962318 0.393357634544 0.601149737835
0.699522793293 0.826810538769 0.149136066437
0.642397344112 0.742201149464 0.193892642856
0.010392280295 0.172180444002 0.153093844652
0.005732269958 0.105324320495 0.064606331289
0.298344016075 0.716670155525 0.381056964397
0.387683629990 0.691209137440 0.422980815172
0.313221991062 0.319208234549 0.956053018570
0.347707122564 0.356321871281 0.855335712433
0.889902055264 0.418224364519 0.595628499985
0.775594592094 0.121288031340 0.438056081533
0.388847053051 0.788352370262 0.074697978795
0.427755832672 0.880098044872 0.032998539507

0.655659794807 0.975299358368 0.751982092857
0.582507014275 0.003643929958 0.830064952374
0.710387885571 0.115723028779 0.634252607822
0.657184958458 0.208803296089 0.651875674725
0.852961421013 0.870045125484 0.473509758711
0.929200470448 0.895072221756 0.400887757540
0.040332179517 0.676624059677 0.455325692892
0.126489236951 0.636001348495 0.412106931210
0.789947688580 0.817655086517 0.620528936386
0.882632553577 0.878605127335 0.616486489773
0.381726771593 0.478561133146 0.360617876053
0.732322394848 0.555097639561 0.393235623837
0.538720726967 0.516548931599 0.658537805080
0.551728963852 0.509299874306 0.461286693811
0.306106209755 0.455522686243 0.585586428642

CHAPTER FOUR

Uranyl−Glutardiamidoxime Binding from First-Principles Molecular Dynamics, Classical Molecular Dynamics, and Free-Energy Simulations

4.1 Abstract

Exploring the structural interplay of ligands with uranyl can provide important knowledge for technology advances in uranium extraction from seawater. However, obtaining such chemical information is not an easy endeavor experimentally. From a plethora of computational methods, this work provides both microscopic insights and free-energy profiles of the binding between uranyl and deprotonated glutardiamidoxime (H_2B) for which experimental structural information is not available, despite H_2B being an important model ligand with an open-chain conformation for understanding aqueous uranium extraction chemistry. In our molecular dynamics (MD) simulations, we explicitly accounted for the water solvent as well as the Na^+ and Cl^- ions. We found that hydrogen bonding plays a critical role in dictating the binding configurations of B^{2-} and HB^- with uranyl. Simulated free energies of sequential ligand binding to form UO_2B, $[UO_2B_2]^{2-}$, and $[UO_2(HB)B]^-$ show very good agreement with the experimental values, lending support to our structural insights. The potential of mean force simulations showed the common feature of an important intermediate state where one end of the ligand binds to uranyl while the other end is solvated in water. Bringing the loose end of the ligand to bind with uranyl has

a free-energy barrier of 15−25 kJ/mol. The present work shows that the combined simulation approach can reveal key structural and thermodynamic insights toward a better understanding of aqueous complexation chemistry for uranium extraction from the sea.

4.2 Introduction

Earth's ocean contains 4.5 billion tons of uranium, but at a very low concentration of 3.3 ppb.[1] To ultimately tap into the ocean for a supply of nuclear fuel requires technology that is economically feasible.[2,3] Past studies have shown that uranium exists as a neutral complex of the uranyl species with carbonate and calcium, $Ca_2[UO_2(CO_3)_3]$.[4–9] The low concentration and relatively strong uranyl−carbonate interaction present a great challenge for uranium seawater extraction. State of the art technology employs a polymeric sorbent grafted with amidoxime ligands.[9,10] However, some transition-metal ions present in seawater compete against uranium for binding with the amidoxime ligands, especially vanadium.[11]

Two methods have been developed to graft amidoxime ligands on a polymer-fiber sorbent: radiation-induced graft polymerization (RIGP) and atom transfer radical polymerization (ATRP).[12,13] In RIGP, copolymerization of acrylonitrile (AN) and monomers such as substituted acrylic acids happens on the surface of electron-radiated polyethylene fiber, followed by reaction with hydroxylamine that converts the −CN group to the amidoxime groups.[14] It has been suggested that, on the basis of the reaction between acrylonitrile and hydroxylamine and the subsequent base conditioning, both open and cyclic forms of amidoxime exist on the fiber surface. Considering these two amidoxime

configurations, multiple possible coordination motifs with uranyl have been proposed, including monodentate or η^1 through the oxime oxygen, bidentate through the oxime oxygen and the amine nitrogen, and η^2 or side-on coordination through the N−O oximate bond. Recent extended X-ray absorption fine structure (EXAFS) studies suggest that fiber samples after contact with seawater show chelating binding interactions or a possible of mixed binding modes, instead of the η^2 mode.[15]

Although limited insight has been obtained for the real fiber sample regarding the binding mode, great progress has been made with small-molecule model ligands. For monoamidoxime ligands, both single-crystal structures and quantum-mechanical calculations have found the η^2 binding mode to uranyl.[16,17] Since the amidoxime ligands are formed from reaction of hydroxylamine with polyacrylonitrile, dioxime or diamidoxime ligands are a better model for the real sorbent. Rao et al. used two model ligands, glutarimidedioxime (H_2A) and glutardiamidoxime (H_2B), to represent the cyclic imide dioxime and the open-chain diamidoxime, respectively. They obtained binding free energies between the small-molecule ligands and the uranyl by potentiometry. For the cyclic H_2A, they were able to crystallize the complex and found that two HA^- ligands coordinate to UO_2^{2+} equatorially in a tridentate mode.[18–20] For the open H_2B, they could not obtain a single-crystal structure.[19] Thus, the binding mode of glutardiamidoxime (H_2B) and its deprotonated forms with uranyl remains unknown.

Since the cyclic form binds to vanadium very strongly,[21] the open-chain or acyclic form has been suggested to give higher uranium/vanadium selectivity[22] and it is important to find out the binding mode between H_2B and uranyl that might shed light on the U/V

selectivity. Toward this end, our work focuses on providing a thorough computational analysis to assist in determining the H_2B binding mode to uranyl complex from both first-principles and classical molecular dynamics simulations. More importantly, we will explicitly take into account the solvation environment including both the water molecules and the Na^+/Cl^- ions. To validate our computational models, we will also compare the simulated binding free energies with experiment to further check the viability of our models.

4.3 Computational Methods

4.3.1 First-Principles Molecular Dynamics

First-principles density functional theory (DFT) molecular dynamics (MD) via the Born− Oppenheimer approximation was performed using Vienna ab initio simulation package (VASP).[23,24] The Kohn−Sham equations were solved with the all-electron projected augmented wave (PAW) method.[25,26] We have chosen the Perdew−Burke−Ernzerhof (PBE) functional of the generalized-gradient approximation (GGA) for electron exchange and correlation.[27] This DFT-MD method has been employed previously to address uranyl in water.[4,28] Two ligands and one uranyl group in a 100-water periodic box at a density of 1.14 g/cm^3 was simulated by NVT at 300 K for 10 ps. It is well-known that the PBE functional tends to overstructure water, leading a frozen solution eventually; therefore, we checked the diffusivity of the water molecules not coordinating to the uranyl−ligand complex and found it to be close to 1×10^{-9} m^2/s. This is on the same order of magnitude as the measured self-diffusion coefficient of liquid water at 300 K (2.6

$\times 10^{-9}$ m^2/s),[29] so the water solvent remains liquid in our DFT-PBEMD simulation at 300 K.

4.3.2 Gas-Phase Quantum Mechanical Calculations

DFT calculations of isolated molecular complexes were performed with the TURBOMOLE package V6.5 with GGA-PBE functional along with the def-TZVP basis set, including def-ECP for uranium (given in the Supporting Information) and the resolution of the identity (RI) formalism with the corresponding auxiliary basis set.

4.3.3 Classical Simulation Systems and Force Field Parameters

To simulate the effect of ionic strength during MD simulations, we considered a water box where Na^+ and Cl^- ions were added to reach the experimental molar strength of 0.5 M NaCl. The TIP3P model was employed for water molecules, while the parameters for Na^+ and Cl^- ions were from a previous study.[30] The force field parameters of the solute molecules (UO_2^{2+}) and ligands (HB^- and B^{2-}; see Scheme 1) were generated from the AMBER 14 GAFF force field (generalized AMBER force field).[31] The partial atomic charges of these solutes (UO_2^{2+}, B^{2-}, BH^-) were obtained from the restrained electrostatic potential (RESP) charge at the B3LYP level of theory[32] with 6-31G(d) basis and antechamber suite.[33] UO_2^{2+}, HB^-, and B^{2-} were placed apart from each other into a periodic water box containing 6000 TIP3P water molecules. A cutoff of 12 Å was used for nonbonded interactions. Here we note that our uranyl force field parameters differ only slightly from and give performance similar to those from Guilbaud and Wipff.[34,35]

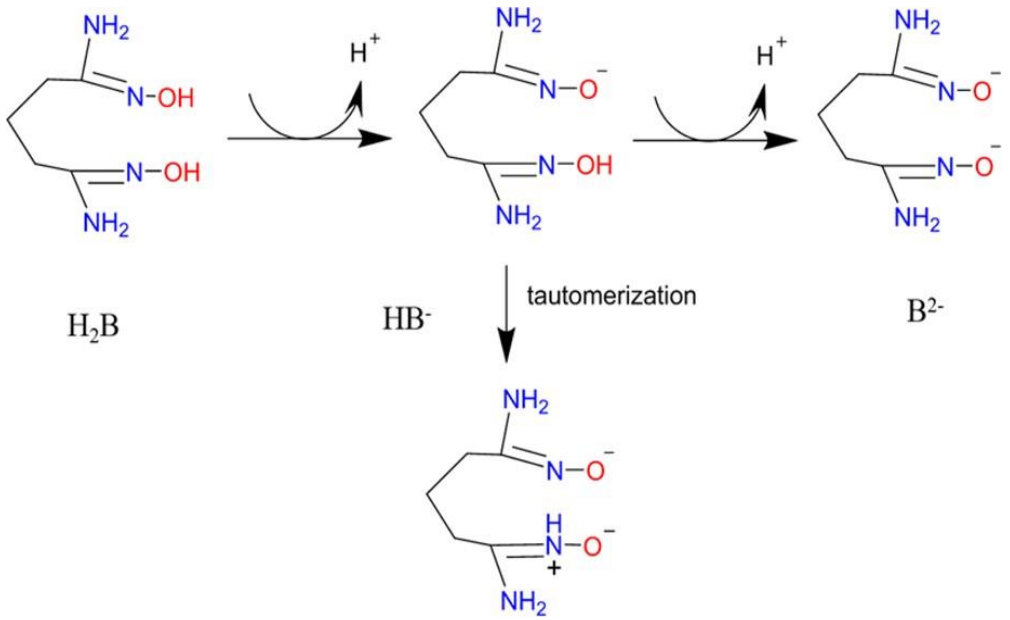

Figure 4.1 Structures of Glutardiamidoxime (H_2B) and Its Two Deprotonated Forms, HB^- and B^{2-}.

4.3.4 Classical Molecular Dynamics

First, 4000 cycles of minimization (2000 cycles of steepest descent and 2000 cycles of conjugate gradient) were carried out to relax the solvent, while solute atoms were constrained by a potential of 3000 kcal/(mol Å). Continually, a second minimization was conducted with solute atoms constrained by 500 kcal/(mol Å). A final, third minimization stage was implemented with 4000 cycles of energy minimization without constraints (2000 cycles of steepest descent and 2000 cycles of conjugated gradient). After the sequence of thorough minimizations of the solute molecule, the system was gradually heated from 0 to 300 K over 50 ps. Then, the cell was relaxed to 1.0 g/cm^3 with an NPT MD at 1 fs for 100−500 ps at a constant pressure of 1.0 bar and 300 K. Next, an NVT simulation was run for 500 ns at 300 K. All simulations were accomplished by applyin g the GPU-accelerated pmemd program in Amber 14.[36] During the production run, the temperature was kept constant using a Nose− Hoover thermostat at 300 K, and the geometry of the water molecules was held fix with the SHAKE algorithm.

4.3.5 Umbrella Sampling with the Weighted Histogram Analysis Method (WHAM)

To calculate the free energy of binding between uranyl and the ligands, we obtained the free-energy profile via potential of mean force (PMF) with our classical MD simulations by using umbrella sampling with the WHAM method.[37] The PMF simulations were carried out in a 2000-molecule water box in an ionic strength of I = 0.50 M NaCl solution. The reaction coordinate was taken as the distance from U to the oxime oxygen −C=N−O$^-$. The final equilibration structures were used for production simulations with no applied constraints. Umbrella sampling between 2.00 and 15.00 Å containing 75−96

windows (depending on the system) was carried out with a force constant ranging from 40 to 150 kcal/(mol Å^2). At the transition states, larger force constants (100−150 kcal/(mol Å^2)) and more windows of 0.1 Å bin size were added around the region to obtain sufficient sampling; for other regions, smaller force constants (40−100 kcal/(mol Å^2)) were used with window sizes of 0.2 Å. Each window was equilibrated between 6 and 10 ns, where the last 5 ns was used for production. Furthermore, the binding free energy was obtained from the PMF profile by following the previous method.[38,39]

4.4 Results & discussions

4.4.1 Binding of Glutardiamidoxime to Uranyl from GasPhase Quantum Mechanical Model

Previous experiments suggest that it is mainly the deprotonated forms (HB^- and B^{2-} in Scheme 1) of glutardiamidoxime binding to uranyl.[19] To provide a baseline understanding, we first examined the gasphase model of the binding at the DFT-PBE/def-TZVP level of theory, without the solvent. We found that UO_2^{2+} and B^{2-} binds via the two $-NO^-$ groups, both in the η^2 mode (Figure 4.1). This mode is in agreement with previous QM calculations of binding of UO_2^{2+} with amidoximate ligands.[40] To examine if the binding mode in Figure 4.1 is stable in solvation from water molecules, we used DFT-based first-principles MD to examine the UO_2B complex in a 100-water supercell.

4.4.2 First-Principles MD of UO_2B Complex in Water

Our DFT MD simulations show that the structure from Figure 4.1 (that is, the η^2 mode) can be maintained in the explicit water solvation with a slight change in the bond lengths (Figure 4.2a). However, we found that the complex with two η^1 binding modes

(Figure 4.2b), which is less stable in the gas phase, now becomes stable with the explicit solvation. This means that the hydrogen-bond network now changes the energy landscape of the complex in terms of the binding mode. This can be clearly seen in Figure 4.2: while the oxime nitrogen is not to water in the η^2 mode (Figure 4.2a), it is in the η^1 mode (Figure 4.2b). The preference of the oxime nitrogen to be solvated by water leads to the higher stability of the η^1 mode. In the η^2 binding mode, the O−N π bond as well as the O and N lone pairs of the oximate group dominate the interaction with U, as analyzed previously,[16] while in the η^1 binding mode the interaction is mainly via the lone pair on the O atom. To further understand the detailed binding mechanism with one additional ligand, to include the Na^+/Cl^- ions in the simulation, and also to address the relative stabilities of the different binding modes with water solvation, DFT-MD is unable to afford the system size and time scale needed to perform the free-energy simulations. Therefore, we turned to classical MD simulations.

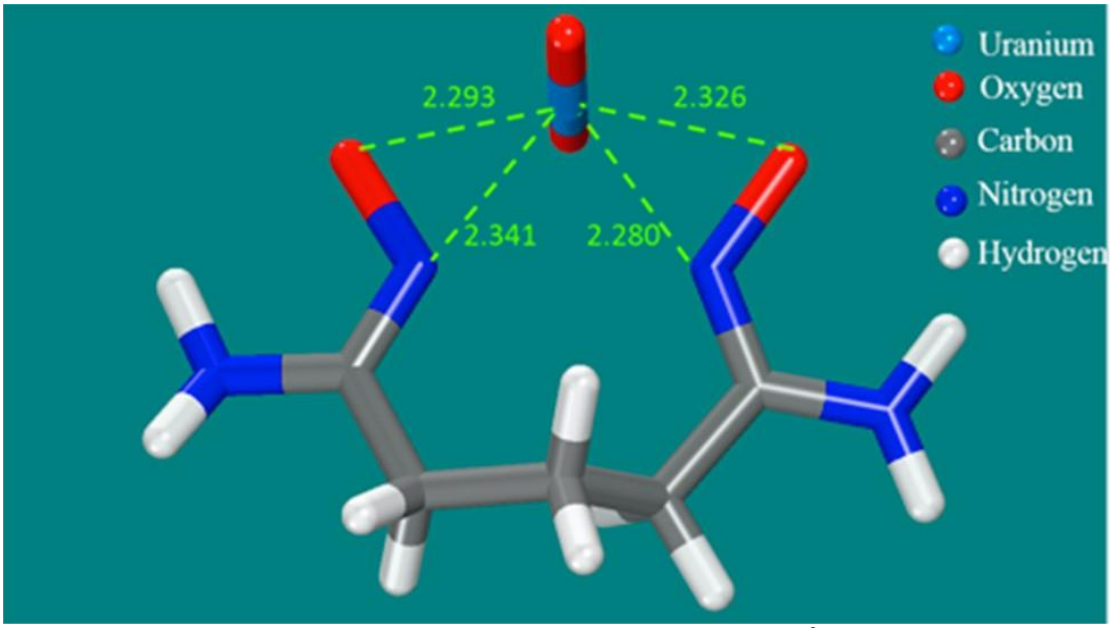

Figure 4.2 DFT-optimized gas phase structure of UO_2B where B^{2-} is double-deprotonated glutardiamidoxime (see Scheme 1).

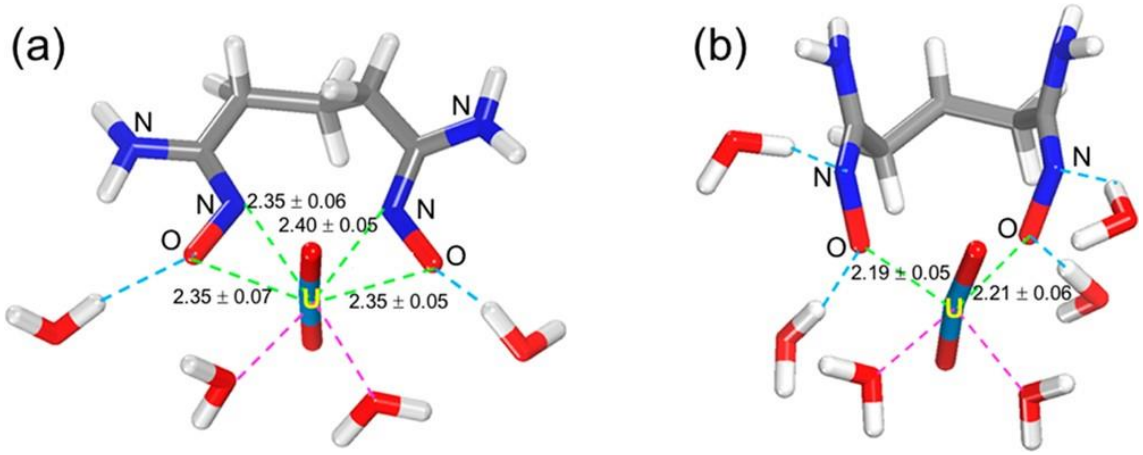

Figure 4.3 Typical structures from DFT-MD simulation of one UO_2B complex in 100 H_2O molecules: (a) η2-binding mode; (b) η1-binding mode. Average U−N and U−O distances are shown in Å.

4.4.3 Binding of Glutardiamidoxime to Uranyl from Classical MD

We placed UO_2^{2+} and B^{2-} ions far apart from each other in a large simulation cell to run brute-force MD simulations for over 500 ns. The binding is monitored by the U−O and U−N distances. The time evolution of the key distances is shown in Figure 4.3a, while the atom labels are shown in Figure 4.4a. The first complexation event happens at about 15 ns when one $-N-O^-$ end of the B^{2-} ligand attaches to UO_2^{2+}. Then around 35 ns, the second $-N-O^-$ end also binds to UO_2^{2+}, leading to a bidentate binding mode. Closer inspection of the U−O and U−N distances (Figure 4.3a, inset) shows that the two U−O distances average about 2.30 Å, while the two U−N distances average about 2.60 Å. A snapshot of the binding is shown in Figure 4.4a; one can see that the N atoms of the two oxime moieties interact with U weakly. This is further supported by the radial distribution analysis of the trajectory after the complex is formed (Figure 4.5). One can see that the N atoms of the $-N-O^-$ groups are rather loosely interacting with U, yielding an average U−N distance of 2.625 Å with a wide dispersion. This binding between the two $-N-O^-$ moieties and UO_2^{2+} (Figure 4) is different from the η^1 binding mode from our DFT MD results (Figure 4.2b) and is better described as a distorted η^2 binding mode. In addition, one can see that one $-NH_2$ group also coordinates to the uranyl in the snapshot (N3 in Figure 4.4a) with an average distance of about 2.50 Å (Figure 4.5). For comparison, the $-NH_2$ groups are not directly interacting with uranyl in our DFT-MD models (Figure 4.2). Further study such as through improving the force field is warranted to resolve this inconsistency between classical MD and DFT-MD simulations.

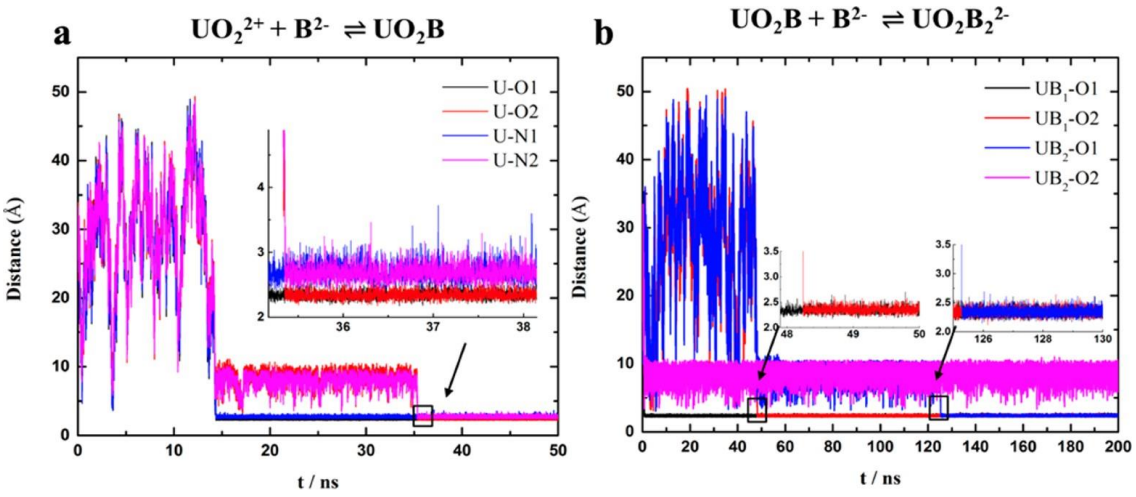

Figure 4.4 Classical molecular dynamics simulations of the binding as monitored by key U−O and U−N distances with time: (a) between UO_2^{2+} and B^{2-} ions, initially around 20 Å apart; (b) between UO_2^{2+} and two B^{2-} ions, initially about 20 Å apart, in pure water. The atom labels for (a) and (b) are shown in Figure 4.4a, b, respectively.

Next, we simulated the binding of two B^{2-} ligands with uranyl. Here we monitored the four U−O distances: two from each of the two B^{2-} ligands, B1 and B2. From Figure 4.3b, one can see that the bidentate binding with the B1 ligand is finished at 45 ns, while the B2 ligand has only one of its two O groups interacting with uranyl after 125 ns. In fact, the second ligand binds with uranyl via only one oxime oxygen even after 500 ns MD simulation. Figure 4.4b shows a snapshot of the binding in the $[UO_2B_2]^{2-}$ complex. One can see that the B1 ligand (the ligand on the right in Figure 4.4b) binds with UO_2^{2-} in a bidentate mode (the same as in the UO_2B complex) but the B2 ligand binds with one of its two amidoximate groups. The B2 ligand is rather linear with the nonbinding amidoximate group extended well away for the uranyl group. One thing to note is that the $-NH_2$ group of the binding amidoximate end of the B2 ligand also weakly coordinates to U with a distance of about 2.51 Å, a mode proposed previously as the adsorption mechanism of U(VI) to amidoxime-based polymers.[41,42] In our simulation, it seems that steric effects prevent the second ligand from forming a chelating binding with both oximate ends. This could be a kinetic issue that our classical MD, despite its 500 ns run, could not overcome.

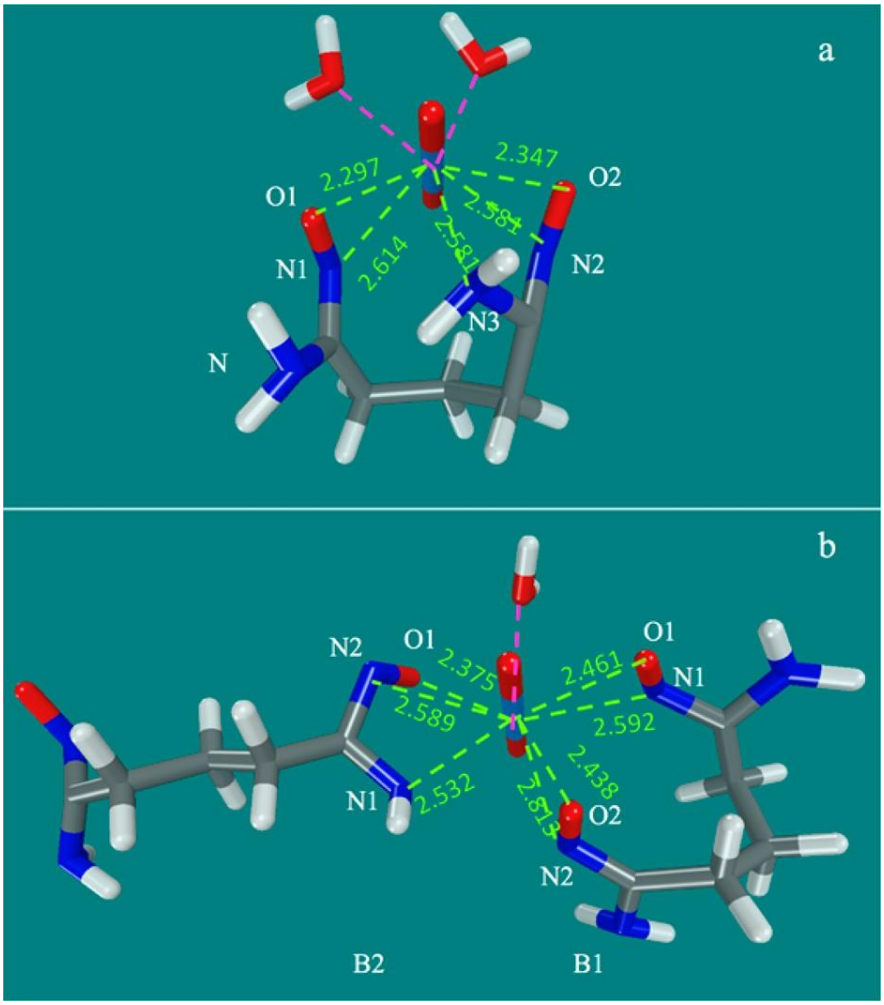

Figure 4.5 Snapshots of the binding modes after 500 ns classical MD simulations: (a) UO_2B; (b) $[UO_2B_2]^{2-}$ in pure water. Instantaneous U−N and U−O distances are labeled in Å.

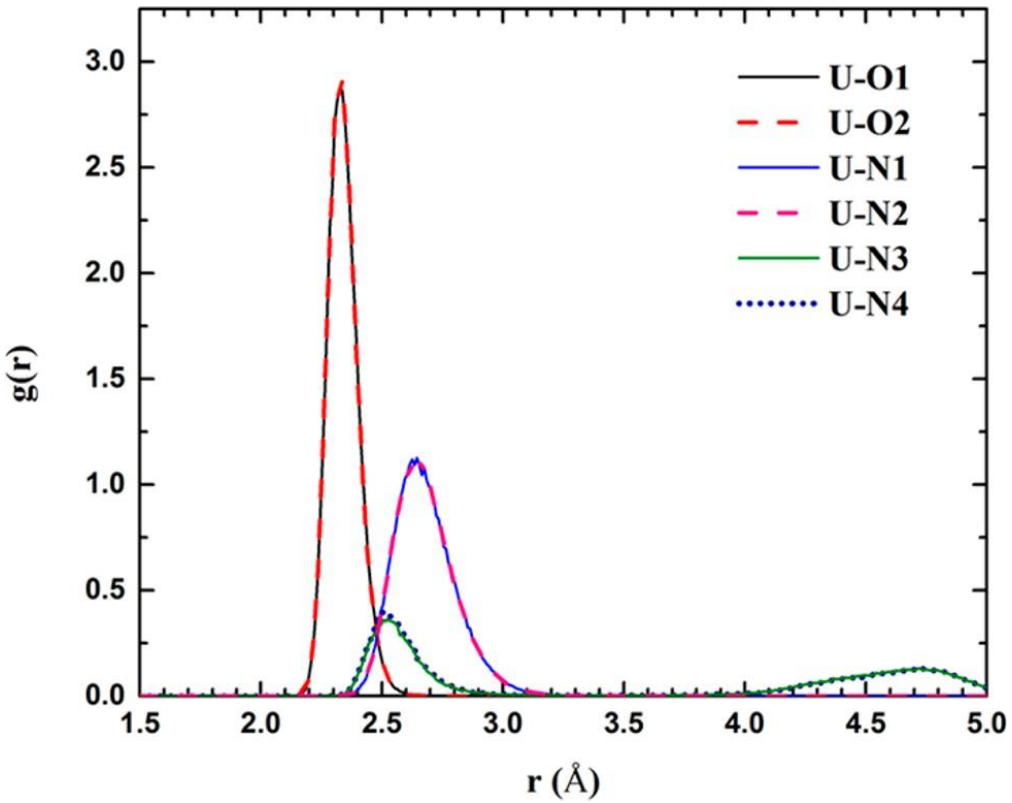

Figure 4.6 Radial distribution function of O and N atoms on the ligand around U for the structure of UO_2B in pure water after a 500 ns classical MD simulation. A snapshot of the binding structure and the atom labels are shown in Figure 4.4a.

4.4.4 Gas-Phase and Aqueous-Phase Structures for Uranyl Binding with Two Glutardiamidoxime Ligands

The structure of the $[UO_2B_2]^{2-}$ complex as found in our classical MD simulations and shown in Figure 4b may not be the most stable structure of the complex in water. To explore other conformations of binding, we first compared their gas-phase energetics at the DFT-PBE/def-TZVP level of theory, without the solvent. Figure 4.6a shows an isomer where the $[UO_2B_2]^{2-}$ complex binds to both B^{2-} ligands in a bidentate, η^1 mode. This isomer is metastable, and after perturbation and relaxation, the structure changes to that in Figure 4.6b, where one B^{2-} ligand binds in a double η^2 mode and the other binds in a single η^2 mode; the energy is lowered by 2.3 eV. To see whether the structures in Figure 4.6 are stable in an aqueous solution, we put them in water and performed classical MD simulations. We found that the structure in Figure 4.6b converged to the structure in Figure 4.4b, indicating again that the normal η^2 mode is less stable in an explicit water-solvation environment and becomes distorted. More interestingly, the structure in Figure 4.6a changes to that in Figure 4.7a, indicating the preference for a distorted η^2 structure in explicit water solvation. In this distorted η^2 structure, the average U−N distance is about 2.60 Å, while the average U−O distance is about 2.33 Å (Figure 4.7b). From integrating both U−N and U−O coordination in Figure 4.7b up to 2.70 Å, we found the coordination number of U to be 7; the extra coordination beyond the normal number of 6 could be due to our force field. Now that we have two stable structures of the $[UO_2B_2]^{2-}$ complex in water (Figure 4.4b and Figure 4.7a), it would be interesting to compare their free energies, as discussed next.

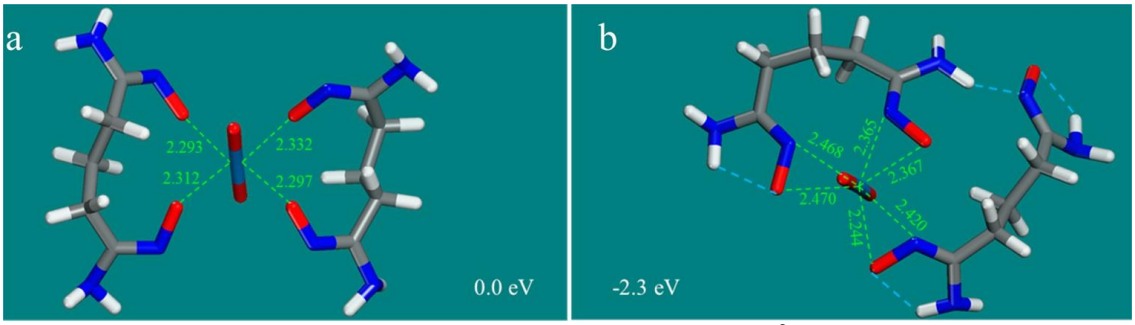

Figure 4.7 DFT-optimized gas-phase structures for $[UO_2B_2]^{2-}$: (a) η1 binding mode; (b) η^2 binding mode. The blue lines represent intramolecular hydrogen bonding.

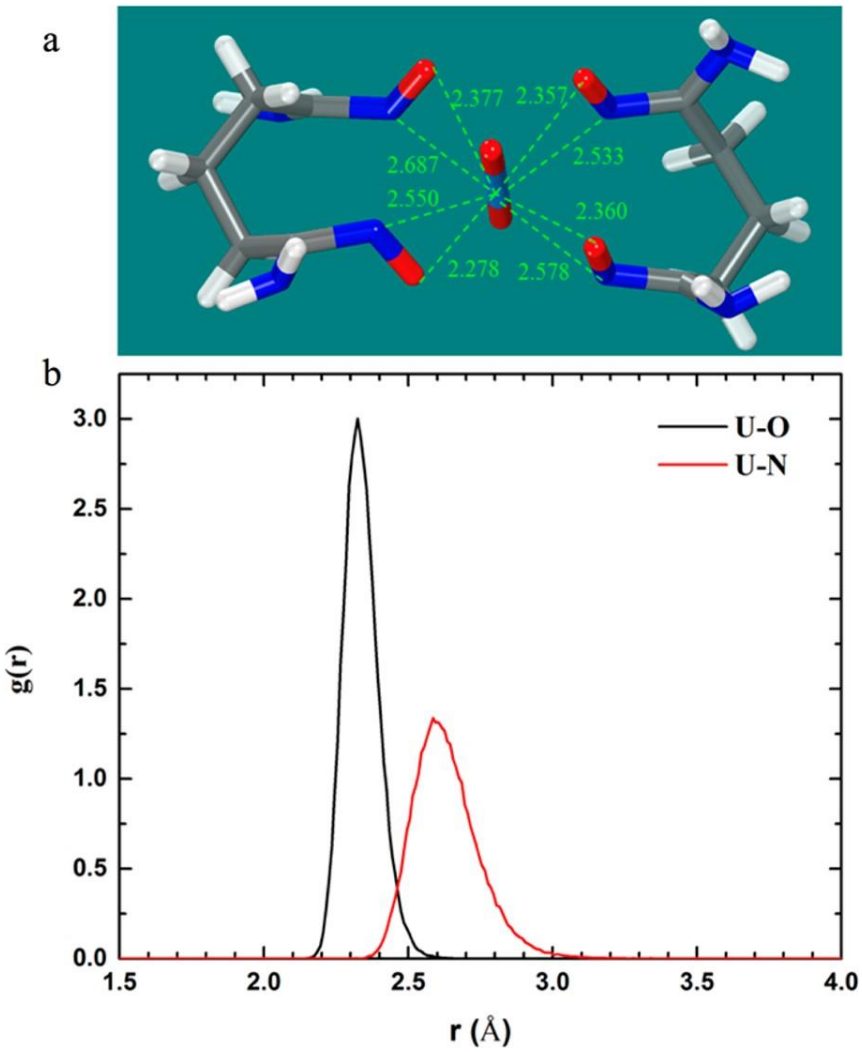

Figure 4.8 (a) Snapshot of the 4-fold distorted η2 binding structure of $[UO_2B_2]^{2-}$ after 100 ns classical MD simulation in 0.50 M NaCl. (b) Corresponding radial distribution function. Bond distances in (a) are from an instantaneous snapshot.

4.4.5 Free-Energy Simulations of Glutardiamidoxime−Uranyl Binding

Although there is no experimental structural information regarding the glutardiamidoxime−uranyl binding, the free energies of the sequential binding events have been measured. This provides a useful way to validate our atomistic insights from MD simulations above. Using umbrella sampling, we obtained the free energy profile via the potential of mean force (PMF) for the glutardiamidoxime−uranyl binding. Figure 4.8 shows the free-energy profiles for the association of a single ligand (UO_2^{2+} + B^{2-}), the association of the second ligand

In these simulations, we start with a bound complex and then begin to slowly pull one end of the ligand away from the uranyl using the U−O distance as a reaction coordinate. One can see that the three reactions have very similar PMF profiles. In the case of $UO_2B \rightarrow UO_2^{2+} + B^{2-}$ (red line in Figure 4.8), we started with the structure in Figure 4.4a and then broke the first U−O binding at about 3.0 Å with a free-energy barrier of about 45 kJ/mol; then the system reached a broad metastable or intermediate state between 4 and 10 Å, due to the flexibility of the $(CH_2)_3$ linker between the two amidoximate end groups, and then the second U−O binding broke between 10 and 12 Å. For the process of $[UO_2B_2]^{2-} \rightarrow UO_2B + B^{2-}$, we started with the structure for $[UO_2B_2]^{2-}$ in Figure 4.7a, where both B^{2-} ligands bind in a distorted η^2 mode, corresponding to the minimum at 2.35 Å in Figure 4.8 (black line). After breaking the first U−O binding with a free-energy barrier of about 35 kJ/ mol (at 3.0 Å in Figure 4.8; black line), we found that the structure changes to the configuration in Figure 4.4b, corresponding to the broad local minimum between 4 and 10 Å in Figure 8 whose energy is about 10 kJ/mol higher than that of the initial complex.

Conversely, there is a free energy barrier of about 15 kJ/mol for the conversion of the local minimum at ~9 Å to the bound complex at 2.35 Å in Figure 4.8, which explains why such a tightly bound mode of binding was not formed during the brute-force MD simulation of the binding of UO_2^{2+} with two B^{2-} ligands (Figure 4.3b)

Since Tian et al. showed that the most abundant species at seawater pH (8.3) is $[UO_2(HB)B]^-$,[19] we performed bruteforce MD simulation of UO_2^{2+} with two faraway B^{2-} and HB^- ligands and found that the B^{2-} ligand binds first followed by the HB^- ligand, in agreement with the stronger electrostatic attraction between UO_2^{2+} and B^{2-}. The brute-force MD yielded a binding mode as shown in Figure 4.9a, which corresponds to a reaction coordinate of 9 Å in Figure 4.8 (blue line). One can see that the oximate end of the HB^- ligand binds to UO_2^{2+} in a chelating mode with an average $U{-}NH_2$ distance of 2.50 Å and U−O distance of 2.30 Å (Figure 4.9b), while B^{2-} binds with two distorted η^2 modes. We also explored the configuration with the 4-fold complexation mode for $[UO_2(HB)B]^-$, which corresponds to a reaction coordinate of 2.35 Å in Figure 4.8 (blue line). Interestingly, unlike the case in $[UO_2B_2]^{2-}$, this configuration of 4-fold complexation is less stable than the 3fold binding mode (Figure 4.9a) for $[UO_2(HB)B]^-$.

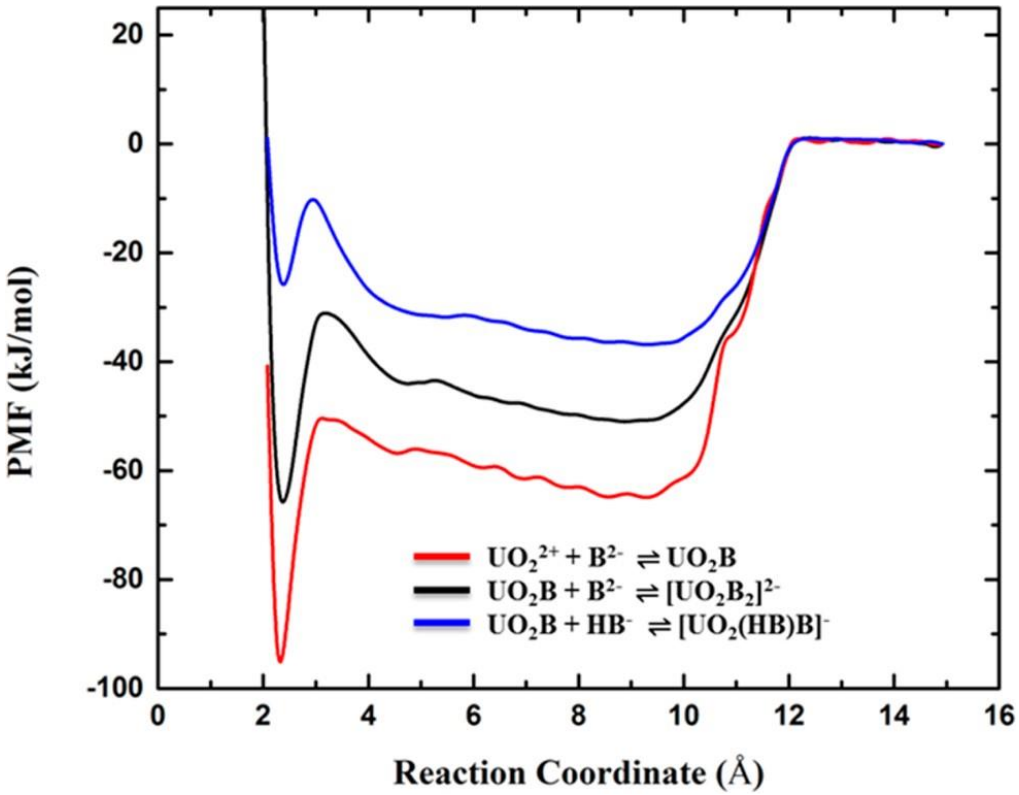

Figure 4.9 Free-energy profiles from the potential of mean force (PMF) for the binding events: UO_2^{2+} +B^{2-}; UO_2B + B^{2-}; UO_2B + HB^- in 0.50 M NaCl. The reaction coordinate is defined as U−O bond distance.

We note that the H atom is placed on the N atom of the oxime group of HB^- in Figure 4.9a (left end). This tautomerized form of oxime (see Scheme 1) has been proposed for $[UO_2(HB)B]^-$ by Tian et al. for the bound state.[19] We compared it with the untautomerized form (H on the O atom of oxime) for the step of the oxime end of HB^- binding with UO_2B (Figure S1 in the Supporting Information). We found that the tautomerized form binds more strongly by 15 kJ/mol than the untautomerized form, leading to a more stable $[UO_2(HB)B]^-$. This is why we used the tautomerized form of the oxime group in HB^- for our free energy simulations of $[UO_2(HB)B]^-$ formation. In the configuration of 4-fold complexation (at 2.35 Å in Figure 4.8, blue line) of the bound state, the tautomerized form of the oxime group in HB^- binds to U via the η^1 mode through the O atom, while the oximate end of HB^- and B^{2-} binds to U via the distorted η^2 mode (Figure S4.2 in the Supporting Information). In the free or unbound state of the oxime group in HB^- (Figure 4.9a), the untautomerized form (H on the O atom of oxime) is more stable; here we use the tautomerized form (H on the N atom of oxime) instead so that we can compare the free-energy difference between the free (Figure 4.9a) and bound (Figure S4.2) states with classical MD simulations that cannot describe the proton transfer or the tautomerization process. We hope to use DFT MD simulations to determine the free energy of the tautomerization process of the amidoxime group in the future.

4.4.6 Comparison Free Energies with Experimental

From the PMF profiles in Figure 4.8, we then followed an integration protocol from Chialvo et al.[38] to obtain the binding free energies. Table 1 compares the free energies for

the three could well capture the binding thermodynamics. This also in turn lends support to the binding modes as found above between UO_2^{2+} and B^{2-}. One can see that the first B^{2-} ligand binding is very strong, while the binding strength reduces by half for the second B^{2-} ligand. Binding of UO_2B with HB^- is slightly weaker than with B^{2-}.

Table 4.1 Comparison of Experimental and Simulated Free energies of Binding between Uranyl and the glutardiamidoxime (H_2B) Ligand at 298 K in 0.5 NaCl Aqueous Solution

reaction	ΔG_{exptl} (kJ/mol)[19]	ΔG_{calcd} (kJ/mol)
$UO_2^{2+} + B^{2-} \rightleftharpoons UO_2B$	−98.7	−91.9 ± 6.8
$UO_2B + B^{2-} \rightleftharpoons [UO_2B_2]^{2-}$	−50.2	−55.3 ± 5.1
$UO_2B + HB^- \rightleftharpoons [UO_2(HB)B]^-$	−39.8	−37.8 ± 2.0

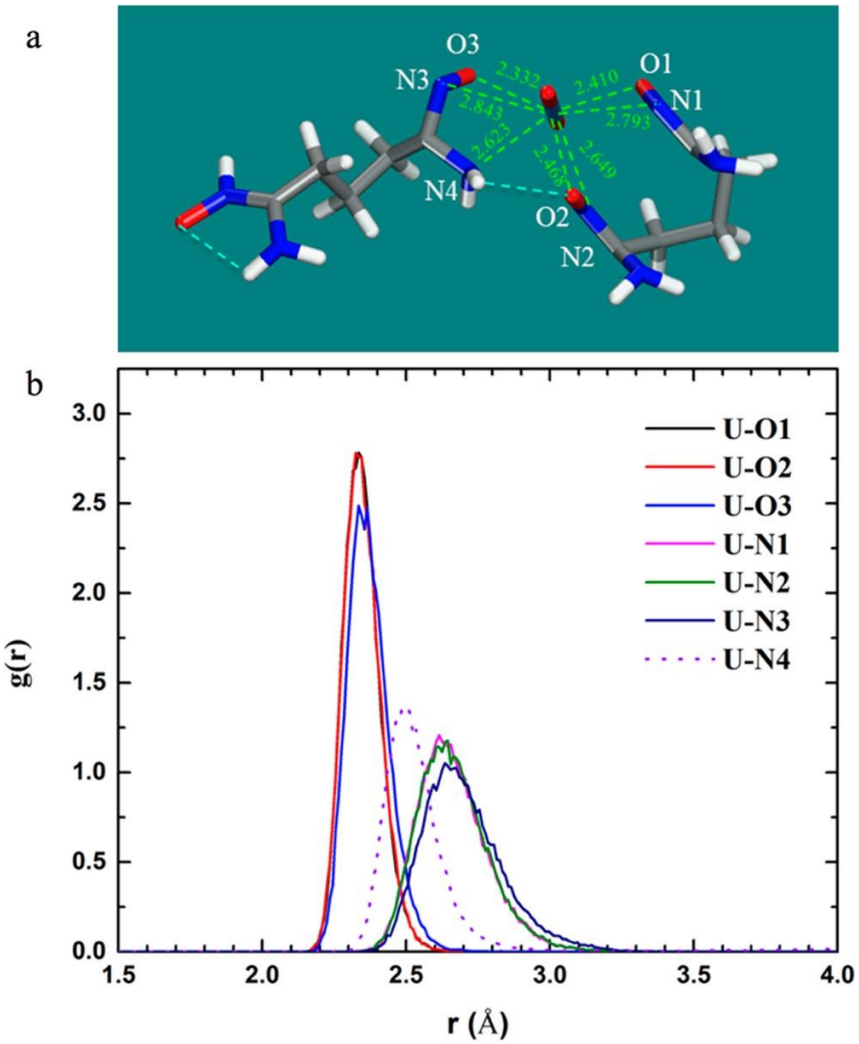

Figure 4.10 (a) Snapshot of the $[UO_2(HB)B]^-$ structure from a 50 ns classical MD simulation in 0.50 M NaCl;. (b) Corresponding radial distribution function. Bond distances in (a) are from an instantaneous snapshot.

4.4.7 Implications for the Experiment

The η^2 mode has been suggested by previous gas-phase and implicit-solvation models and also found in several single-crystal structures.[40,43] Our work shows that the aqueous solvation environment could be very different from those cases. On the other hand, the glutardiamidoxime ligand is a very simplified model in comparison to the real ligand binding environment in the polymeric sorbent, and more complex ligand models need to be developed to take into account the carboxylate group and a mixture of cyclic and open-chain configurations. The combined approach here shows a promising way to simulate the binding of such complex ligands with uranyl, although more work is needed to further improve the force field for a consistent picture between classical MD and DFT MD simulations.

4.5 Conclusions

In summary, we have used a suite of computational methods to shed light on the binding between uranyl and glutardiamidoxime (H_2B), an important model ligand with an open-chain conformation. From our molecular dynamics (MD) simulations with solvent as well as the Na^+ and Cl^- ions, we found that the binding configurations of B^{2-} with uranyl favor the 2-fold distorted η^2 binding between the oximate ends ($C{=}N{-}O^-$) and U, while HB^- prefers the chelating mode for the oximate end with the neutral end being solvated by water. We simulated the free energies of sequential ligand binding to form UO_2B, $[UO_2B_2]^{2-}$, and $[UO_2(HB)B]^-$ with umbrella sampling. Very good agreement with the experimental values was achieved, which corroborates our structural insights into the binding mode. The free-energy profiles as a function of the U−O distance from the potential

of mean force simulations showed similar features of a loose intermediate state separated from the tight-binding state by a sizable barrier (15−25 kJ/mol). Hence the present work revealed key structural and thermodynamic insights into the binding between uranyl and an open-chain amidoxime ligand in a simulated seawater that will be useful for further understanding of uranium extraction from the sea in a more realistic ligand and solvation environment.

4.6 References

1. Davies, R. V.; Kennedy, J.; Hill, K. M.; Mcilroy, R. W.; Spence, R. Extraction of Uranium from Sea Water. Nature 1964, 203, 1110−1115.

2. Das, S.; Liao, W. P.; Flicker Byers, M.; Tsouris, C.; Janke, C. J.; Mayes, R. T.; Schneider, E.; Kuo, L. J.; Wood, J. R.; Gill, G. A.; Dai, S. Alternative Alkaline Conditioning of Amidoxime Based Adsorbent for Uranium Extraction from Seawater. Ind. Eng. Chem. Res. 2016, 55, 4303−4312.

3. Kim, J.; Tsouris, C.; Oyola, Y.; Janke, C. J.; Mayes, R. T.; Dai, S.; Gill, G.; Kuo, L. J.; Wood, J.; Choe, K. Y.; Schneider, E.; Lindner, H. Uptake of Uranium from Seawater by Amidoxime-Based Polymeric Adsorbent: Field Experiments, Modeling, and Updated Economic Assessment. Ind. Eng. Chem. Res. 2014, 53, 6076−6083.

4. Priest, C.; Tian, Z. Q.; Jiang, D. E. First-principles Molecular Dynamics Simulation of the $Ca_2UO_2(CO_3)_3$ Complex in Water. Dalton Trans. 2016, 45, 9812−9819.

5. Wu, W. H.; Priest, C.; Zhou, J. W.; Peng, C. J.; Liu, H. L.; Jiang, D. E. Solvation of the $Ca_2UO_2(CO_3)_3$ Complex in Seawater from Classical Molecular Dynamics. J. Phys. Chem. B 2016, 120, 7227−7233.

6. Bernhard, G.; Geipel, G.; Reich, T.; Brendler, V.; Amayri, S.; Nitsche, H. Uranyl(VI) Carbonate Complex Formation: Validation of the $Ca_2UO_2(CO_3)_3$(aq.) Species. Radiochim. Acta 2001, 89, 511−518.

7. Endrizzi, F.; Rao, L. F. Chemical Speciation of Uranium(VI) in Marine Environments: Complexation of Calcium and Magnesium Ions with $[(UO_2)(CO_3)_3]$ and the Effect on the Extraction of Uranium from Seawater. Chem. - Eur. J. 2014, 20, 14499−14506.

8. Bernhard, G.; Geipel, G.; Brendler, V.; Nitsche, H. Speciation of Uranium in Seepage Waters of a Mine Tailing Pile Studied by TimeResolved Laser-Induced Fluorescence Spectroscopy (TRLFS). Radiochim. Acta 1996, 74, 87−91.

9. Das, S.; Brown, S.; Mayes, R. T.; Janke, C. J.; Tsouris, C.; Kuo, L. J.; Gill, G.; Dai, S. Novel Poly(imide dioxime) Sorbents: Development and Testing for Enhanced Extraction of Uranium from Natural Seawater. Chem. Eng. J. 2016, 298, 125−135.

10. Brown, S.; Yue, Y. F.; Kuo, L. J.; Mehio, N.; Li, M. J.; Gill, G.; Tsouris, C.; Mayes, R. T.; Saito, T.; Dai, S. Uranium Adsorbent Fibers Prepared by Atom-Transfer Radical Polymerization (ATRP) from Poly(vinyl chloride)-co-chlorinated Poly(vinyl chloride) (PVC-coCPVC) Fiber. Ind. Eng. Chem. Res. 2016, 55, 4139−4148.

11. Das, S.; Oyola, Y.; Mayes, R. T.; Janke, C. J.; Kuo, L. J.; Gill, G.; Wood, J. R.; Dai, S. Extracting Uranium from Seawater: Promising AF Series Adsorbents. Ind. Eng. Chem. Res. 2016, 55, 4110−4117.

12. Brown, S.; Chatterjee, S.; Li, M. J.; Yue, Y. F.; Tsouris, C.; Janke, C. J.; Saito, T.; Dai, S. Uranium Adsorbent Fibers Prepared by AtomTransfer Radical Polymerization from Chlorinated Polypropylene and Polyethylene Trunk Fibers. Ind. Eng. Chem. Res. 2016, 55, 4130−4138.

13. Oyola, Y.; Janke, C. J.; Dai, S. Synthesis, Development, and Testing of High-Surface-Area Polymer-Based Adsorbents for the Selective Recovery of Uranium from Seawater. Ind. Eng. Chem. Res. 2016, 55, 4149−4160.

14. Das, S.; Tsouris, C.; Zhang, C.; Kim, J.; Brown, S.; Oyola, Y.; Janke, C. J.; Mayes, R. T.; Kuo, L. J.; Wood, J. R.; Gill, G. A.; Dai, S. Enhancing Uranium Uptake by Amidoxime Adsorbent in Seawater: An Investigation for Optimum Alkaline Conditioning Parameters. Ind. Eng. Chem. Res. 2016, 55, 4294−4302.

15. Abney, C. W.; Mayes, R. T.; Piechowicz, M.; Lin, Z.; Bryantsev, V. S.; Veith, G. M.; Dai, S.; Lin, W. XAFS Investigation of Polyamidoxime-Bound Uranyl Contests the Paradigm from Small Molecule Studies. Energy Environ. Sci. 2016, 9, 448−453.

16. Abney, C. W.; Liu, S. B.; Lin, W. B. Tuning Amidoximate to Enhance Uranyl Binding: A Density Functional Theory Study. J. Phys. Chem. A 2013, 117, 11558−11565.

17. Guo, X. J.; Xiong, X. G.; Li, C.; Gong, H. F.; Huai, P.; Hu, J. T.; Jin, C.; Huang, L. L.; Wu, G. Z. DFT Investigations of Uranium Complexation with Amidoxime-, Carboxyl- and Mixed Amidoxime/ Carboxyl-Based Host Architectures for Sequestering Uranium from Seawater. Inorg. Chim. Acta 2016, 441, 117−125.

18. Astheimer, L.; Schenk, H. J.; Witte, E. G.; Schwochau, K. Development of Sorbers for the Recovery of Uranium from Seawater 0.2. The Accumulation of Uranium from

Seawater by Resins Containing Amidoxime and Imidoxime Functional-Groups. Sep. Sci. Technol. 1983, 18, 307−339.

19. Tian, G. X.; Teat, S. J.; Rao, L. F. Thermodynamic Studies of U(VI) Complexation with Glutardiamidoxime for Sequestration of Uranium from Seawater. Dalton Trans. 2013, 42, 5690−5696.

20. Tian, G. X.; Teat, S. J.; Zhang, Z. Y.; Rao, L. F. Sequestering Uranium from Seawater: Binding Strength and Modes of Uranyl Complexes with Glutarimidedioxime. Dalton Trans. 2012, 41, 11579− 11586.

21. Leggett, C. J.; Parker, B. F.; Teat, S. J.; Zhang, Z.; Dau, P. D.; Lukens, W. W.; Peterson, S. M.; Cardenas, A. J. P.; Warner, M. G.; Gibson, J. K.; Arnold, J.; Rao, L. Structural and Spectroscopic Studies of a Rare Non-Oxido V(v) Complex Crystallized from Aqueous Solution. Chem. Sci. 2016, 7, 2775−2786.

22. Brown, S. Private communication.

23. Kresse, G.; Hafner, J. Ab initio Molecular Dynamics for Liquid Metals. Phys. Rev. B: Condens. Matter Mater. Phys. 1993, 47, 558−561.

24. Kresse, G.; Furthmuller, J. Efficiency of Ab-Initio Total Energy Calculations for Metals and Semiconductors using a Plane-Wave Basis Set. Comput. Mater. Sci. 1996, 6, 15−50.

25. Blöchl, P. E. Projector Augmented-Wave Method. Phys. Rev. B: Condens. Matter Mater. Phys. 1994, 50, 17953−17979.

26. Kresse, G.; Joubert, D. From Ultrasoft Pseudopotentials to the Projector Augmented-Wave Method. Phys. Rev. B: Condens. Matter Mater. Phys. 1999, 59, 1758−1775.

27. Perdew, J. P.; Burke, K.; Ernzerhof, M. Generalized Gradient Approximation Made Simple. Phys. Rev. Lett. 1996, 77, 3865−3868.

28. Ferrier, M. G.; Batista, E. R.; Berg, J. M.; Birnbaum, E. R.; Cross, J. N.; Engle, J. W.; La Pierre, H. S.; Kozimor, S. A.; Pacheco, J. S. L.; Stein, B. W.; Stieber, S. C. E.; Wilson, J. J. Spectroscopic and Computational Investigation of Actinium Coordination Chemistry. Nat. Commun. 2016, 7, 12312.

29. Holz, M.; Heil, S. R.; Sacco, A. Temperature-dependent Selfdiffusion Coefficients of Water and Six Selected Molecular Liquids for Calibration in Accurate 1H NMR PFG Measurements. Phys. Chem. Chem. Phys. 2000, 2, 4740−4742.

30. Joung, I. S.; Cheatham, T. E. Determination of Alkali and Halide Monovalent Ion Parameters for Use in Explicitly Solvated Biomolecular Simulations. J. Phys. Chem. B 2008, 112, 9020−9041.

31. Wang, J. M.; Wolf, R. M.; Caldwell, J. W.; Kollman, P. A.; Case, D. A. Development and Testing of a General Amber Force Field. J. Comput. Chem. 2004, 25, 1157−1174.

32. Frisch, M. J.; Trucks, G. W.; Schlegel, H. B.; Scuseria, G. E.; Robb, M. A.; Cheeseman, J. R.; Scalmani, G.; Barone, V.; Mennucci, B.; Petersson, G. A., et al. Gaussian 09, Gaussian, Inc., Wallingford, CT, 2009.

33. Wang, J. M.; Wang, W.; Kollman, P. A.; Case, D. A. Automatic Atom Type and Bond type Perception in Molecular Mechanical Calculations. J. Mol. Graphics Modell. 2006, 25, 247−260.

34. Guilbaud, P.; Wipff, G. MD Simulations on UO_2^{2+} and Sr^{2+} Complexes with CMPO Derivatives in Aqueous Solution and at a Water/chloroform Interface. New J. Chem. 1996, 20, 631−642.

35. Bühl, M.; Wipff, G. Insights into Uranyl Chemistry from Molecular Dynamics Simulations. ChemPhysChem 2011, 12, 3095− 3105.

36. Case, D. A.; Babin, V.; Berryman, J. T.; Betz, R. M.; Cai, Q.; Cerutti, D. S.; Cheatham, T. E.; Darden, T. A.; Duke, R. E.; Gohlke, H., et al. AMBER 14; University of California, San Francisco, 2014.

37. Kumar, S.; Bouzida, D.; Swendsen, R. H.; Kollman, P. A.; Rosenberg, J. M. The Weighted Histogram Analysis Method for Free Energy Calculations on Biomolecules 0.1. The Method. J. Comput. Chem. 1992, 13, 1011−1021.

38. Chialvo, A. A.; Cummings, P. T.; Cochran, H. D.; Simonson, J. M.; Mesmer, R. E. Na+-Cl- Ion-Pair Association in Supercritical Water. J. Chem. Phys. 1995, 103, 9379−9387.

39. Doudou, S.; Arumugam, K.; Vaughan, D. J.; Livens, F. R.; Burton, N. A. Investigation of Ligand Exchange Reactions in Aqueous Uranyl Carbonate Complexes using Computational Approaches. Phys. Chem. Chem. Phys. 2011, 13, 11402−11411.

40. Vukovic, S.; Hay, B. P. De Novo Structure-Based Design of Bisamidoxime Uranophiles. Inorg. Chem. 2013, 52, 7805−7810.

41. Zhang, A. Y.; Asakura, T.; Uchiyama, G. The Adsorption Mechanism of Uranium(VI) from Seawater on a Macroporous Fibrous Polymeric Adsorbent Containing Amidoxime Chelating Functional Group. React. Funct. Polym. 2003, 57, 67−76.

42. Katragadda, S.; Gesser, H. D.; Chow, A. The Extraction of Uranium by Amidoximated orlon. Talanta 1997, 45, 257−263.

43. Qin, Z.; Shi, S. W.; Yang, C. T.; Wen, J.; Jia, J. P.; Zhang, X. F.; Yu, H. Z.; Wang, X. L. The Coordination of Amidoxime Ligands with Uranyl in the Gas Phase: A Mass Spectrometry and DFT Study. Dalton Trans. 2016, 45, 16413−16421.

4.7 Supplementary

1. Comparison of the tautomerized and untautomerized forms of the oxime end of HB^- in binding with UO_2B.

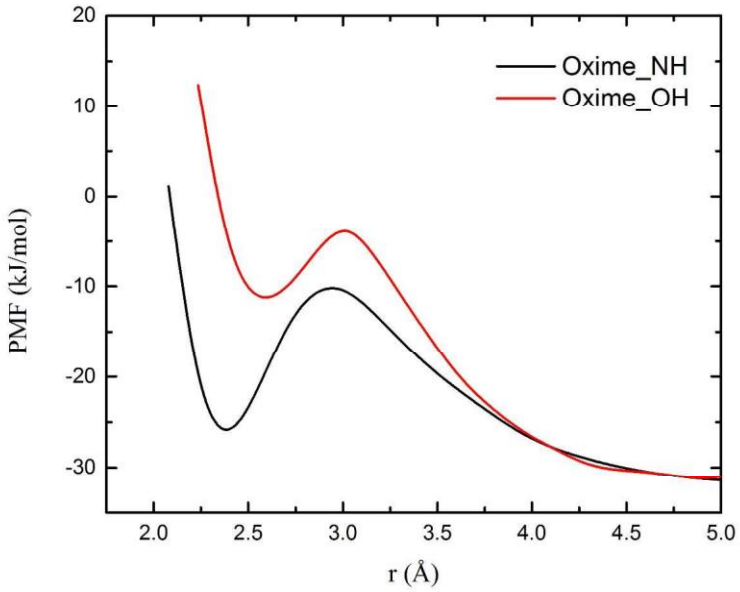

Figure S4.1 Potential of mean force for the step of the oxime end of HB^- in binding with UO_2B: Comparison of the tautomerized (oxime_NH) and untautomerized forms (oxime_OH). The reaction coordinate, r, is the distance between U and the oxime O.

2. Structure of $[UO_2(HB)B]^-$ with fourfold complexation and the tautomerized form of oxime on HB^- (indicated by the arrow in Figure S2a).

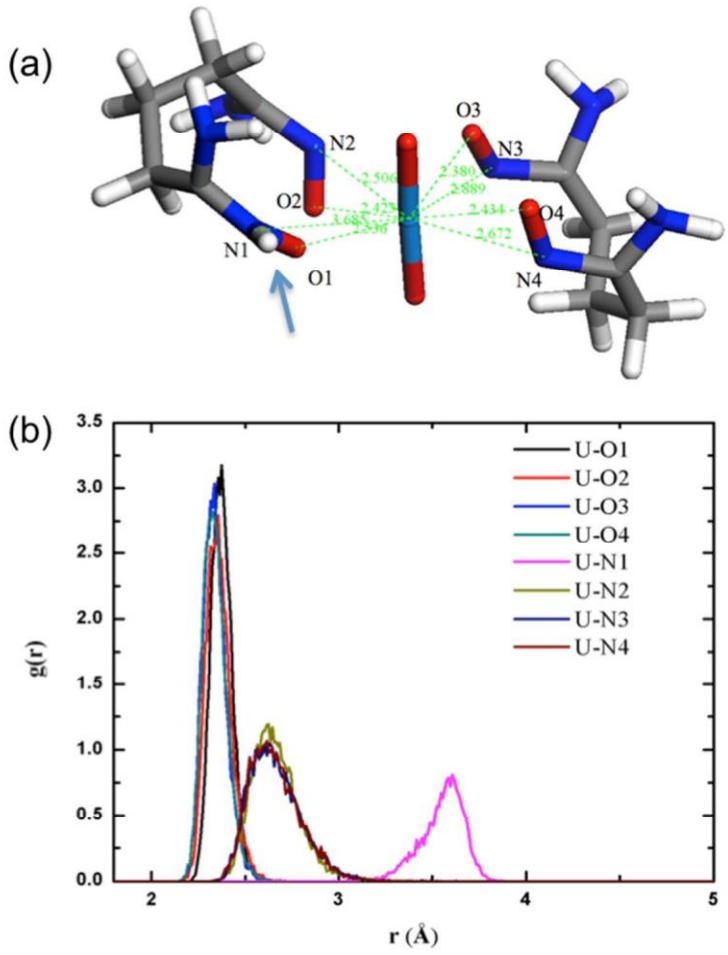

Figure S4.2. (a) Snapshot and instantaneous interatomic distances of the $[UO_2(HB)B]^-$ structure with fourfold complexation in 0.50 M NaCl, corresponding to the local minimum at 2.35 Å in Figure 8 (blue line); (b) the corresponding radial distribution function.

CHAPTER FIVE

Understanding the Binding of a Bifunctional Amidoximate-Carboxylate Ligand with Uranyl in Seawater from Simulations

5.1 Abstract

Extracting uranium from seawater remains a formidable challenge due to its extremely low concentration at 3.3 ppb. State-of-the-art polymeric sorbents employ both amidoxime and carboxylate groups on the side chains to achieve optimal U uptake and selectivity, but little is known about the synergistic effect between the two functional groups in binding with uranyl. Herein we simulated the binding of a model amidoxime-carboxylate bifunctional ligand with uranyl using a combination of theoretical methods. Gas-phase quantum-mechanical calculations show a slightly more stable carboxylate coordination than amidoxime, however ultimately binding simultaneously through a monodentate carboxylate binding mode with a η^2 amidoxime. Furthermore, the dimer formation with the bifunctional ligand shows a unique stability among different binding conformation. Lastly, free-energy binding energies for the consecutive binding for the bifunctional-ligand show a greater propensity for binding than that of pure AO containing ligand.

5.2 Introduction

Current terrestrial uranium reserves are limited to an estimate of ~6 million tons, and given today's rates of energy consumption, it has been predicted to be sufficient to sustain power generation for only the next century.[1] Although sparsely distributed homogenously across the oceans at minute concentrations of 3.3 ppb, scientists are very

interested in finding advanced adsorbents to tap into the huge reservoir containing 4.5 billion tons of uranium, a 1000 times more uranium than terrestrial reserves.[2] In seawater, uranium exists as the neutral $Ca_2[UO_2(CO_3)_3]$ species.[3-5] The challenge remains in designing adsorbents that have high uptake and high selectivity toward uranyl.

State-of-the-art sorbents for extraction of uranium from seawater are prepared via functionalizing the polymeric fibers with organic ligands such as amidoximes.[6] Studies have shown that efficient adsorption largely depends on AO-ligand density and hydrophilicity.[7] Currently, there are two common adsorbent preparation methods for poly(amidoxime) fabrication, radiation-induced graft polymerization (RIGP) and atom-transfer radical polymerization (ATRP). Although both contain advantages and disadvantages, RIGP is a mature refined poly(amidoxime)-type fabrication method used since the 1980s. A relatively young method, ATRP, allows for more chemical flexibility of composition and degree of polymerization and has shown.[7, 8]

The incorporation of an carboxylic acid co-monomer into the poly(amidoxime) adsorbents has been shown to increase uranium uptake.[9, 10] Experimentalists have optimized the molar ratio of amidoxime to carboxylate.[11, 12] Research suggests that the enhancement of uranium recovery from the bifunctional ligand containing both AO- and Ac- could be due to a synergetic effect. Density functional theory (DTF) calculations with implicit solvation models have been performed to unveil this synergetic effect. Some theoretical studies have shown that a protonated carboxylate (HAc) is conducive to the dissociation of the uranium-carbonate complex.[13-15] But the explicit solvation environment, important in uranyl speciation and ligand displacement, has not been considered.

This work aims to shed light on the synergetic effect between amidoxime and carboxylate groups in binding with uranyl, by using a model ligand and an explicit solvation environment. Especially, classical molecular dynamic (CMD) simulations coupled with free-energy methods (umbrella sampling with the weighted histogram analysis method)[16] will be utilized to investigate the modes and thermodynamics of the binding in a simulated seawater condition. Moreover, gas-phase quantum mechanical calculations and ab initio MD simulations have also been performed to provide a baseline understanding.

5.3 Computational Methods

5.3.1 Gas phase analysis

DFT calculations of isolated molecular complexes were performed with the TURBOMOLE package V6.5 with GGA-PBE functional along with the def-TZVP basis set, including def-ECP for uranium and the resolution of the identity (RI) formalism with the corresponding auxiliary basis set.

5.3.2 Ab initio molecular dynamics

First-principles density functional theory (DFT) molecular dynamics (MD) via the Born− Oppenheimer approximation was performed using Vienna ab initio simulation package (VASP).[17, 18] The Kohn−Sham equations were solved with the all-electron projected augmented wave (PAW) method.[19, 20] We have chosen the Perdew−Burke−Ernzerhof (PBE) functional of the generalized-gradient approximation (GGA) for electron exchange and correlation.[21] Two ligands and one uranyl group in a 100-

water periodic box at a density of 1.11 g/cm^3 was simulated by NVT at 300 K for a total of 20 ps.

5.3.3 Classical molecular dynamic parameters

To simulate the effect of ionic strength during MD simulations, we considereda water box where Na^+ and Cl^- ions were added to reach the experimental molar strength of 0.5 M NaCl. The TIP3P model was employed for water molecules, while the parameters for Na^+ and Cl^- ions were from a previous study.[22] The force field parameters of the solute molecules (UO_2^{2+}) and Figure 1, were generated from the AMBER 16 GAFF force field (generalized AMBER force field).[23] The partial atomic charges of these solutes (UO_2^{2+}, AO/AC) were obtained from the restrained electrostatic potential (RESP) charge at the B3LYP[24] level of theory with 6-31G(d) basis and antechamber suite.[25] UO_2^{2+} and the binfunctional-ligandcontaing AO/Ac were placed apart from each other into a periodic water box containing 2000 TIP3P water molecules. A cutoff of 12 Å was used for nonbonded interactions. Here we note that our uranyl force field parameters differ only slightly from and give performance similar to those from Guilbaud and Wipff.[26, 27]

5.3.4 Classical molecular dynamic procedure

First, 4000 cycles of minimization (2000 cycles of steepest descent and 2000 cycles of conjugate gradient) were carried out to relax the solvent, while solute atoms were constrained by a potential of 3000 kcal/(mol Å). Continually, a second minimization was conducted with solute atoms constrained by 500 kcal/(mol Å). A final, third minimization stage was implemented with 4000 cycles of energy minimization without constraints (2000

cycles of steepest descent and 2000 cycles of conjugated gradient). After the sequence of thorough minimizations of the solute molecule, the system was gradually heated from 0 to 300 K over 50 ps. Then, the cell was relaxed to 1.0 g/cm^3 with an NPT MD at 1 fs for 100−500 ps at a constant pressure of 1.0 bar and 300 K. Next, an NPT simulation was run for 500 ns at 300 K. All simulations were accomplished by applying the GPU-accelerated pmemd program in Amber 16.[28] During the production run, the temperature was kept constant using a Nose− Hoover thermostat at 300 K, and the geometry of the water molecules was held fix with the SHAKE algorithm.

5.3.5 Umbrella Sampling and Weighted Histogram Analysis Method (WHAM)

To calculate the free energy of binding between uranyl and the ligands, we obtained the free-energy profile via potential of mean force (PMF) with our classical MD simulations by using umbrella sampling with the WHAM method.[29] The PMF simulations were carried out in a 2000-molecule water box in an ionic strength of I = 0.50 M NaCl solution. The reaction coordinate was taken as the distance from U to the oxime oxygen −C=N−O$^-$. The final equilibration structures were used for production simulations with no applied constraints. Using pmd, umbrella sampling between 2.00 and 15.00 Å containing 81 windows (depending on the system) was carried out with a force constant ranging from 80 to 300 kcal/(mol Å^2). At the transition states, larger force constants (200−300 kcal mol^{-1} Å^{-2}) and more windows of 0.1 Å bin size were added around the region to obtain sufficient sampling; for other regions, smaller force constants (80−200 kcal mol^{-1} Å^{-2}) were used with window sizes of 0.2 Å. Each window was equilibrated for 2 ns, where the last 1 ns

was used for statistics. Furthermore, binding free-energy was calculated from the constructed PMFs from determined methods.[30, 31]

5.4 Results and discussion

5.4.1 Structure of the bifunctional model ligand

Since it is the deprotonated form of an amidoxime or carboxylic group that binds with uranyl, our model ligand simply comprises an amidoximate group and an acetate group connected by the $–(CH_2)_3$- linker (Figure 5.1). So the bifunctional ligand has an overall charge of -2.

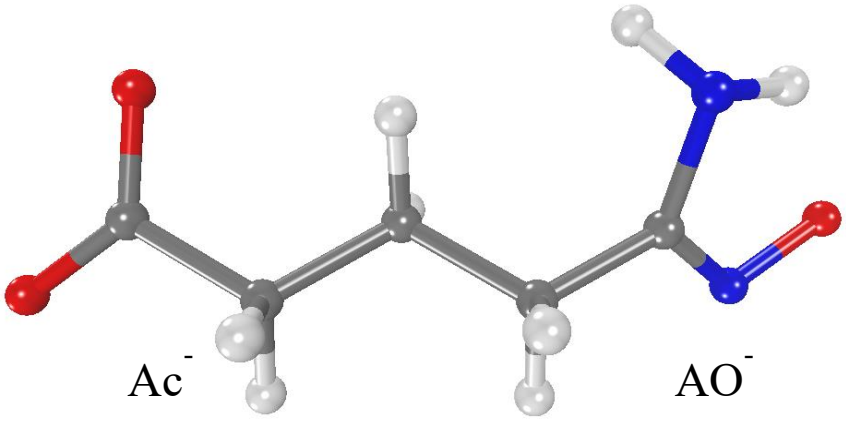

Figure 5.1. DFT-optimized gas-phase structure of the dianionic bifunctional ligand, denoted as C^{2-}. The ligand consists of a carboxylate (Ac^-) and amidoximate (AO^-) functional groups.

5.4.2 Binding of the bifunctional model ligand with uranyl in the gas phase

Various binding modes of a single bifunctional ligand to uranyl are compared in Figure 5.2. The most stable configuration consists of a bifunctional, chelate binding: AO^- in η^2 mode and Ac^- in monodentate mode. In the second most stable configuration, the binding mode of AO^- in η^2 changes to η^1 and the energy is 0.54 eV higher. The monofunctional binding configurations (with either AO^- or Ac^-, but not both) have much higher energies and are therefore much less stable.

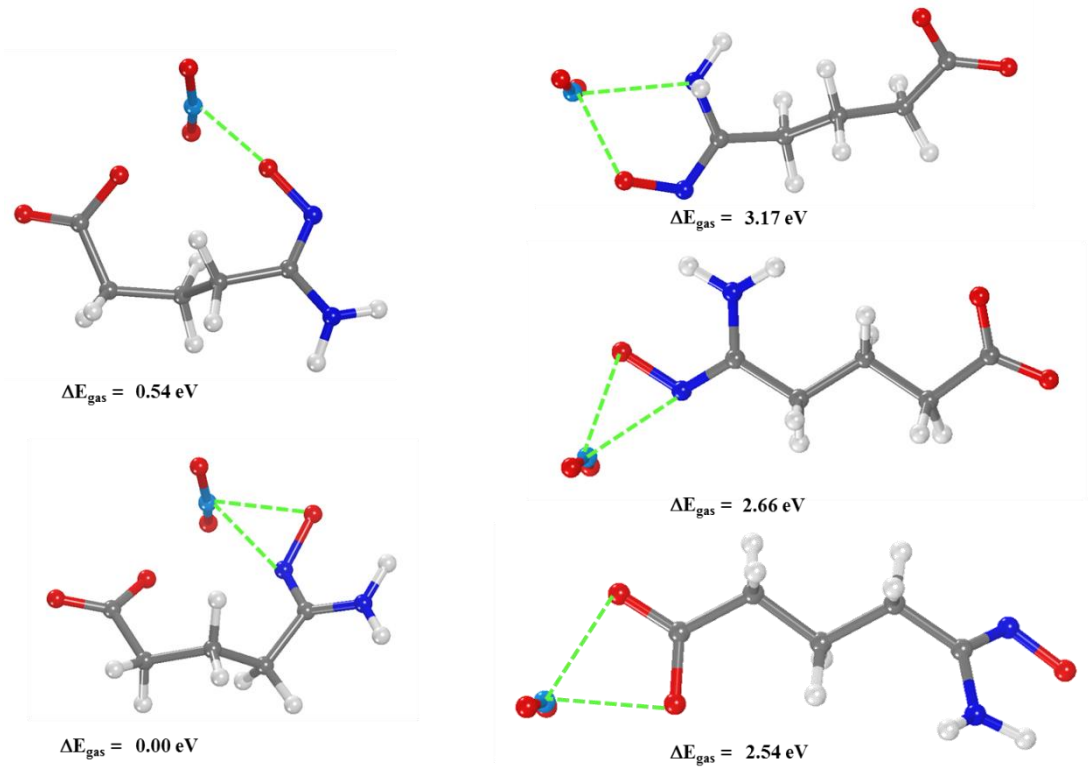

Figure 5.2 Assorted gas-phase optimizations of coordinated single bifunctional oligomer with uranyl, [UO_2(AO/Ac)].

5.4.3 Ab initio molecular dynamics Solvation of the UO_2C complex.

To gauge the stability of the uranyl-bifunctional ligand configuration in an explicit solvent model at the DFT-PBE level, we have performed AIMD simulations. Figure 5.3a shows a snapshot of the most stable gas-phase configuration of the UO_2C complex after a 15 ps production simulation in a pure water box. One can see that the gas-phase geometry is well maintained in water. The first solvation shell shows how the water molecules hydrogen bond with oxime-oxygen, axial uranyl oxygens, carboxylate oxygen, and U. Figure 5.3b shows radial distribution functions for some key distances: the uranyl-carbonate-oxygen ($U\text{-}O_c$) is predominately at 2.25 Å, the uranyl-oxime-oxygen ($U\text{-}O_{ox}$), at 2.30 Å, and the uranyl-oxime-nitrogen ($U\text{-}N_{ox}$) at 3.38 Å.

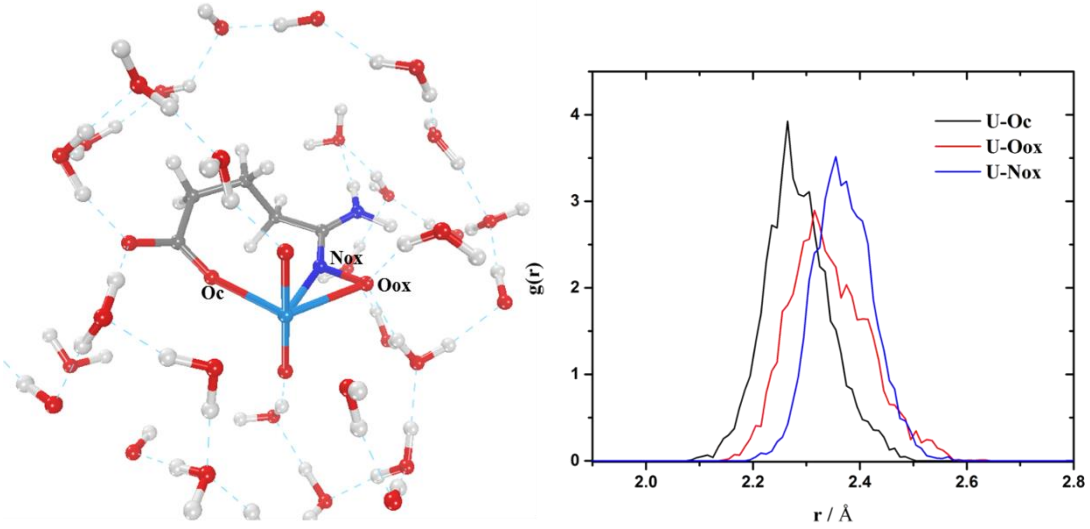

Figure 5.3. a) is the final snapshot of the interacting single bifunctional ligand contain AO-/Ac functional groups. b) Is the last 20 ps of the simulation. Bond distances are averages represented in units of Å. The blue dashed-lines represent hydrogen bond network

5.4.4 Binding of uranyl two bifunctional ligands in the gas phase.

Next, we continue our study by adding one more bifunctional ligand, since the equatorial coordination number of uranyl can reach six. Figure 5.4 shows the different types of binding configurations for two C2- ligands with one uranyl and their relative energies in the gas phase at the DFT-PBE level. Interestingly, one can see that the four most stable configurations of $[UO_2C_2]^{2-}$ all have very similar energies (within 0.10 eV). To test stability of these configurations in seawater, we performed CMD simulations, since it would be computationally prohibitive to simulate solvation of the complex in a 0.5 M NaCl solution with AIMD.

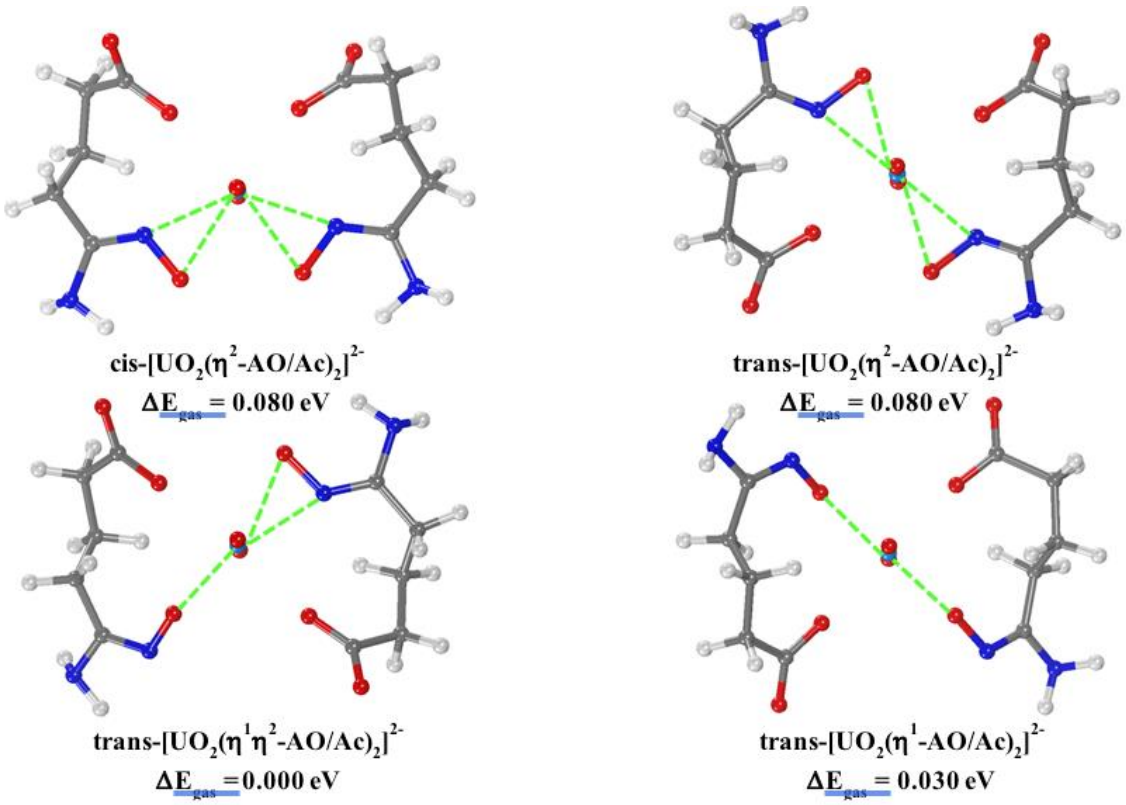

Figure 5.4. DFT-optimized gas-phase structures for the different types of binding modes with dimer bifunctional ligand. The structures chemical formula and relative energies are provided below each structure.

5.4.5 Classical MD simulations of binding of uranyl with two bifunctional ligands in 0.5 M NaCl

Using CMD, we simulated the stability of the four configurations in Figure 5.4 in 0.5 M NaCl. We found that the cis configuration is stable and therefore a local minimum on the free-energy surface. More interestingly, we found that all the three trans configurations converged into the two-fold η^2-trans configuration (Figure 5.4b). Hence in 0.5 M NaCl, the $[UO_2C_2]^{2-}$ complex can exist in two states. To evaluate the relative stability, we used umbrella sampling to obtain the potential-of-mean-force and binding free energies for the two configurations.

5.4.6 Binding free energies of uranyl with the bifunctional ligands in 0.5 M NaCl

Figure 5.5 shows the PMFs for sequential formations of the UO_2C complex (from UO_2^{2+} and C^{2-}) and the $[UO_2C_2]^{2-}$ complex (from UO_2C and C^{2-}). To assess the relative neighboring interaction upon the association of $[UO_2C_2]^{2-}$ the reaction coordinate is modeled by the U-Ooxime. We choose this collective variable to compare to previous calculated free-energy values, and most of the interaction is going to come from the uranyl and oxime-oxygen. Formation of the UO_2C complex (black line) goes through a metastable state between 4 – 5 Å where it then overcomes a 10 kJ/mol barrier to enter its lowest stable minimum binding state. It can be observed that the metastable state dissipates by the formation of the cis- or trans-hydrid dimer. Specifically, the metastable state almost disappears from trans- to cis- formation, shown respectively by the red and blue lines in Figure 5.5. Additionally, another comparison can be observed between the binding uranyl-bifunctional and the uranyl-$(\text{bifunctional})_2$, as the dimers are seen to dissociate 0.5-1.0 Å

sooner than the uranyl-bifunctional. Both of these last two observations are possibly due to the Coulombic-repulsion between interacting dimer bifunctional-ligands, which is an illustration of the hydrophilic 1:1 bifunctional ligand.

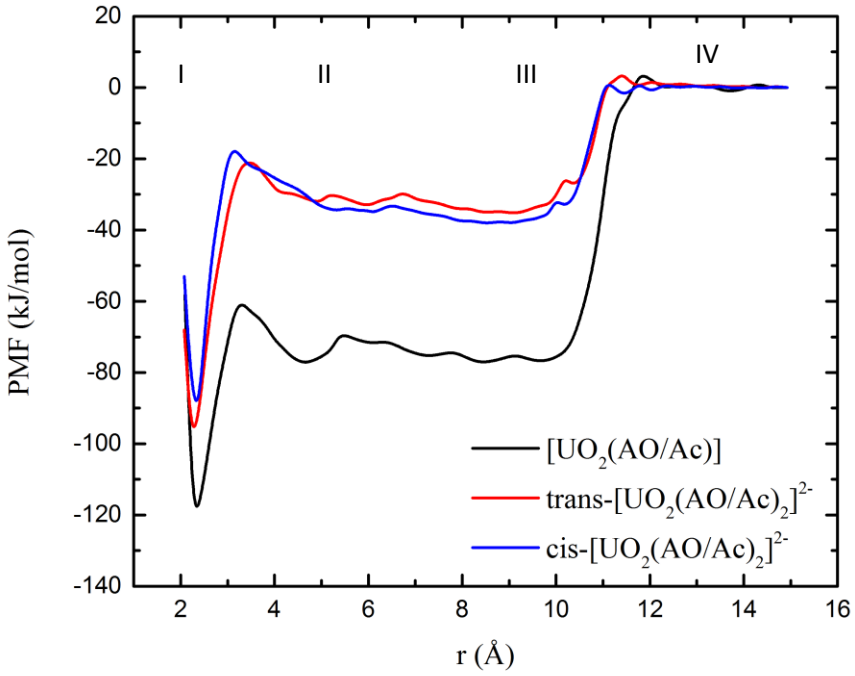

Figure 5.5. Is a cumulative free-energy plot containing the single uranyl-bifunctional, black line, and cis-\trans- uranyl-(bifunctional)$_2$, blue line and red line, respectively.

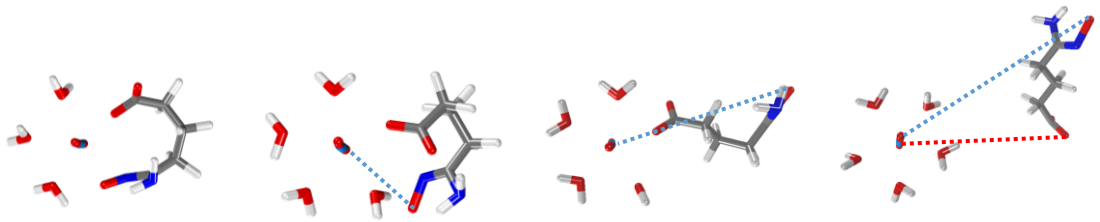

I II III IV

Figure 5.6. Shows key-points for the association of a single bifunctional ligand, [UO_2(C)] along the PMF curve in Figure 5.5. Red- and blue-dashed line represents the sequential binding to uranyl.

We can bring more light to the association by analyzing molecular interaction of uranyl-C from the inspection of key-regions in Figure 5, labeled as I, II, III, and IV. Figure 6 displays the different molecular configurations at each of these four relative points. In Figure 5.6, region IV, a single bifunctional-ligand begins its association approaching UO_2^{2+} hydration shell that is surrounded by 5-water molecules. In section III, the bifunctional-ligand's carboxylate (Ac) displaces a single water molecule from its first hydration shell as the Ac interacts in a monodentate fashion. As the oxime-oxygen move to the metastable state of interaction (region II), the oxime-amine is seen to displace a second water molecule from the uranyl hydration shell. As the formation continues into region I, a monodentate binding of the carboxylate and a distorted η^2 of the oxime group is seen.

To pry into the influence of neighboring ligands and its interaction with aqueous environment, the dimer formation of a bifunctional-ligand is analyzed. Figure 5.7 show key molecular structures interacting with the uranyl-bifunctional-ligand along the PMF for the second association dealing with the cis\trans- formation. In region IV and III, both forms exhibit very similar entrance into the ligand-hydration shell. As the carboxylate enters in region III of the ligand-hydration shell, a single water molecule is displaced, resulting in a mondentate interaction with the $[UO_2(C)]$ complex that is neighbored by two water molecules. However, inspecting the PMF (Figure 5.5), the association of the dimer, in general, shows shorter initial interaction distance (between 10.5 – 11.0 Å) as the second ligand enters the first ligand-hydration shell. This could be due to the interaction of the carboxylate of the entering ligand interacting with AO/Ac of the neighboring ligand, which could be explained by the flexibility from the free rotation of the Ac-group of the

coordinating Ac. Contrasting chemical behavior for the associating oxime-oxygen is observed for the cis- and trans- form in region II. The cis-$[UO_2(C)_2]^{2-}$ formation shows two relatively bulky neighboring AO^- functional groups interacting with sodium ions. The sodium ions are seen to facilitate the binding of the cis- form by mitigating Coulombic charge-charge interaction of neighboring like groups. Comparatively, the trans-$[UO_2(C)_2]^{2-}$ formation does not need much facilitation of the sodium ions and, instead, can bind to the uranium through the displacement of the final water molecule. The PMF shows a relatively more stable state for the trans- form in region II, which is likely due to the neighboring hydrogen-bonding with the first ligand-hydration shell. As the ligand continues along the reaction pathway it falls into a relatively stable cis\trans configuration (region I) with contrasting solvation interactions. In region I, both result in η2-formaton. Both, exhibit neighboring sodium ions surrounded by 6 oxygen molecules from water and the carboxylate groups. Interesting, the two interacting carboxylate groups in cis-$[UO_2(C)_2]^{2-}$, a hydrated sodium ion is seen to interact with the both carboxyl groups in a bidentate fashion, which increases interacting hydrating water molecules, while the trans configuration show less hydration with interacting AO/AO. This is consistent with previous conclusions that the carboxyl groups increase hydrophilicity of the ligands.

Some key chemical points can be made about the difference between the single and dimer formation with uranyl. The intrinsic chemical nature of the system's overall charge influences the dimer formation. As an example, the cis-$[UO_2(C)_2]^{2-}$ formation experiences a sodium ion to facilitate interacting uranyl and oxime group before the complete dimer formation, follow by the increase hydration of carboxylate groups with interacting sodium

ions. This suggests that anionic complexes influence metal-ion (sodium-ligand) interaction with the entire system. One can imagine that the increase in the localization of sodium ions can influence oxime-uranyl and ligand-ligand interaction by the increase of hydrated metal ions. A telltale sign of the possible Coulombic influence is that the dimer form overall is slower to interact, compared to the readiness of the single-bifunctional formation, seen in **Figure 5.5**. We can see the association of a single bifunctional-ligand is initiated around 12 Å, as opposed to the dimer at 10.5 – 11.0 Å. If we compare the $[UO_2(B)_2]^{2-}$ from literature, a pure oligomer containing the open-ligand shows to have less influence of the association distance between the single and dimer form. This suggests the incorporation of carboxylate illustrates more influences on the free-energy of binding by interaction of neighboring Ac-Ac.

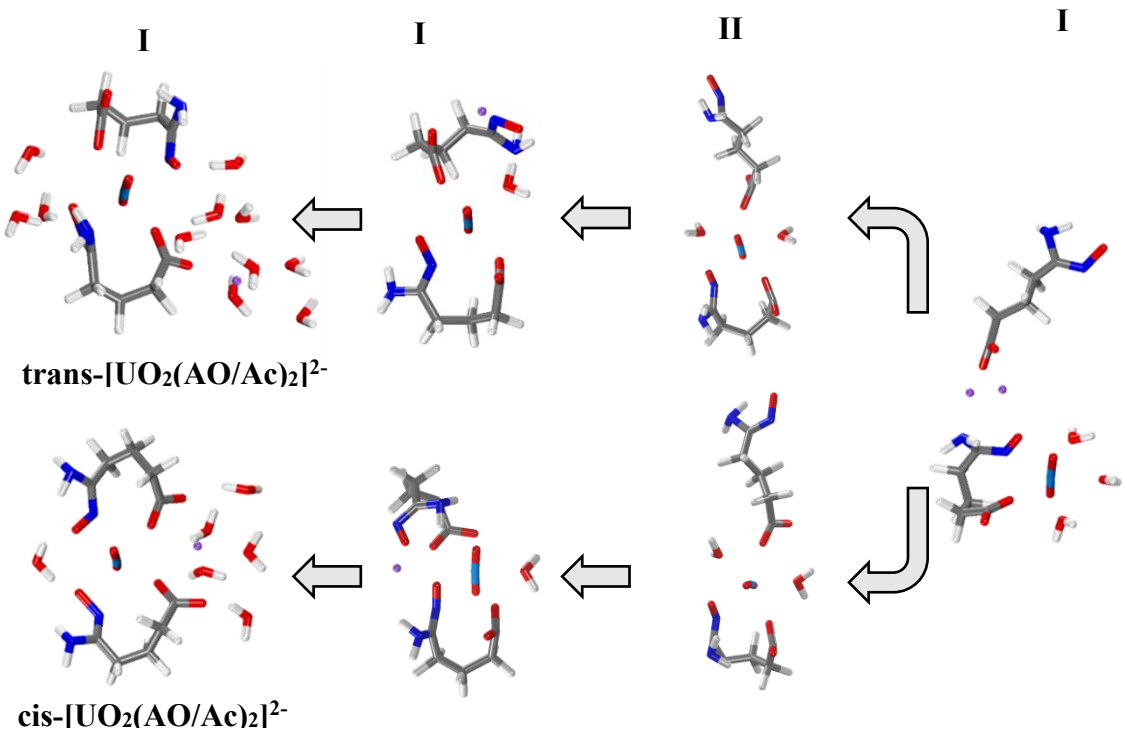

Figure 5.7. Are key molecular structures for the cis\trans-dimer formation along the PMF in Figure 5.5.

Table 5.1 compares the sequential ligand-interaction by the consecutive addition of the uranyl-AO/AO and uranyl-AO/Ac. The comparison of the first titration shows the 1:1, AO/Ac ligand, to be relatively more stable than AO/AO by -9.1 kJ/mol. Interesting, relative greater stability arises from the second titration with the formation of UO_2-$(AO/Ac)_2$ compared to UO_2-$(AO/AO)_2$. The alacrity for the thermochemical formation of UO_2-$(AO/Ac)_2$ is -28.2 kJ/mol more favorable than UO_2-$(AO/AO)_2$. Inspecting the cis-\trans-form shows trans to be slightly more thermochemically favorable by If we sum the sequential of each ligand added we see that the UO2-bifunctional interaction is thermodynamically more favorable by -52.8 kJ/mol compared to UO_2-AO/AO interaction.

Table 5.1. Binding free-energy comparison of the sequential binding for the bifunctional and nonbifunctional-ligand.

Binding Free-energy	**AO^-/AO^- (kJ/mol)**	**AO^-/Ac^- (kJ/mol)**
ΔG_1	**-91.9**	**-115.50**
ΔG_2	**-55.3**	**-86.9/-80.0**
$\Delta G_{total} = \Delta G_1 + \Delta G_2$	**-147.2**	**-200.0**

5.5 Conclusion

Further insight into the interaction of a bifunctional ligand, AO/Ac, with uranyl was studied from a combination of different MD methods and quantum gas-phase calculations. From the quantum gas-phase perspective, the introduction of the first ligand to uranyl illustrates an impartial selectivity of complexation towards the side-chains UO_2-(η^2-AO/Ac) and the bidentate UO_2-(Ac/AO), but relatively less selective to UO_2-(κ^2-AO/Ac). Furthermore, the gas-phase analysis on the subsequent addition of a bifunctional ligand shows no stark relative energetics, which implies the second dimer uniquely stabilizes the cis- and trans-η^2- form with uranyl. Thermodynamic assisted calculations provided a subtle free-energy difference between cis- and trans-, favoring trans by -6.9 kJ/mol. This slight difference is probably due to the coulombic repulsion between neighboring Ac^- groups. Additionally, when comparing the single binding uranyl-bifunctional to uranyl-bifunctional-dimer, a 0.5 – 1.0 Å dissociation difference is experienced. This finding suggests there does exist coulombic repulsive character between neighboring bifunctional ligands, which not apparent in the pure AO/AO case. Moreover, total binding free-energies for the sequential addition of the bifunctional ligands were studied and compared to that of the, formerly calculated, open-amidoxime ligands which showed a greater stability with a 1:1 AO/Ac, compared to AO/AO. Specifically, the total free-energy for the formation of the bifunctional-dimer to uranyl calculates to be -52.8 kJ/mol more than AO/AO base dimers. This work suggests that not only does there exist the possible synergetic effect between the covalent nature of 6d/5f character previously studied but also some coulombic contribution between neighboring ligands containing carboxylate groups. We plan on enhancing this

study a model of a more realistic system with uranyl-oligomer interaction with the oligomer consisting of different concentrations and arrangements of open-amidoximes, closed-amidoximes, and carboxylates.

This work illustrates implications toward the engineering and design of amidoxime/carboxylate type adsorbents by exploiting the hydrophilic chemical nature of bifunctional-based ligands. From the series of computational calculations from the sequential addition of AO/Ac based ligands in gas-phase show a unique characteristic of stabilizing the uranyl bifunctional binding by formation of a dimer bifunctional. Furthermore, this work pry's into the chemical behavior of neighboring bifunctional ligands that is beneficial for polymer development.

5.6 References

1. Kim, J.; Tsouris, C.; Mayes, R. T.; Oyola, Y.; Saito, T.; Janke, C. J.; Dai, S.; Schneider, E.; Sachde, D. Recovery of Uranium from Seawater: A Review of Current Status and Future Research Needs. Sep. Sci. Technol., 2013, 48 (3), 367-387 DOI: Doi 10.1080/01496395.2012.712599.

2. Davies, R. V.; Kennedy, J.; Hill, K. M.; Mcilroy, R. W.; Spence, R. Extraction of Uranium from Sea Water. Nature 1964, 203 (495), 1110-& DOI: Doi 10.1038/2031110a0.

3. Endrizzi, F.; Rao, L. F. Chemical Speciation of Uranium(VI) in Marine Environments: Complexation of Calcium and Magnesium Ions with [(UO2)(CO3)3] and the Effect on the Extraction of Uranium from Seawater. Chem. Euro. J. 2014, 14499-14506.

4. Bernhard, G.; Geipel, G.; Brendler, V.; Nitsche, H. Speciation of uranium in seepage waters of a mine tailing pile studied by time-resolved laser-induced fluorescence spectroscopy (TRLFS). Radiochim. Acta., 1996, 74, 87-91.

5. Bernhard, G.; Geipel, G.; Reich, T.; Brendler, V.; Amayri, S.; Nitsche, H. Uranyl(VI) carbonate complex formation: Validation of the Ca2UO2(CO3)(3)(aq.) species. Radiochim. Acta., 2001, 89 (8), 511-518 DOI: DOI 10.1524/ract.2001.89.8.511.

6. Abney, C. W.; Mayes, R. T.; Saito, T.; Dai, S. Materials for the Recovery of Uranium from Seawater. Chem. Rev., 2017, 117 (23), 13935-14013 DOI: 10.1021/acs.chemrev.7b00355.

7. Saito, T.; Brown, S.; Chatterjee, S.; Kim, J.; Tsouris, C.; Mayes, R. T.; Kuo, L. J.; Gill, G.; Oyola, Y.; Janke, C. J.; Dai, S. Uranium recovery from seawater: development of fiber adsorbents prepared via atom-transfer radical polymerization. J. Mater. Chem. A, 2014, 2 (35), 14674-14681 DOI: 10.1039/c4ta03276d.

8. Brown, S.; Yue, Y. F.; Kuo, L. J.; Mehio, N.; Li, M. J.; Gill, G.; Tsouris, C.; Mayes, R. T.; Saito, T.; Dai, S. Uranium Adsorbent Fibers Prepared by Atom-Transfer Radical Polymerization (ATRP) from Poly(vinyl chloride)-co-chlorinated Poly(vinyl chloride) (PVC-co-CPVC) Fiber. Ind. Eng. Chem. Res. 2016, 55 (15), 4139-4148 DOI: 10.1021/acs.iecr.5b03355.

9. Das, S.; Oyola, Y.; Mayes, R. T.; Janke, C. J.; Kuo, L. J.; Gill, G.; Wood, J. R.; Dai, S. Extracting Uranium from Seawater: Promising AF Series Adsorbents. Ind. Eng. Chem. Res. 2016, 55 (15), 4110-4117 DOI: 10.1021/acs.iecr.5b03136.

10. Liu, X. Y.; Liu, H. Z.; Ma, H. J.; Cao, C. Q.; Yu, M.; Wang, Z. Q.; Deng, B.; Wang, M.; Li, J. Y. Adsorption of the Uranyl Ions on an Amidoxime-Based Polyethylene Nonwoven Fabric Prepared by Preirradiation-Induced Emulsion Graft Polymerization. Ind. & Eng. Chem. Res., 2012, 51 (46), 15089-15095 DOI: 10.1021/ie301965g.

11. Oyola, Y.; Dai, S. High surface-area amidoxime-based polymer fibers co-grafted with various acid monomers yielding increased adsorption capacity for the extraction of uranium from seawater. Dalton Trans. 2016, 45 (21), 8824-8834 DOI: 10.1039/c6dt01114d.

12. Brown, S.; Chatterjee, S.; Li, M. J.; Yue, Y. F.; Tsouris, C.; Janke, C. J.; Saito, T.; Dai, S. Uranium Adsorbent Fibers Prepared by Atom-Transfer Radical Polymerization from Chlorinated Polypropylene and Polyethylene Trunk Fibers. Ind. Eng. Chem. Res., 2016, 55 (15), 4130-4138 DOI: 10.1021/acs.iecr.5b03667.

13. Wang, C. Z.; Lan, J. H.; Wu, Q. Y.; Luo, Q.; Zhao, Y. L.; Wang, X. K.; Chai, Z. F.; Shi, W. Q. Theoretical insights on the interaction of uranium with amidoxime and carboxyl groups. Inorg. Chem., 2014, 53 (18), 9466-76 DOI: 10.1021/ic500202g.

14. Guo, X. J.; Xiong, X. G.; Li, C.; Gong, H. F.; Huai, P.; Hu, J. T.; Jin, C.; Huang, L. L.; Wu, G. Z. DFT investigations of uranium complexation with amidoxime-, carboxyl- and mixed amidoxime/carboxyl-based host architectures for sequestering uranium from seawater. Inorg. Chim. Acta., 2016, 441, 117-125 DOI: 10.1016/j.ica.2015.11.013.

15. Zhang, B. W.; Guo, X. J.; Xie, S. Y.; Liu, X. Y.; Ling, C. J.; Ma, H. J.; Yu, M.; Li, J. Y. Synergistic nanofibrous adsorbent for uranium extraction from seawater. Rsc. Adv., 2016, 6 (85), 81995-82005 DOI: 10.1039/c6ra18785d.

16. Priest, C.; Li, B.; Jiang, D. E. Uranyl-Glutardiamidoxime Binding from First-Principles Molecular Dynamics, Classical Molecular Dynamics, and Free-Energy Simulations. Inorg Chem 2017, 56 (16), 9497-9504 DOI: 10.1021/acs.inorgchem.7b00711.

17. Kresse, G.; Hafner, J. Ab initio molecular dynamics for liquid metals. Phys. Rev. B, 1993, 47 (1), 558.

18. Kresse, G.; Furthmüller, J. Efficiency of ab-initio total energy calculations for metals and semiconductors using a plane-wave basis set. Comp. Mate.r Sci. 1996, 6 (1), 15-50.

19. Blöchl, P. E. Projector augmented-wave method. Phys. Rev. B, 1994, 50 (24), 17953.

20. Kresse, G.; Joubert, D. From ultrasoft pseudopotentials to the projector augmented-wave method. Phys. Rev. B, 1999, 59 (3), 1758.

21. Perdew, J. P.; Burke, K.; Wang, Y. Generalized gradient approximation for the exchange-correlation hole of a many-electron system. Phys. Rev. B, 1996, 54 (23), 16533.

22. Joung, I. S.; Cheatham, T. E. Determination of alkali and halide monovalent ion parameters for use in explicitly solvated biomolecular simulations. J. Phys. Chem. B, 2008, 112 (30), 9020-9041 DOI: 10.1021/jp8001614.

23. Wang, J. M.; Wolf, R. M.; Caldwell, J. W.; Kollman, P. A.; Case, D. A. Development and testing of a general amber force field (vol 25, pg 1157, 2004). J. Comput. Chem. 2005, 26 (1), 114-114 DOI: 10.1002/jcc.20145.

24. Frisch, M. J. Gaussian 09, Gaussian, Inc: Wallingford, CT, 2009.

25. Wang, J. M.; Wang, W.; Kollman, P. A.; Case, D. A. Automatic atom type and bond type perception in molecular mechanical calculations. J. Mol. Graph. Model. 2006, 25 (2), 247-260 DOI: 10.1016/j.jmgm.2005.12.005.

26. Guilbaud, P.; Wipff, G. MD simulations on UO2 (2+) and Sr2+ complexes with CMPO derivatives in aqueous solution and at a water/chloroform interface. N. J. Chem. 1996, 20 (6), 631-642.

27. Buhl, M.; Wipff, G. Insights into Uranyl Chemistry from Molecular Dynamics Simulations. Chemphyschem. 2011, 12 (17), 3095-3105 DOI: 10.1002/cphc.201100458.

28. D.A. Case, V. B., J.T. Berryman, R.M. Betz, Q. Cai, D.S. Cerutti, T.E. Cheatham, III, T.A. Darden, R.E.; Duke, H. G., A.W. Goetz, S. Gusarov, N. Homeyer, P. Janowski, J. Kaus, I. Kolossváry, A. Kovalenko,; T.S. Lee, S. L., T. Luchko, R. Luo, B. Madej, K.M. Merz, F. Paesani, D.R. Roe, A. Roitberg, C. Sagui,; R. Salomon-Ferrer, G. S., C.L. Simmerling, W. Smith, J. Swails, R.C. Walker, J. Wang, R.M. Wolf, X.; Kollman, W. a. P. A. AMBER 14, University of California, San Francisco, 2014.

29. Kumar, S.; Bouzida, D.; Swendsen, R. H.; Kollman, P. A.; Rosenberg, J. M. The Weighted Histogram Analysis Method for Free-Energy Calculations on Biomolecules .1. The Method. J. Comput. Chem. 1992, 13 (8), 1011-1021 DOI: DOI 10.1002/jcc.540130812.

30. Chialvo, A. A.; Cummings, P. T.; Cochran, H. D.; Simonson, J. M.; Mesmer, R. E. Na+-Cl- Ion-Pair Association in Supercritical Water. J. Chem. Phys., 1995, 103 (21), 9379-9387 DOI: Doi 10.1063/1.470707.

31. Doudou, S.; Arumugam, K.; Vaughan, D. J.; Livens, F. R.; Burton, N. A. Investigation of ligand exchange reactions in aqueous uranyl carbonate complexes using computational approaches. Phys. Chem. Chem. Phys. 2011, 13 (23), 11402-11411 DOI: 10.1039/c1cp20617f.

CHAPTER SIX

Solvation of the vanadate ion in seawater conditions from molecular simulations

6.1 Abstract

One of the current challenges present in uranium extraction from seawater is the competitive sorption of vanadium. But compared with uranium, much less is known about the solvation and speciation of the vanadate ion in seawater. Herein, we utilize both first principles molecular dynamics and classical molecular dynamics simulations to provide a microscopic insight into the solvation of the HVO^{2}_{4} ion in pure water and in seawater. In pure water, we found that the dianion state is the most probable structure. But in a simulated seawater with 0.55 M NaCl, the $NaHVO_4$ ion is most probable, followed by the neutral Na_2HVO_4; averaging over 100-ns trajectory, the coordination number of Na^+ ions around V was found to be 1.5 within a radius of 4.0 Å. We found that the $NaHVO_4$ ion can exist in two interchangeable states: a bidentate state where the Na^+ ion interacts directly with two vanadate oxo groups; a monodentate where the Na^+ ion interacts with only one vanadate oxo group. From this monodentate state, the Na^+ ion can further dissociate away with a free-energy barrier of 2.5 kcal/mol. Our work therefore demonstrates that Na^+ ions are closely associated with the vanadate species in seawater.

6.2 Introduction

When terrestrial nuclear resources become scarce and expensive due to increasing demand from more nuclear reactors, uranium recovery from seawater is needed. An estimated 4.5 billion metric tons of uranium in seawater theorizes an auspicious source of nuclear energy for many millennia [1, 2]. Experimental screening methods have shown that the most promising method for uranium extraction from seawater entails an amidoxime-grafted polymer [3, 4]. These poly(amidoxime) adsorbent material can be prepared with methods such as radiation-induced graft polymerization [5] and atom-transfer radical polymerization [6, 7]. Although promising, these poly(amidoxime) sorbents attract more vanadium (V) than uranium from sweater [8, 9]. Hence, one prevalent challenge of developing advanced sorbents for uranium from seawater is to enhance U/V selectivity while increasing the U uptake at the same time.

Vanadium exists in seawater at 1.7-2.3 ppb [10] with a predominate oxidation state of 5+ as a vanadate anion, [11] while uranium is found at 3.3 ppb as a uranyl ion [1]. The speciation of vanadate (V) in solution can involve complex equilibria between various mono- and oligonuclear clusters, critically depending on concentration and pH [12]. In seawater pH of 8.2, V(V) is present in equilibrium with two oxyanion forms of the orthovanadate, $H_2VO_4^-$ and HVO_4^{2-}. Although a number of recent studies have shed important light on speciation of uranyl in different aqueous environments,[13-16] [17] little is known about speciation of vanadium species in seawater [12, 18-21]. Equilibrium complexation of HVO_4^{2-} has been previously determined from speciation calculations using free ion concentrations modeled for seawater and calculated stability contestants at the appropriate ionic strength [20].

From the perspective of molecular simulations, Buhl et al. have investigated water effects on the ^{51}V NMR chemical shifts of $H_2VO_4^-$ with Car-Parrinello molecular dynamics (CPMD) [22]. They found that the aqueous environment induced a conformational change on the two VOH moieties from C_2 symmetry to C_s symmetry and an exchange of water molecules between the first solvation sphere of $H_2VO_4^-$ and the solution. Recent work with coupled cluster theory examined coordination number and prominent binding modes of water and other ligands to vanadyl (VO_2^+) [19]. From a single-crystal structure, Rao and coworkers have found a unique binding mode of vanadium to amidoxime-type ligand, where the V-O bonds are sequentially displaced by two amidoximate oxygens [23]. In addition, the oxovanadium (IV) and dioxovanadium (V) complexation with an amidoximate ligand has been studied computationally [18, 19].

To our knowledge, the solvation of the HVO_4^{2-} ion, a major species of V(V) in seawater, has not been studied from a computational perspective, especially under the realistic solvation conditions. In this paper, our goal is to understand solvation of the HVO_4^{2-} ion in seawater from molecular dynamics simulations. We use both density functional theory molecular dynamics (DFT-MD) and classical molecular dynamics (CMD) simulations. Starting with Na_2HVO_4, we first pry into dissociation of sodium ions. Next, we investigate how Na^+ ions interact with the vanadate ion. Furthermore, we calculate the potential of mean force of dissociating Na^+ from vanadate.

6.3 Computational methods

6.3.1 Quantum Mechanical Calculations

First-principles molecular dynamic simulations based on density functional theory (DFT-MD) and Born–Oppenheimer approximation were carried out using Vienna Ab-initio simulation package (VASP) with plane wave basis and periodic boundary conditions [24, 25]. The Kohn-Sham equations are solved with the all-electron projected augmented wave (PAW) method [26, 27]. We have chosen the Perdew-Burke-Ernzerhof (PBE) functional of the generalized-gradient approximation (GGA) for electron exchange and correlation [28]. PBE is one of the most versatile GGA functionals, which provides a balance description for diverse molecules and materials, instead of being designed for a special class of molecules or interactions. The MD calculations were carried out at 298 K in a canonical NVT ensemble for a periodic cubic box that contains one Na_2HVO_4 complex in a fixed number of water molecules: we examined two concentrations with 50 and 100 water molecules. The temperature was kept constant via Nose-Hoover thermostat. A Verlet algorithm was used to integrate Newton's equation of motion with a time step of 1 femtosecond. After equilibration at 298 K for 15 ps, another 15 ps of production run was followed. Graphical visualization and analysis of the liquid structure packing of the vanadate complex was examined with VMD [29].

6.3.2 Force field parameters

Generalized Amber force field (GAFF) format was used for the HVO_4^{2-} anion based on Gaussian09 calculations at the B3LYP level of theory with the 6-31G(d) basis sets for O and H and the LANL2DZ effective-core potential for V. Restrained electrostatic

potential (RESP) charges were obtained from fitting into the electrostatic potential from Gaussian09 calculations. The van der Waals parameter for V was taken from the UFF while those for O and H from AMBER [30]. Bond stretching, bond bending, and dihedral angle parameters were from fitting the potential energy curves from Gaussian09 scanning. All the force field parameters were provided in the supplementary materials (Figure S6.1-S6.2; Table S6.1-S6.4). To validate these parameters, gas-phase bond lengths and angles of HVO_4^{2-} optimized with Gaussian09 at the B3LYP level and with AMBER using the determined force field parameters were compared in Table S6.5 of the supplementary materials. One can see an overall excellent agreement.

6.3.3 Classical MD

To investigate Na_2HVO_4 in water, both fresh and seawater were used: the fresh water model contains 1500 water molecules, while the seawater model contains additional 15 Na^+ and Cl^- ions, to mimic the salinity of seawater at 0.54 M NaCl. The TIP3P model was used for water, while the vdW parameters for Na^+ and Cl^- ions are the same as used previously [31]. Before an unconstrained production run, a sequence of constrained steps was employed to keep the sodium's localized around the vanadate complex: first, a simple minimization step with 2000 optimization steps; second, a NVT heating run from 0 K to 300 K for 100 ps with a 1fs time; next, a 10 ns NPT equilibration step for optimal volume and density. After an equilibration run, a 100 ns unconstrained production run was performed. For the production run, the temperature was kept constant using the Nose-Hover thermostat at 300 K, and the geometry of the water molecules was held fix with the SHAKE algorithm.

6.3.4 Umbrella sampling

The potential of mean force (PMF) simulation via umbrella sampling was performed to obtain the free-energy profile of $NaHVO_4^-$ dissociation into HVO_4^{2-} and Na^+. A bias potential of 40 kcal/mol along the reaction coordinate (the Na-V distance, r_{Na-V}) drove the system from an initial $NaHVO_4^-$ thermodynamic state to a final HVO_4^{2-} (product). Starting at r_{Na-V}=3.0 Å the system took intermediate steps of 0.1 Å that was covered by a series of windows performed at 10 ns time frame to a final 6.0 Å. All windows were then stitched together with the Weighted Histogram Analysis Method (WHAM) to generate the PMF.

6.4 Results and discussion

6.4.1 DFT-MD analysis of Na_2HVO_4 in water

To investigate the most stable vanadate structure, we simulated the interaction of vanadate in water with DFT-MD using the Na_2HVO_4 salt as the initial state. Figure 6.1 shows a molecular model of Na_2HVO_4: a tetrahedral structure that is charge balanced with two sodium ions within close proximity of vanadate's oxygens. Two types of vanadate oxygens exist: a protonated V-OH group and three unprotonated V-O groups. To study the solvation of sodium ions, we monitored the interaction of sodium ions to vanadium. In the 50-ps DFT-MD simulation, the dissolution of one sodium ion was observed. In the case of a simulation cell of 50 water molecules, the dissociating sodium departure is at about 6 ps (Figure 6.2a), while in the case of 100 water molecules, the dissociation of the sodium is around 8 ps (Figure 6.2b). One can also see that during the 50-ps time frame, one sodium ion remains associated with the vanadate anion as $NaHVO_4^-$. Limited by the accessible

timescale of our DFT-MD simulation, we could not examine the dissolution of the remaining sodium ion from the brute-force DFT-MD simulation. So we turn to classical MD which allows us to simulate Na_2HVO_4 in both pure water and seawater for a much longer time scale.

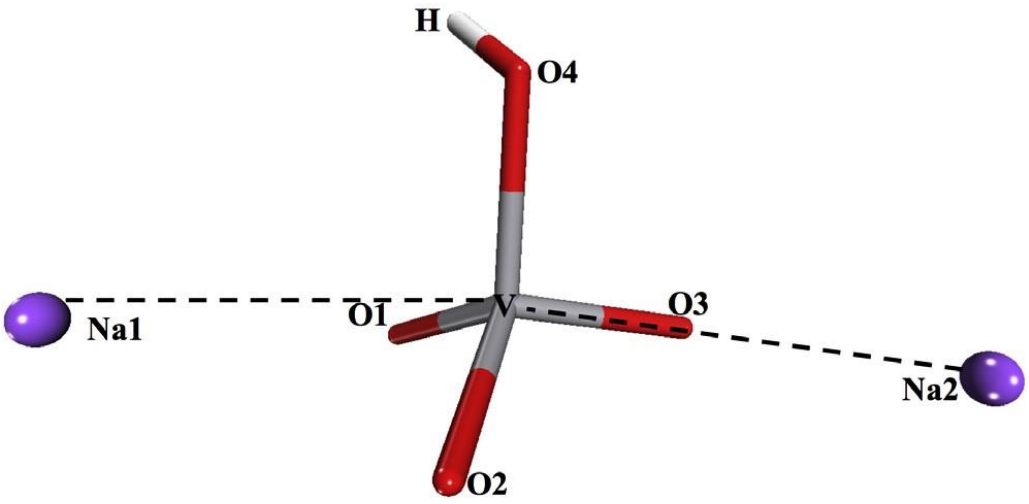

Figure 6.1 Structure of Na_2HVO_4 used as the initial state in the simulation.

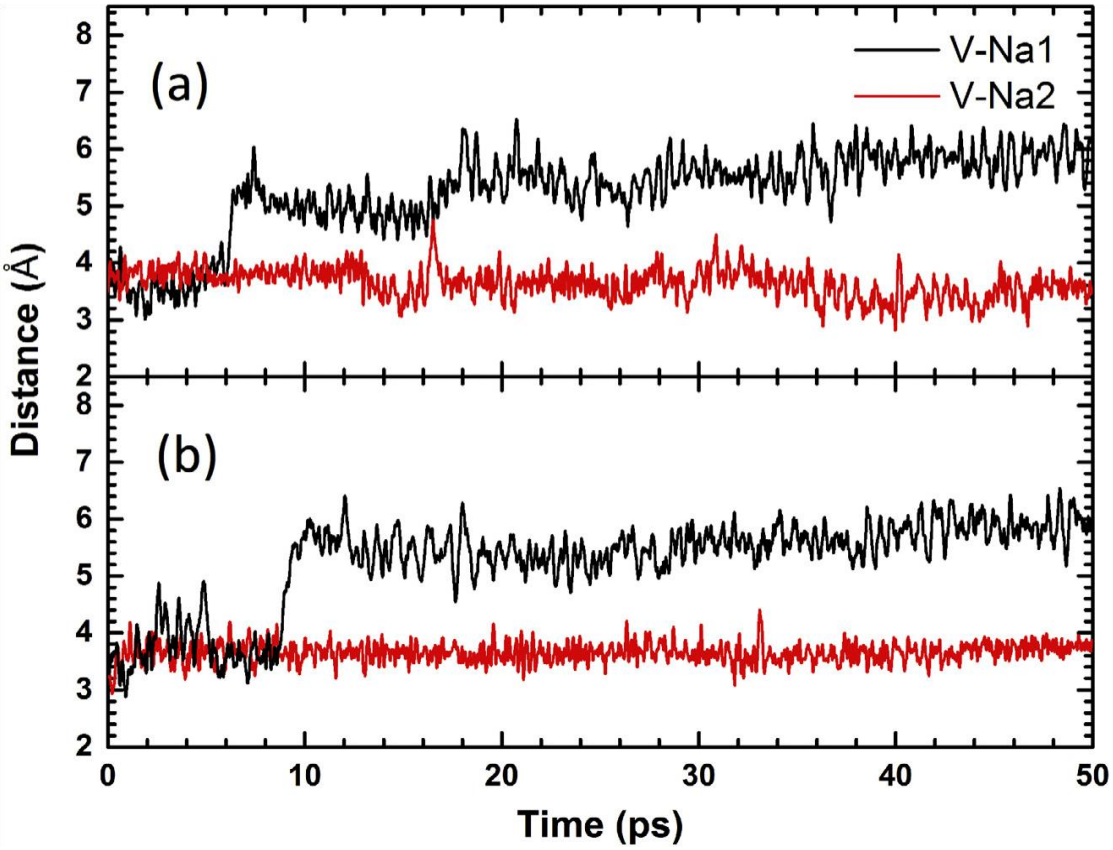

Figure 6.2 V-Na1 and V-Na2 distances as a function of time, starting with Na_2HVO_4 (Fig. 6.1) in water, from DFT-MD: (a) in a simulation cell of 50 water molecules; (b) in a simulation cell of 100 water molecules.

6.4.2 Classical molecular dynamics of Na_2HVO_4 in pure water and seawater

To further follow the dissolution of the two sodium ions, we first explore the coordination number (CN) of sodium ions around the vanadate in a 100-ns time frame. In pure water (Figure. 6.3a), we found that both sodium ions can dissociate away and spend most of their time away from the HVO_4^{2-} anion (CN=0), while one sodium ion often associates with the HVO_4^{2-} anion (CN=1) and occasionally two sodium ions associate with the HVO_4^{2-} anion at the same time (CN=2). In seawater conditions (Figure. 6.3b), we found that both sodium ions can dissociate away from the HVO_4^{2-} anion (CN=0), but the most probable CN is between 1 and 2; sometimes there are three and even four sodium ions around the HVO_4^{2-} anion.

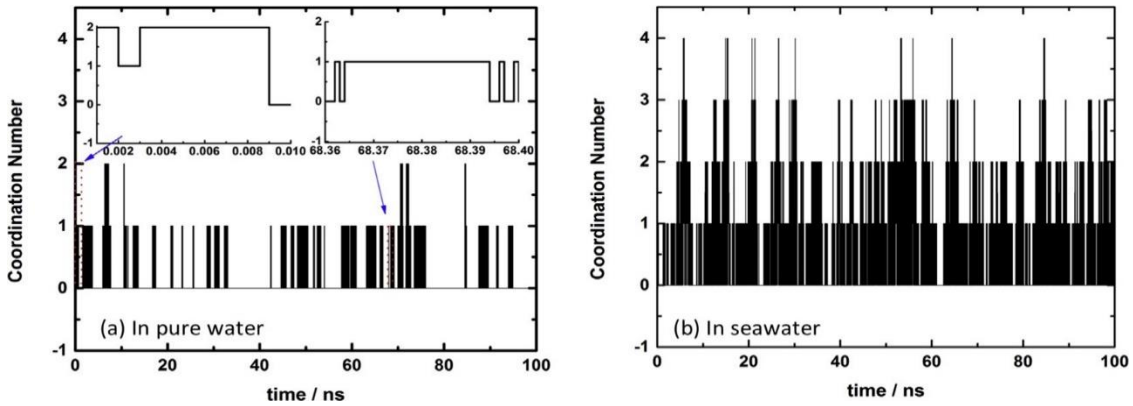

Figure 6.3 Change of coordination number of Na^+ ions around V with time from 100-ns classical molecular dynamics simulations: (a) in pure water; (b) in seawater.

Averaging over the 100-ns trajectories in Figure 6.3, we obtained the radial distribution function (RDF) of sodium ions around V (Figure 6.4). In both pure water and seawater, two peaks can be seen at 2.95 Å and 3.55 Å. These peaks represent two interacting sites around the vanadate complex. As shown in Fig. 6.5, the 2.95-Å site corresponds to a state where Na^+ interacting with two oxo groups (Na-O_V distances at 2.42 and 2.54 Å), while the 3.55-Å site corresponds to a state where Na^+ interacting with one oxo group (Na-O_V distance at 2.30 Å). Furthermore, CN from the integrated RDF shows that there is 0.3 Na^+ within a 4.0-Å radius around V in pure water, while there are 1.5 Na^+ around V in seawater.

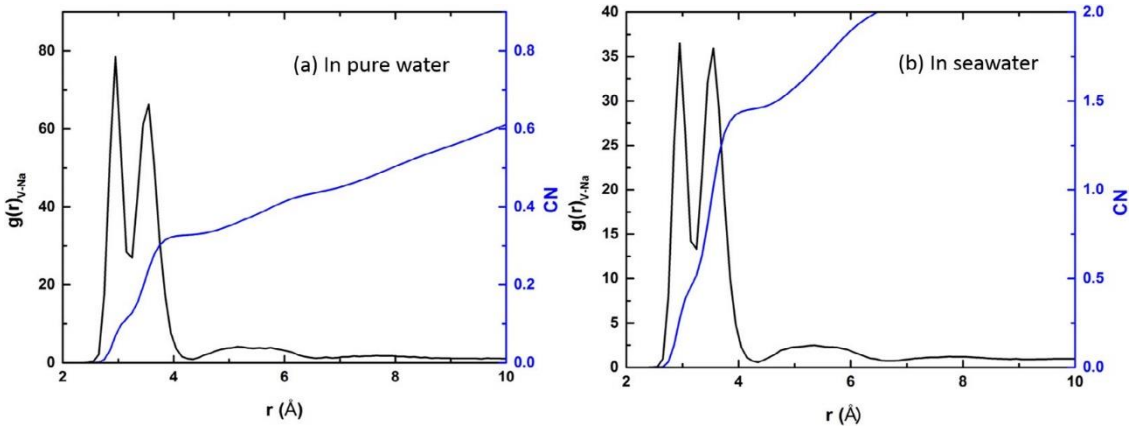

Figure 6.4 Radial distribution function (black) and coordination number (blue) of Na^+ ions around V averaged over 100-ns trajectories of classical molecular dynamics simulations: (a) in pure water; (b) in seawater.

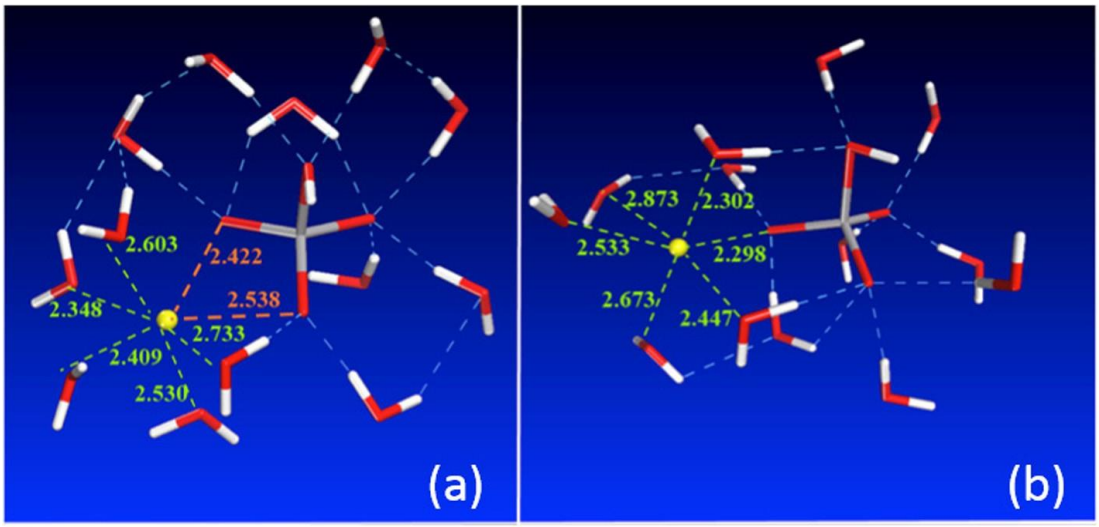

Figure 6.5 Snapshots of two states of $NaHVO_4^-$ in pure water, corresponding to the two peaks in radial distribution function of Na around V in Fig. 6.4a: (a) rV-Na = 2.95 Å; (b) rV-Na = 3.55Å. Na, yellow; V, gray; O, red; H, white.

6.4.3 Salt effect on hydrogen bonding

The CN of sodium ions around the vanadate anion is closely related to the hydrogen-bond network. So we explored the hydrogen bond lifetime of the vanadate anion in pure water and in seawater. To define the hydrogen bonds between water and the vanadate, we used geometrical criteria of the O-H---O distance within 3.0 Å and angles greater than 135^{o}. From Figure 6.6, one can see that a longer lifetime of hydrogen bonds around the vanadate anion is observed in pure water than in seawater. So the existence of a high concentration of NaCl disrupts the hydrogen-bond network around the vanadate anion, thereby accelerating the hydrogen-bond dynamics. This is consistent with our finding that 1.5 sodium ions are closely associated with the vanadate anion as shown in the RDF plot (Figure 6.4b).

The effects of adding NaCl on the solvation of the vanadate can be further inspected from the number of hydrogen bonds around each V-O group. Table 6.1 shows the average number of hydrogen bonds over the 100-ns trajectory. In pure water, the oxo groups (O1, O2, and O3) of vanadate (Figure. 6.1) are calculated to accept about three hydrogens from surrounding waters, whereas the –OH group (O4) of vanadate accepts two. In seawater, the average number of hydrogen bonds decreases by about 0.3 to 0.4, as the sodium ions now compete with water molecules for the interaction with the vanadate anion.

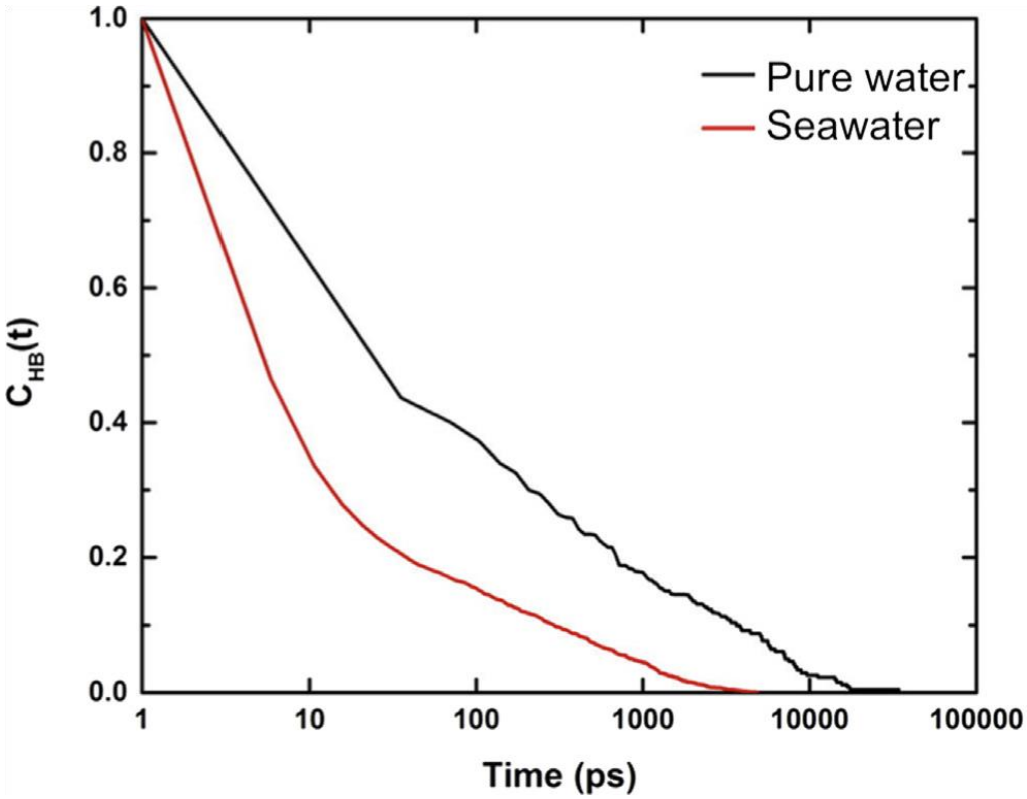

Figure 6.6 Hydrogen bond autocorrelation function, CHB(t), for water molecules hydrogen-bonded to HVO_4^{2-} in pure water (black) and in seawater (red).

Table 6.1: Average number of hydrogen bonds with the V-O groups of vanadate over 100-ns trajectory

V-O	In pure water	In seawater
V-O1	3.03	2.74
V-O2	3.06	2.77
V-O3	3.08	2.83
V-O4	2.24	1.86

6.4.4 Free-energy dissociation of $NaHVO_4$

The DFT-MD and CMD simulations above show the high probability of the vanadate anion with a sodium ion associated with it to form $NaHVO_4^-$. To examine the free-energy profile for this sodium ion to dissociate away from the vanadate, we used umbrella sampling with our CMD simulations to obtain the potential of mean force (PMF). Figure 6.7 shows the free-energy profile of $NaHVO_4^-$ dissociation to HVO_4^{2-} and Na^+ in pure water and in seawater. One can see that the sodium ion in $NaHVO_4^-$ exists in two states, one with V-Na distance of 2.95 Å and the other with V-Na distance of 3.5 Å, as already shown in the RDF plot in Figure 6.4 and in the snapshots in Figure 6.5. The two states are separated by a small barrier of ~0.7 kcal/mol. From the 3.5-Å state, the sodium ion can then break away with a barrier of 2.2 kcal/mol in pure water and 2.5 kcal/mol in seawater; both barriers are small enough that we observed many crossings in our brute-force MD simulations at 300K (Figure 6.2). At the transition state (Figure 6.8a), the Na-O_V distance is at 2.63 Å and the Na^+ ion is surrounded by five water molecules. Figure 6.7 also shows that the associated state ($NaHVO_4^-$) is more stable than the dissociated state (HVO_4^{2-} and Na^+). In addition, this stability is enhanced in seawater than in pure water. In the dissociated state, the Na^+ ion is now surrounded by six water molecules (Figure 6.8b).

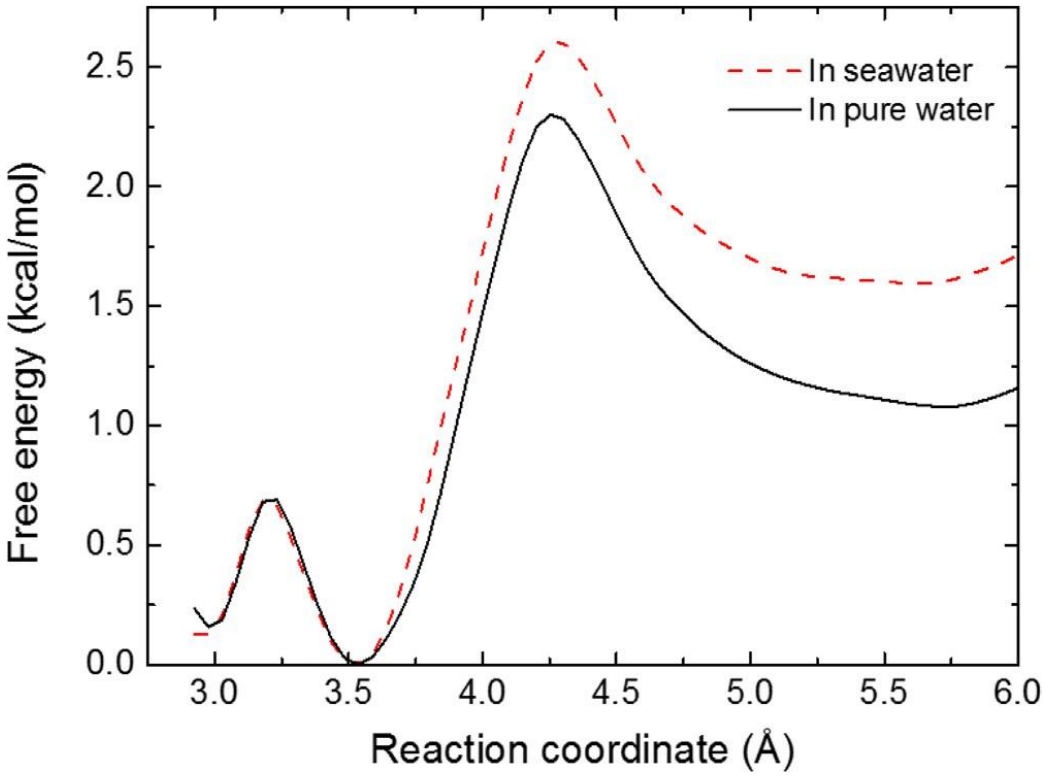

Figure 6.7 Free-energy profile from the potential of mean force of $NaHVO_4^-$ dissociation to HVO_4^{2-} and Na+ in pure water and in seawater. Reaction coordinate is defined as the V-Na distance.

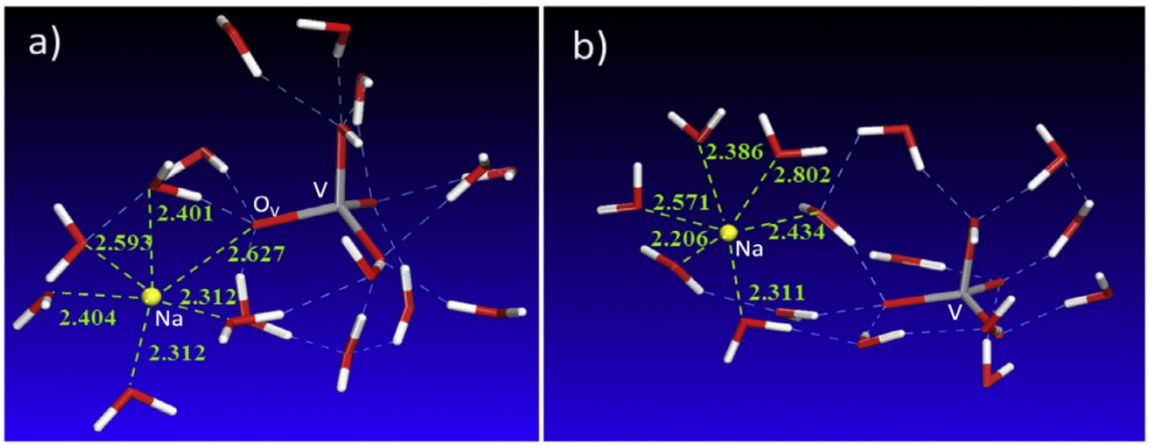

Figure 6.8 Snapshots along the potential of mean force (PMF) of $NaHVO_4^-$ dissociating into HVO_4^{2-} and Na^+: (a) transition state (at a Na-V distance of 4.25 Å in Fig. 6.7); (b) after dissociation (at a Na-V distance of 5.75 Å in Fig. 6.7). Na, yellow; V, gray; O, red; H, white.

6.5 Conclusions

In summary, we have examined the solvation of the vanadate anion (HVO_4^{2-}) with molecular dynamics simulations. Starting with Na_2HVO_4, DFT-MD showed that one Na^+ ion quickly dissociates away within a few ps, while the second Na^+ ion remains associated within the timescale of 50 ps. Classical MD simulations on the time scale of 100 ns showed that the fully dissociated state (HVO_4^{2-}) is most probable in pure water, while in seawater $NaHVO_4^-$ is the most probable state. Relaxation of hydrogen bonds around the vanadate anion was found to be faster in seawater than in pure water due to the disruption of the hydrogen-bond network by the Na^+ ions. Potential of mean force for $NaHVO_4^-$ dissociation into HVO_4^{2-} and Na^+ ion revealed a smaller barrier of ~2.5 kcal/mol. Our simulations show the importance of Na^+ ions in the solvation and speciation of vanadate in seawater; this knowledge will be useful for further understanding of the uranium/vanadium selectivity in ligand binding and design for seawater uranium recovery.

6.6 References

1. Davies, R. V.; Kennedy, J.; Hill, K. M.; Mcilroy, R. W.; Spence, R. Extraction of Uranium from Sea Water. Nature 1964, 203 (495), 1110-& DOI: Doi 10.1038/2031110a0.

2. Kim, J.; Tsouris, C.; Mayes, R. T.; Oyola, Y.; Saito, T.; Janke, C. J.; Dai, S.; Schneider, E.; Sachde, D. Recovery of Uranium from Seawater: A Review of Current Status and Future Research Needs. Sep. Sci. Technol. 2013, 48 (3), 367-387 DOI: 10.1080/01496395.2012.712599.

3. Schenk, H. J.; Astheimer, L.; Witte, E. G.; Schwochau, K. Development of Sorbers for the Recovery of Uranium from Seawater .1. Assessment of Key Parameters and Screening Studies of Sorber Materials. Sep. Sci. Technol. 1982, 17 (11), 1293-1308 DOI: Doi 10.1080/01496398208056103.

4. Astheimer, L.; Schenk, H. J.; Witte, E. G.; Schwochau, K. Development of Sorbers for the Recovery of Uranium from Seawater .2. The Accumulation of Uranium from Seawater by Resins Containing Amidoxime and Imidoxime Functional-Groups. Sep. Sci. Technol. 1983, 18 (4), 307-339 DOI: Doi 10.1080/01496398308068568.

5. Okamoto, J.; Sugo, T.; Katakai, A.; Omichi, H. Amidoxime-Group-Containing Adsorbents for Metal-Ions Synthesized by Radiation-Induced Grafting. J Appl Polym Sci 1985, 30 (7), 2967-2977 DOI: DOI 10.1002/app.1985.070300720.

6. Brown, S.; Chatterjee, S.; Li, M. J.; Yue, Y. F.; Tsouris, C.; Janke, C. J.; Saito, T.; Dai, S. Uranium Adsorbent Fibers Prepared by Atom-Transfer Radical Polymerization from Chlorinated Polypropylene and Polyethylene Trunk Fibers. Ind. Eng. Chem. Res. 2016, 55 (15), 4130-4138 DOI: 10.1021/acs.iecr.5b03667.

7. Brown, S.; Yue, Y. F.; Kuo, L. J.; Mehio, N.; Li, M. J.; Gill, G.; Tsouris, C.; Mayes, R. T.; Saito, T.; Dai, S. Uranium Adsorbent Fibers Prepared by Atom-Transfer Radical Polymerization (ATRP) from Poly(vinyl chloride)-co-chlorinated Poly(vinyl chloride) (PVC-co-CPVC) Fiber. Ind. Eng. Chem. Res., 2016, 55 (15), 4139-4148 DOI: 10.1021/acs.iecr.5b03355.

8. Suzuki, T.; Saito, K.; Sugo, T.; Ogura, H.; Oguma, K. Fractional elution and determination of uranium and vanadium adsorbed on amidoxime fiber from seawater. Anal. Sci., 2000, 16 (4), 429-432 DOI: DOI 10.2116/analsci.16.429.

9. Das, S.; Oyola, Y.; Mayes, R. T.; Janke, C. J.; Kuo, L. J.; Gill, G.; Wood, J. R.; Dai, S. Extracting Uranium from Seawater: Promising AF Series Adsorbents. Ind. Eng. Chem. Res., 2016, 55 (15), 4110-4117 DOI: 10.1021/acs.iecr.5b03136.

10. Collier, R. W. Particulate and Dissolved Vanadium in the North Pacific-Ocean. Nature, 1984, 309 (5967), 441-444 DOI: Doi 10.1038/309441a0.

11. Abbasse, G.; Ouddane, B.; Fischer, J. C. Determination of trace levels of dissolved vanadium in seawater by use of synthetic complexing agents and inductively coupled plasma-atomic emission spectroscopy (ICP-AES). Anal. Bioanal. Chem., 2002, 374 (5), 873-878 DOI: 10.1007/s00216-002-1532-3.

12. Sadoc, A.; Messaoudi, S.; Furet, E.; Gautier, R.; Le Fur, E.; Le Polles, L.; Pivan, J. Y. Structure and stability of VO2+ in aqueous solution: A car-parrinello and static ab initio study. Inorg. Chem., 2007, 46 (12), 4835-4843 DOI: 10.1021/ic0614519.

13. Priest, C.; Tian, Z. Q.; Jiang, D. E. First-principles molecular dynamics simulation of the Ca2UO2(CO3)(3) complex in water. Dalton Trans., 2016, 45 (24), 9812-9819 DOI: 10.1039/c5dt04576b.

14. Bernhard, G.; Geipel, G.; Brendler, V.; Nitsche, H. Speciation of uranium in seepage waters of a mine tailing pile studied by time-resolved laser-induced fluorescence spectroscopy (TRLFS). Radiochim. Acta., 1996, 74, 87-91.

15. Bernhard, G.; Geipel, G.; Reich, T.; Brendler, V.; Amayri, S.; Nitsche, H. Uranyl(VI) carbonate complex formation: Validation of the Ca2UO2(CO3)(3)(aq.) species. Radiochim. Acta., 2001, 89 (8), 511-518 DOI: DOI 10.1524/ract.2001.89.8.511.

16. Tirler, A. O.; Hofer, T. S. The structural influence of Ca2+ counter-ions on uranyl(VI) tricarbonate in aqueous solution. Dalton Trans., 2016, 45 (12), 4983-4988 DOI: 10.1039/c5dt04718h.

17. Endrizzi, F.; Rao, L. F. Chemical Speciation of Uranium(VI) in Marine Environments: Complexation of Calcium and Magnesium Ions with [(UO2)(CO3)3] and the Effect on the Extraction of Uranium from Seawater. Chem. Euro. J. 2014, 14499-14506.

18. Mehio, N.; Ivanov, A. S.; Ladshaw, A. P.; Dai, S.; Bryantsev, V. S. Theoretical Study of Oxovanadium(IV) Complexation with Formamidoximate: Implications for the Design of Uranyl-Selective Adsorbents. Ind. Eng. Chem. Res., 2016, 55 (15), 4231-4240 DOI: 10.1021/acs.iecr.5b03398.

19. Mehio, N.; Johnson, J. C.; Dai, S.; Bryantsev, V. S. Theoretical study of the coordination behavior of formate and formamidoximate with dioxovanadium(v) cation: implications for selectivity towards uranyl. Phys Chem Chem Phys 2015, 17 (47), 31715-31726 DOI: 10.1039/c5cp06165b.

20. Turner, D. R.; Whitfield, M.; Dickson, A. G. The Equilibrium Speciation of Dissolved Components in Fresh-Water and Seawater at 25-Degrees-C and 1 Atm Pressure. Geochim. Cosmochim. Ac. 1981, 45 (6), 855-881 DOI: Doi 10.1016/0016-7037(81)90115-0.

21. Wu, F.; Qin, T.; Li, X. F.; Liu, Y.; Huang, J. H.; Wu, Z. Q.; Huang, F. First-principles investigation of vanadium isotope fractionation in solution and during adsorption. Earth Planet. Sc. Lett., 2015, 426, 216-224 DOI: 10.1016/j.epsl.2015.06.048.

22. Buhl, M.; Parrinello, M. Medium effects on (51)V NMR chemical shifts: A density functional study. Chem-Eur. J., 2001, 7 (20), 4487-4494 DOI: Doi 10.1002/1521-3765(20011015)7:20<4487::Aid-Chem4487>3.0.Co;2-G.

23. Leggett, C. J.; Parker, B. F.; Teat, S. J.; Zhang, Z.; Dau, P. D.; Lukens, W. W.; Peterson, S. M.; Cardenas, A. J. P.; Warner, M. G.; Gibson, J. K.; Arnold, J.; Rao, L. Structural and spectroscopic studies of a rare non-oxido V(v) complex crystallized from aqueous solution. Chem. Sci., 2016, 7 (4), 2775-2786 DOI: 10.1039/c5sc03958d.

24. Kresse, G.; Hafner, J. Ab initio molecular dynamics for liquid metals. Phys. Rev. B, 1993, 47 (1), 558.

25. Kresse, G.; Furthmuller, J. Efficiency of ab-initio total energy calculations for metals and semiconductors using a plane-wave basis set. Comp. Mater. Sci., 1996, 6 (1), 15-50 DOI: Doi 10.1016/0927-0256(96)00008-0.

26. Blöchl, P. E. Projector augmented-wave method. Phys. Rev. B, 1994, 50 (24), 17953.

27. Kresse, G.; Joubert, D. From ultrasoft pseudopotentials to the projector augmented-wave method. Phys. Rev. B, 1999, 59 (3), 1758.

28. Perdew, J. P.; Burke, K.; Ernzerhof, M. Generalized gradient approximation made simple. Phys. Rev. lett., 1996, 77 (18), 3865.

29. Humphrey, W.; Dalke, A.; Schulten, K. VMD: Visual molecular dynamics. J. Mol. Graph. Model. 1996, 14 (1), 33-38 DOI: Doi 10.1016/0263-7855(96)00018-5.

30. D.A. Case, V. B., J.T. Berryman, R.M. Betz, Q. Cai, D.S. Cerutti, T.E. Cheatham, III, T.A. Darden, R.E.; Duke, H. G., A.W. Goetz, S. Gusarov, N. Homeyer, P. Janowski, J. Kaus, I. Kolossváry, A. Kovalenko,; T.S. Lee, S. L., T. Luchko, R. Luo, B. Madej, K.M. Merz, F. Paesani, D.R. Roe, A. Roitberg, C. Sagui,; R. Salomon-Ferrer, G. S., C.L. Simmerling, W. Smith, J. Swails, R.C. Walker, J. Wang, R.M. Wolf, X.; Kollman, W. a. P. A. AMBER 14, University of California, San Francisco, 2014.

31. Joung, I. S.; Cheatham, T. E. Determination of alkali and halide monovalent ion parameters for use in explicitly solvated biomolecular simulations. J. Phys. Chem. B, 2008, 112 (30), 9020-9041 DOI: 10.1021/jp8001614.

6.7 Supplementary

Force field parameters

We created an AMBER force field for the HVO_4^{2-} by fitting bond stretching and bending modes to the B3LYP/6-31G(d) calculations.

Figure S6.1: the atom labels

Figure S6.2: fitting of the O-V-O bending

Table S6.1: atomic charges

Table S6.2: bond stretching parameters

Table S6.3: bond bending parameters

Table S6.4: Lennard-Jones Parameters

Table S6.5: comparison of B3LYP/6-31G(d) and AMBER force field

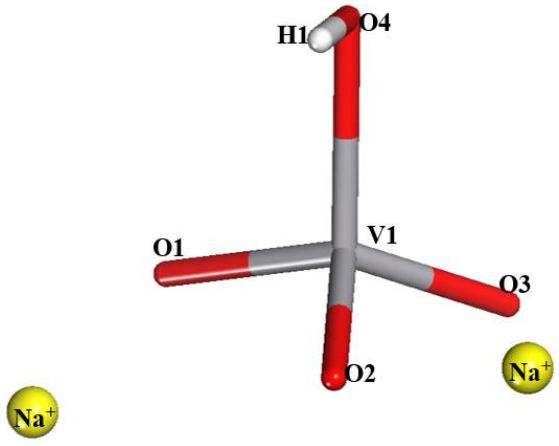

Figure S1. Atom labels for HVO_4^{2-}.

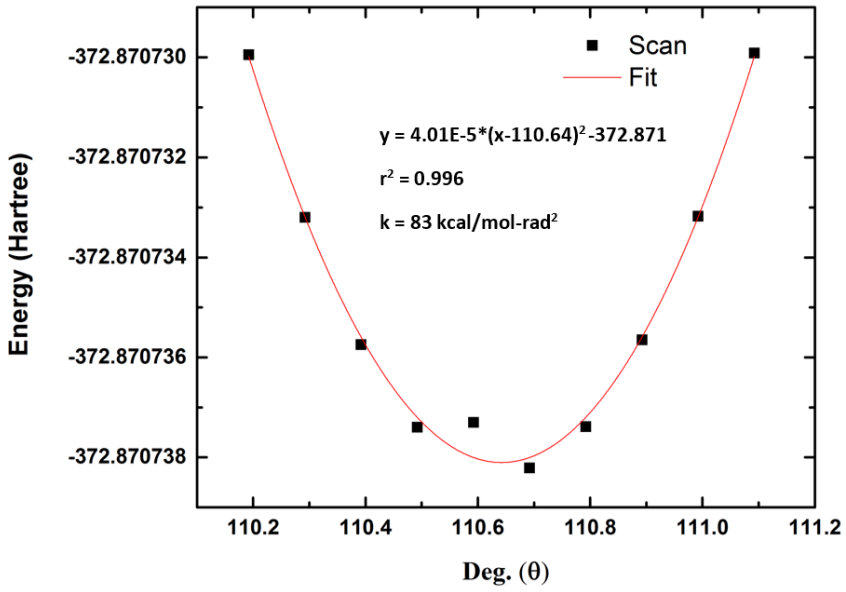

Figure S6.2. Angle scan for a O2-V1-O3 bond. The black dots are the computed data and the red line is the fitted data.

Table S6.1. Symbols and charges

Ion	Charge (|e|)
V1	+1.370592
O1	-0.915224
O2	-0.915224
O3	-0.915224
O4	-0. 918577
H1	+0.293656
Na^+	+1.000000

Table S6.2. Bond Parameters

Bond	k(kcal/mol-Å^2)	Distance (Å)
V1-O1	470.00	1.67800
V1-O2	470.00	1.67800
V1-O3	470.00	1.67800
V1-O4	420.00	1.94000
O4-H1	420.00	0.94700

*****Note the force constants were generalized from a fitted data scan and adjusted to match optimizations with B3LYP/6-31G(d).

Table S6.3. Angle Parameters

Angle	k(kcal/mol-rad^2)	Deg.
V1-O4-H1	70.000	100.160
O1-V1-O2	85.000	110.640
O1-V1-O3	85.000	110.640
O1-V1-O4	85.000	106.000
O2-V1-O3	85.000	110.640
O2-V1-O4	85.000	106.000
O3-V1-O4	85.000	108.000

*****Note the force constants were generalized from a fitted data scan and adjusted to match optimizations with b3lyp/6-31G(d).

Table S4. Lennard-Jones Parameters

Ion	ε (kcal/mol)	σ(Å)	Ref.
V1	1.4000	0.0159	1,2
O1	1.6612	0.2100	
O2	1.6612	0.2100	
O3	1.6612	0.2100	
O4	1.6612	0.2100	
H1	1.4870	0.0157	

*The parameters for vanadium are from Refs.1-2; the others are from Amber14 force field.

Table S6.5. Gas-phase bond lengths and angles of HVO_4^{2-} optimized with Gaussian09 at the B3LYP level and with AMBER using our force field (FF) parameters**.**

Angle (degree)	B3LYP	AMBER FF
O1-V-O2	112.32	112.33
O2-V-O3	112.32	112.79
O3-V-O1	111.71	113.76
O1-V-O4	109.10	105.81
O2-V-O4	101.77	102.75
O3-V-O4	109.09	108.46
Bond (Å)	B3LYP	AMBER FF
V-O1	1.67	1.67
V-O2	1.68	1.67
V-O3	1.67	1.67
V-O4	1.96	1.92
O4-H	0.97	0.94

CHAPTER SEVEN

Structural Evolution of Tc_n (n = 4−20) Clusters from First-Principles Global Minimization

7.1 Abstract

We explore the structural evolution of Tc_n (n = 4−20) clusters using a first-principles global minimization technique, namely, basin-hopping from density functional theory geometry optimization (BH-DFT). Significantly more stable structures have been found in comparison with previous models, indicating the power of DFT-based basin hopping in finding new structures for clusters. The growth sequence and pattern for n from 4 to 20 are analyzed from the perspective of geometric shell formation. The binding energy per atom, relative stability, and magnetic moments are examined as a function of the cluster size. Several magic sizes of higher stability and symmetry are discovered. In particular, we find that Tc_{19} prefers an O_h symmetry structure, resembling a piece of a face-centered-cubic metal, and its electrostatic potential map shows interesting features that indicate special reactivity of the corner.

7.2 Introduction

The study of nanometer transition metal clusters is an attractive field of study because their physical and chemical properties differ from those of their bulk.[1] In fact, research has discovered that much of their novel electronic, magnetic, and chemical

properties are strongly dependent on their large surface-to-volume ratio, shape, size, and surface termination.[2,3] Understanding these properties enables scientists to vary the composition and atomic ordering. This tuning process is significant in advancing nanotechnology with their implications in biotechnology and catalysis. Furthermore, an understanding about the step-by-step mechanism from small building blocks to a bulk system can be gained.

Technetium is a silvery gray metal.[4] It has a ground-state electronic structure [Kr] $4d^5\ 5s^2$ and has been found in many oxidation states: 0, + 2, + 4, + 5, + 6, and +7.[4,5] The element has seven valence electrons for compound formation. Under ambient conditions, Tc has a hexagonal closed-packed (hcp) structure.[6] It is the lightest radioactive element on the periodic table. The latest method for synthesizing technetium isotopes is from the fission of heavier radioactive elements, prominently uranium-235. Molybdenum-99 is a major product of uranium235 fission process. 88.75% of Molybdenum-99 undergoes beta decay with a half-life of 66 h to yield technetium-99m, while the remainder forms technetium-99.[4] Furthermore, technetium99m undergoes a gamma decay at 143 keV, half-life of 6.01 h, to become the more stable technetium-99. Technetium-99m plays an important role in nuclear medicine. It is the most commonly used isotope in diagnostic radio-imaging.[1] Furthermore, technetium-99 has shown an important role in uranium nuclear fuel cycle. The long-lived isotope, technetium-99, has raised environmental concerns due to the increase in nuclear fuel for energy.

Despite technetium's importance in nuclear medicine, the chemistry of its nanostructure is not well understood. As a starting point, we are interested in the structural evolution of Tc nanoclusters. Given the lack of experimental studies of Tc nanostructures, the motivation behind our work is twofold: (1) It serves as a prediction for future experimental studies of gasphase Tc clusters, which has not been done so far, and (2) it contrasts with previous theoretical studies[1,7] in terms of the most stable structures and their evolution with size.

Global minimization, or to predict structure given a chemical composition, is extremely difficult due to the complexity of the potential-energy landscape. First, the interaction among atoms in the chemical compound needs to be accurately described. For many inorganic/nanoscale systems, this means that one has to take the valence electrons in account explicitly, in other words, solving the Schrodinger equation for the whole system. Density functional theory has become the de facto standard to describe such systems from first principles. Nowadays by combining DFT with global minimization algorithms, one can do first-principles structure predictions for many inorganic and nanoscale systems. Two widely used global minimization methods are genetic algorithm[8] and basin-hopping (BH).[9] We chose BH here because of its simplicity and past successes in using this method for nanoclusters.[10,11] Where experiments are recalcitrant, first-principle minimization techniques provide an alternative for structure elucidation in which computational work can further chemical knowledge. Previous work examined the structural evolution of Tc (2−15) by screening a database of structures.[7] To our knowledge, no first-principles global minimization techniques have been performed in exploring a large configurational

landscape for the evolution of Tc nanostructures. We determine the structural evolution of neutral Tc_n (n = 4−20) using BH algorithm from a random initial structure. The consequence of the sequential addition of Tc atoms is explored from the binding energy, second difference plot, and magnetic moment. Further examination of chemical reactivity is also performed for a high-symmetry Tc_{19} cluster.

7.3 Computational methods

The first-principles global minimization in this work is based on the basin-hopping (BH) method coupled to DFT energy and forces. A python script was employed to run the BH algorithm on top of the DFT geometry optimization or local minimization.[12] The Vienna Ab Initio Simulation Package (VASP)[13,14] was used to perform DFT calculations with planewave basis and periodic boundary conditions. Spin-polarization was taken into account in our calculations. Spin−orbit coupling was, however, not included, because for the fifth period transition-metal elements spin−orbit coupling is not significant.[15] We have chosen the Perdew−Burke−Ernzerhof functional of the generalized-gradient approximation (GGA) for electron exchange and correlation.[16] The Kohn−Sham equations are solved with the all-electron projected augmented wave (PAW) method.[4,17,18] A cluster was placed inside a supercell of 25 × 25 × 25 $Å^3$, and the Brillouin zone was sampled by the Γ point only. Initial random structures were generated with the CALYPSO program.[19] For each cluster, at least 500 Monte Carlo steps were run to find the lowest energy structure. The detail of the DFT-based BH process has been described before.[12,20] A smaller kinetic energy cutoff was used during the DFT-BH process. After a putative global minimum was found, a higher energy cutoff (400 eV) was used for finer geometry optimization. For small

clusters such as n = 4−10, we used only one initial guess for the BH process, while two or more initial guesses (that is, parallel BH runs) were performed for larger cluster sizes (n = 11−20). The binding energy of a cluster was calculated with the following formula:

$$E_b(n) = \frac{-[E(\mathrm{Tc}_n) - nE(\mathrm{Tc})]}{n}$$

where $E(Tc_n)$ is the total energy of the Tc_n cluster and E(Tc) is the energy of an isolated Tc atom. The relative stability of the Tc_n clusters was assessed with the second difference of binding energies from the following formula

7.4 Results & discussion

7.4.1 Putative global minima of Tc_n (n = 4−20) clusters

The putative global minima of Tc_4 to Tc_{20} from our DFT-BH process are shown in Figure 7.1. When a growth pattern is recognizable, the progressive addition of a Tc atom is indicated in red to suggest the pattern. One can see that the evolution of Tc_4 to Tc_9 is straightforward. Tc_4 begins as a rectangle. The two longer bonds have a length of 2.43 Å and the shorter bonds have a length of 1.96 Å. We note that this rectangular structure is 1.5 eV more stable than the tetrahedron reported previously.[7,22] The preference of the rectangle can be explained by the triple bond characteristic in the shorter bonds. Tc_5 is formed by the addition of a Tc atom above the plane. Tc_6 prefers the octahedron structure, as proposed by other researchers,[7,22] with a bond length of 2.39 Å. Tc_7 is a low symmetry cluster and can be viewed as the expansion of an octahedral vertex to an edge.

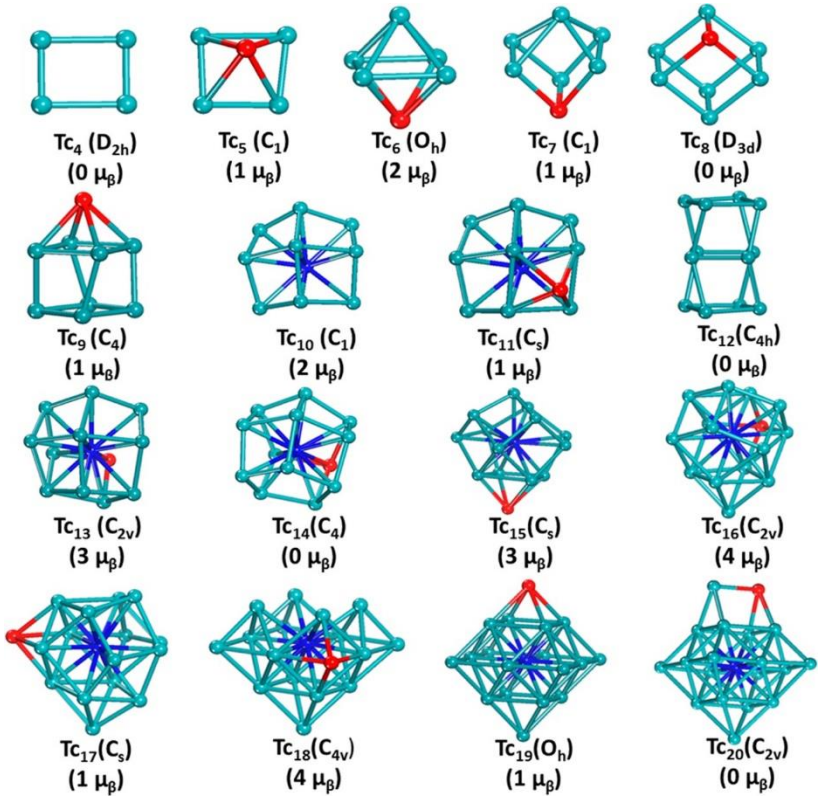

Figure 7.1 Putative global minima of Tc_n (n = 4−20) clusters. The red Tc atom represents the site of addition in Tc_n relative to Tc_{n-1}. The highest coordination Tc atom is highlighted in blue. The total magnetic moment for each cluster is also provided. The coordinates for these structures are provided in the Supporting Information.

The addition of a Tc atom to Tc_7 gives Tc_8, a cube-like shape with a symmetry of D_{3d}. The bond lengths are 2.35 and 2.29 Å. The addition of a Tc atom into Tc_8 gives Tc_9 an apex to the cube-like structure that distorts the cube-like scaffold; the structure has C_4 symmetry. The addition of a Tc atom into Tc_9 shows dramatic structure change from the prior flow of sequence: it goes from a geometric scaffold to a face; this is also a size where a central Tc atom (highlighted in blue in Figure 7.1) or a nucleation point emerges. Interestingly, structures similar to Tc_n ($n = 7-9$) have been found for cationic ruthenium clusters.[23] The Tc_{10} structure has a bilaterallike symmetry across the middle of the structure with bonds varying in length of 2.30 to 2.50 Å. Tc_{10} is the beginning of a core-shell structure. Tc_{11} is closely related to Tc_{10}: The addition of a Tc atom onto Tc_{10} caps one of the square faces.

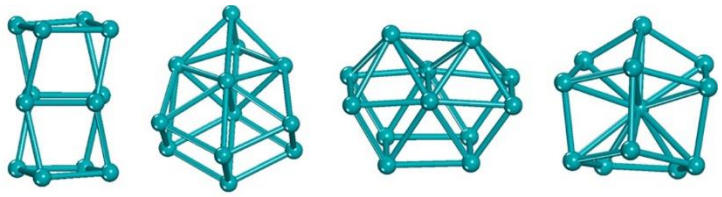

Isomer	1	2	3	4
ΔE (eV)	0	0.40	0.47	0.49

Figure 7.2 Low-lying isomers for Tc_{12}. The isomer energies are compared with the most stable structure (0 eV) in increasing order.

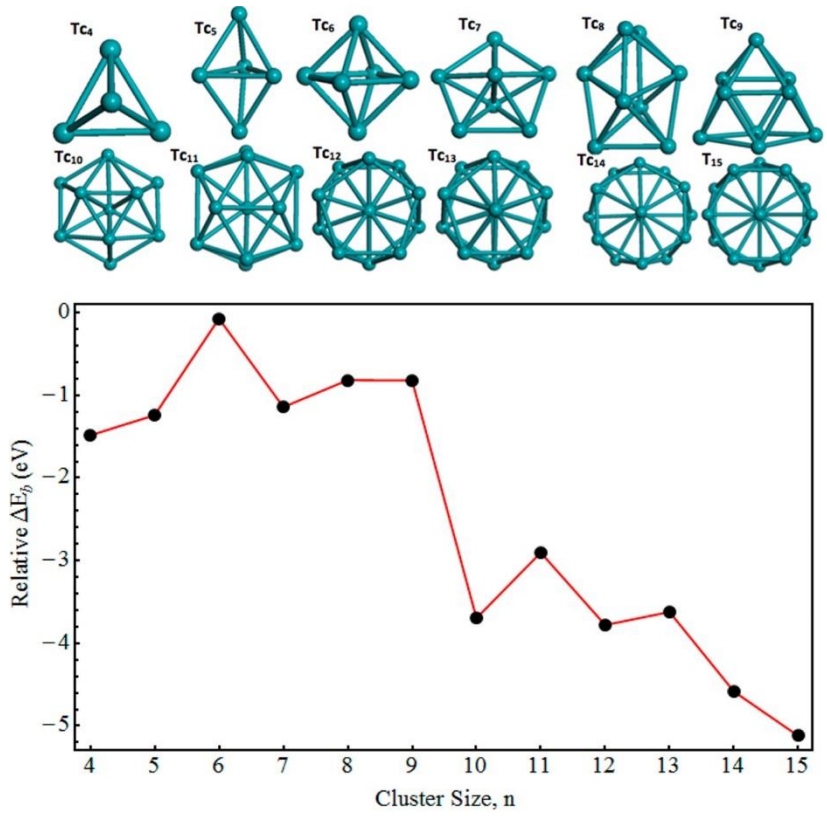

Figure 7.3 Energy difference between our putative global minimum (Figure 7.1) and the structure from ref 7 (top) for Tc_n. The energies for the structures from ref 7 are set at zero.

Tc_{12} is interesting in that its global minimum has a twisted double-cube structure, different from the growth trend from Tc_{10} to Tc_{11}; however, among the several low-lying isomers of Tc_{12} (Figure 7.2), we did find one that follows that growth trend but its energy is ~0.5 eV higher in energy (isomer 4). The double-cube structure of Tc_{12} is more related to Tc_8 and Tc_9.

The growth trend in Tc_{10} and Tc_{11} is recovered in Tc_{13} and Tc_{14}: The clusters are growing around the central atom. Tc_{14} corresponds to the first shell closing. A new aspect appears in Tc_{15}: a corner atom grows out (the red atom in the Tc_{15} structure in Figure 7.1), which is not directly connected to the central atom, suggesting the formation of a second shell. Tc_{15} through Tc_{19} has a fluid sequence of additions of Tc corner atoms in the second coordination shell around the central atom, leading to the formation of a stable and highly symmetric (O_h) Tc_{19} cluster with bond lengths of 2.51 to 2.52 Å, just like a piece of the bulk face-centered-cubic (fcc) structure. Here we note that the bulk Tc metal has a hexagonal-close-packed (hcp) structure, but interestingly, the Tc_{19} nanocluster has a fcc structure. The Tc_{20} structure follows the octahedron of Tc_{19} by turning a corner atom to an add-on edge. The structural evolution of Tc clusters resembles that of ruthenium clusters reported by Waldt et al.[25] Their results were obtained experimentally using anion-trapped ion electron diffraction (TIED) and then compared with structures obtained using DFT calculations. While their DFT method utilized genetic algorithm, we see similarities to our results. The Ru clusters' structure evolution begins on a very similar cubic structural pathway from 4 to 9 with dissimilar double-layer hexagonal pathway from 10 to 17 that converges to a similar cubic pathway at clusters 18 to 20 structures.[24,25] The 19-atom Ru

cluster is very similar to our Tc_{19} cluster. Interestingly, manganese shows a drastically different structural evolution.[26] The Mn_7 cluster adopts a pentagonal bipyramidal, while Mn_8 and Mn_9 adopt a bicapped octahedron and a centered antiprism, respectively. All of the intermediate-sized Mn clusters n = 11−20 adopt an icosahedral growth pattern.

A previous computational study examined the geometry and electronic structure of Tc_n (n = 4−15) clusters.[7] We compare the relative energies between our structures and theirs in Figure 7.3. One can see that except Tc_6 (for which our structures and theirs are the same), our structures are over 1.0 eV lower in energy for Tc_4 to Tc_9 and over 3.0 eV lower in energy for Tc_{10} to Tc_{15}. The difference between their study and ours is that we used a global-minimization method (basin hopping), while they just used the high-symmetry structures from the previous literature for other clusters.[7] This reflects the power of the DFT-based basin hopping approach as a first-principles global minimization technique to generate better structures for metal clusters.

7.4.2 First and second difference binding energy for cluster evolution

Next, we examine the stability of the cluster as the size increases. Figure 7.4 is a plot of the binding energy per atom, which is a measure of the overall stability of a cluster.

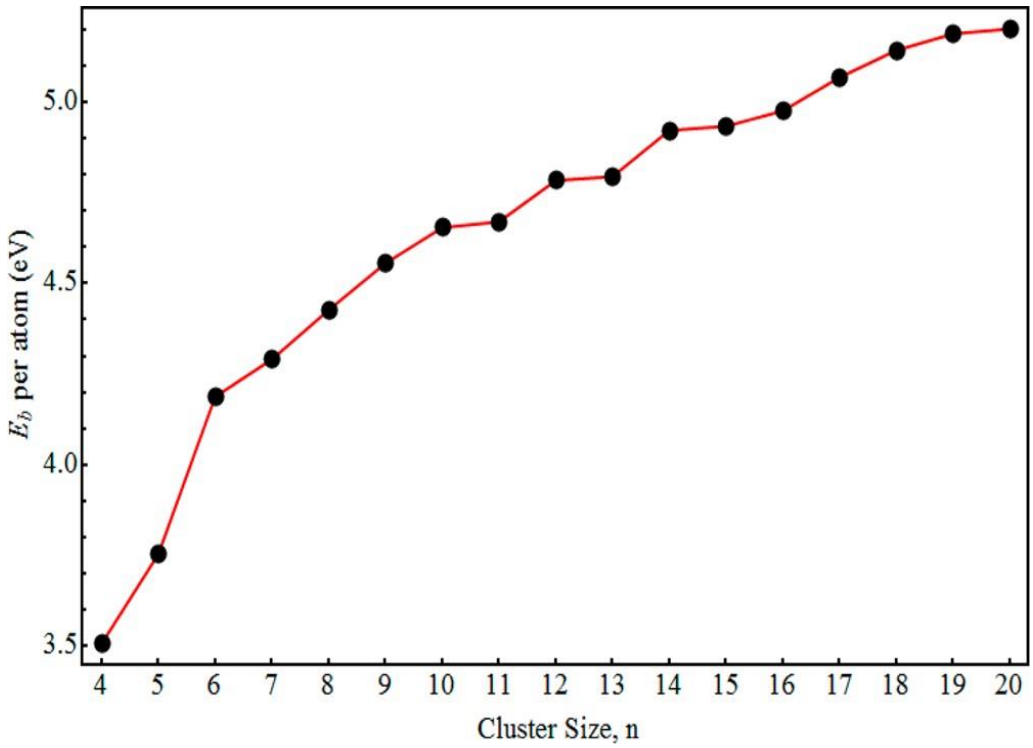

Figure 7.4 Binding energy (eV per atom) for Tcn (n = 4-20) clusters.

The binding energy starts at 3.5 eV for Tc_4 and asymptotically approaches 5.2 eV. This curve shows that on a per atom basis the stability of the cluster increases with the cluster size and eventually will approach the bulk value. This general trend is true for most of metal clusters because the ratio of the atoms in the bulk versus on the surface increases with the cluster size and the bulk atom is lower in energy than the surface atom.

Magic numbers, or cluster sizes of higher relative stability against neighboring sizes are often invoked in the discussion of metal clusters. The relative cluster stability is determined with the second difference of binding energies (see the Method section), which is shown in Figure 7.5 for Tc_n. There are distinctive peaks at cluster sizes 6, 10, 12, 14, and 18, indicating their higher relative stability than their neighbors. The higher relative stability of Tc_6 originates from its high symmetry or the octahedron structure.

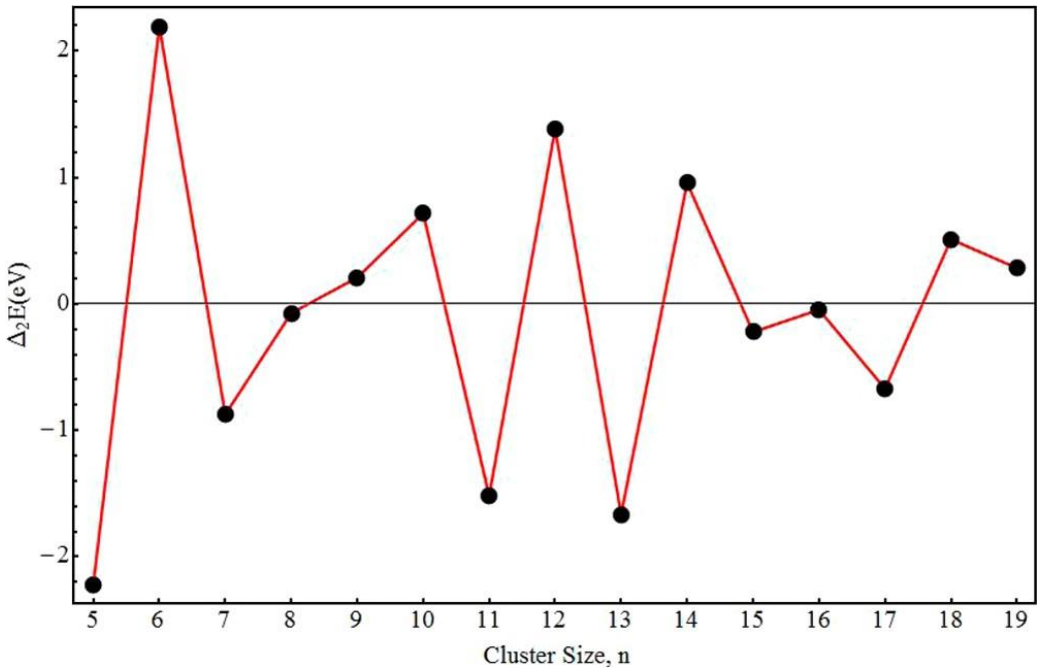

Figure 7.5 Second difference of binding energies (see the Method section) of Tc_n (n = 5−19) clusters.

Tc_{10}'s stability may be enhanced due to the emergence of the central atom, while Tc_{12}'s higher stability is probably closely related to its double-cube structure. In Tc_{14}'s structure, the first coordinate shell around the central atom is completed and this geometric closure may give Tc_{14} a higher relative stability. The higher stability of Tc_{18} than Tc_{17} probably originates from its higher symmetry (C_{4v} vs C_s). The similar stability between Tc_{18} and Tc_{19} is due to their similar structures. Bulk technetium metal is paramagnetic, so can be Tc clusters. We examined the total magnetic moments of Tc_n clusters (Figure 7.6). When n = 4, 8, 12, 14, and 20, the cluster is nonmagnetic.

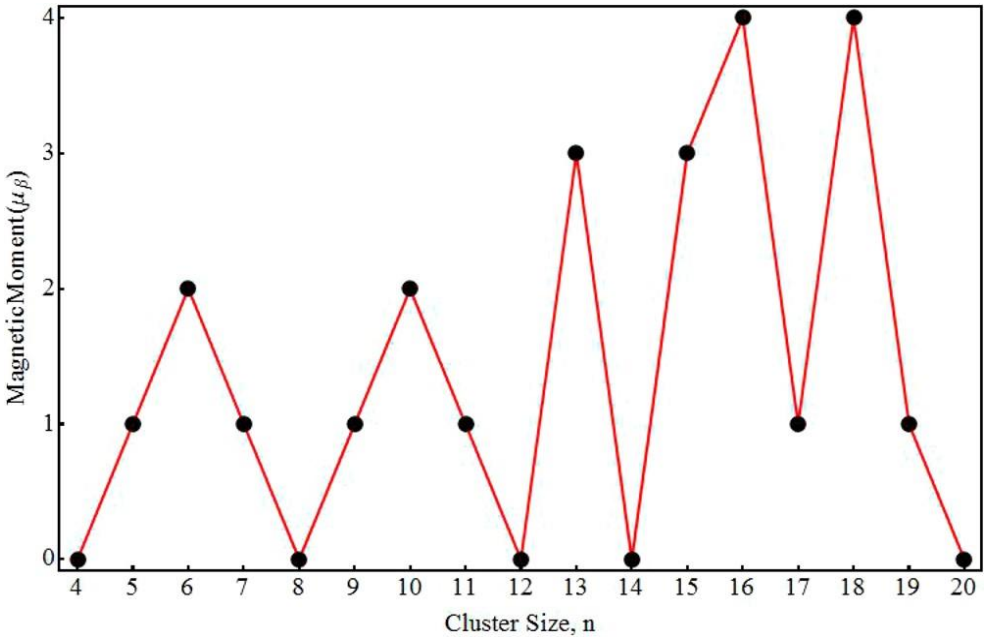

Figure 7.6 Magnetic moment of the Tc_n cluster with increasing cluster size for the lowest-energy structure (see Figure 7.1).

7.4.3 Magnetic Moment for Tc_n (n = 4−20) clusters

In other words, these clusters have a closed-shell singlet ground state. For other sizes, the clusters are magnetic with varying magnetic moments. The most common magnetic moment is 1 μ_B, for n = 5, 7, 9, 11, 17, and 19. The largest is 4 μ_B for clusters n = 16 and 18. Previously, Zhang et al. calculated a Tc_{13} isomer with the same magnetic moment of 3 but with a different structure,[27] and Tc_6 has also been shown to have a total magnetic moment of 2 μ_B.[28]

7.4.4 Adsorption Analysis for Tc_{19} + (1/2) X_2 = $Tc_{19}X$

Tc_{19} stands out as an interesting finding from our first principles structure search. Its high symmetry and bulk-like structure prompted us to further examine its chemical properties. The electrostatic potential map of the neat Tc_{19} cluster (Figure 7.7, left) shows that the corner Tc atoms are more negative than the edge Tc atoms, suggesting a higher reactivity at the corner sites. We tested this idea by adsorption of fluorine,

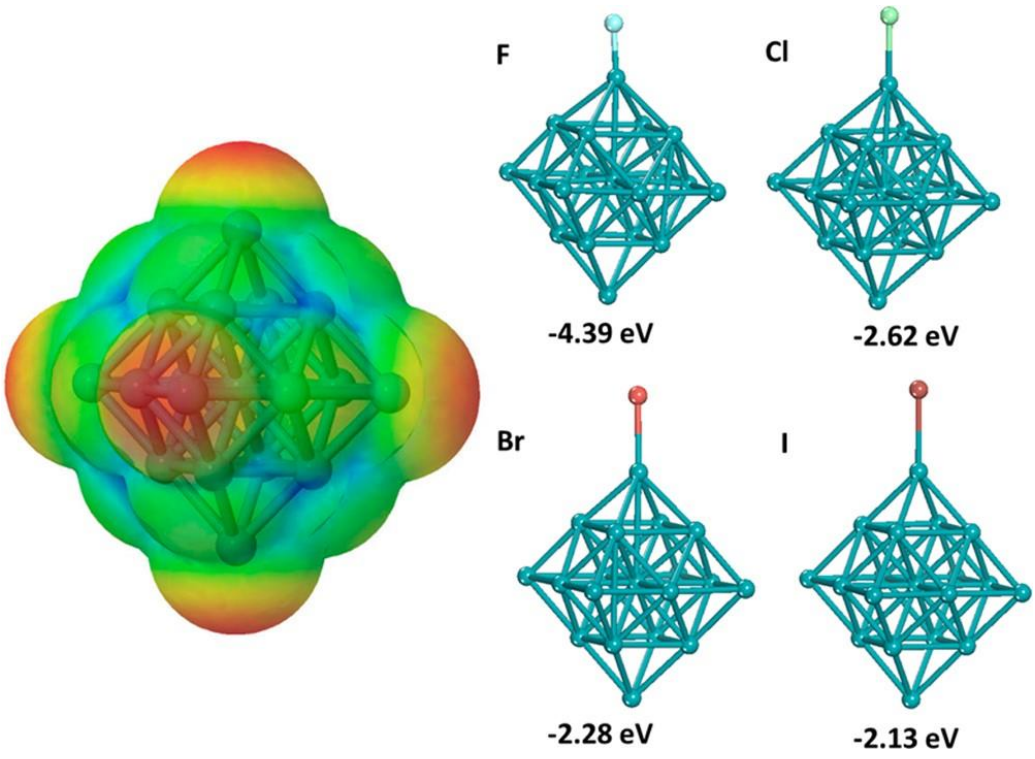

Figure 7.7 Left: electrostatic potential map of the neat Tc_{19} cluster. Red represents more electronegative and blue represents less electronegative. Right: the $Tc_{19}X$ (X = F, Cl, Br, and I) structures; shown beneath each structure are the adsorption energies according to $Tc_{19} + (1/2)\ X_2 = Tc_{19}X$.

chlorine, bromine, and iodine and found that the halogen atoms adsorb to the corners of Tc_{19}, as predicted by the electrostatic potential; the facet sites on Tc_{19} are much less reactive. We also see a trend of decreasing adsorption energy of the $Tc_{19}X$ complex going down the periodic table, in agreement with the decreasing electronegativity. The electron-rich corner site and the high electronegativity of fluorine make the Tc_{19}–F bonding the strongest.

7.5 Conclusion

The putative global minima of Tc_n (n = 4–20) clusters were predicted using DFT-based basin hopping for first-principles global minimization. Except for Tc_6, all of the structures were found to be more stable than previous models.[7] The computed binding energy per atom varies steadily from 3.5 eV for Tc_4 to 5.2 eV for Tc_{20} with higher relative stability appearing at n = 6, 10, 12, 14, and 18. Tc_6 has an octahedral structure, while Tc_{10} has a double-cube geometry. Tc_{12} corresponds to the closure of the first geometric shell around a central atom, while Tc_{19} signifies the formation of the high-symmetry octahedral structure with all corner sites filled. The chemical reactivity of the Tc_{19} corner sites was probed by halogen adsorption. This work demonstrates the unique structural evolution of Tc nanoclusters and the power of first-principles global minimization.

7.6 References

1. Dilworth, J.; Parrott, S. The Biomedical Chemistry of Technetium and Rhenium. Chem. Soc. Rev. 1998, 27, 43–55.

2. Chang, C.; Chou, M. Alternative Low-symmetry Structure for 13Atom Metal Clusters. Phys. Rev. Lett. 2004, 93, 133401.

3. Piotrowski, M. J.; Piquini, P.; Da Silva, J. L. Density Functional Theory Investigation of 3 d, 4 d, and 5 d 13-Atom Metal Clusters. Phys. Rev. B: Condens. Matter Mater. Phys. 2010, 81, 155446.

4. Hammond, C. R. The Elements. In CRC Handbook of Chemistry and Physics, 96th ed.; CRC Press: Boca Raton, FL, 2015; pp 4−35.

5. Mazzi, U. Technetium in Medicine. In Technetium-99m Pharmaceuticals; Springer: Berlin, 2007; p 8.

6. Kittel, C. Introduction to Solid State Physics, 7th ed.; Wiley: New York, 1996; p 23.

7. Weck, P. F.; Kim, E.; Poineau, F.; Czerwinski, K. R. Structural Evolution and Properties of Subnanometer Tc n (n= 2−15) Clusters. Phys. Chem. Chem. Phys. 2009, 11, 10003−10008.

8. Deaven, D. M.; Ho, K. M. Molecular Geometry Optimization with a Genetic Algorithm. Phys. Rev. Lett. 1995, 75, 288−291.

9. Wales, D. J.; Doye, J. P. Global Optimization by Basin-Hopping and the Lowest Energy Structures of Lennard-Jones Clusters Containing Up to 110 Atoms. J. Phys. Chem. A 1997, 101, 5111−5116.

10. Bai, J.; Cui, L.-F.; Wang, J.; Yoo, S.; Li, X.; Jellinek, J.; Koehler, C.; Frauenheim, T.; Wang, L.-S.; Zeng, X. C. Structural Evolution of Anionic Silicon Clusters Si N (20≤ N≤ 45). J. Phys. Chem. A 2006, 110, 908−912.

11. Goedecker, S. Minima Hopping: An Efficient Search Method for the Global Minimum of the Potential Energy Surface of Complex Molecular Systems. J. Chem. Phys. 2004, 120, 9911−9917.

12. Jiang, D. e.; Walter, M.; Dai, S. Gold Sulfide Nanoclusters: A Unique Core-In-Cage Structure. Chem. - Eur. J. 2010, 16, 4999−5003.

13. Kresse, G.; Furthmüller, J. Efficiency of ab-initio Total Energy Calculations for Metals and Semiconductors Using a Plane-Wave Basis Set. Comput. Mater. Sci. 1996, 6, 15−50.

14. Kresse, G.; Hafner, J. Ab initio Molecular Dynamics for Liquid Metals. Phys. Rev. B: Condens. Matter Mater. Phys. 1993, 47, 558.

15. Ronca, E.; De Angelis, F.; Fantacci, S. Time-Dependent Density Functional Theory Modeling of Spin−Orbit Coupling in Ruthenium and Osmium Solar Cell Sensitizers. J. Phys. Chem. C 2014, 118, 17067−17078.

16. Perdew, J. P.; Burke, K.; Ernzerhof, M. Generalized Gradient Approximation Made Simple. Phys. Rev. Lett. 1996, 77, 3865.

17. Blöchl, P. E. Projector Augmented-Wave Method. Phys. Rev. B: Condens. Matter Mater. Phys. 1994, 50, 17953.

18. Kresse, G.; Joubert, D. From Ultrasoft Pseudopotentials to the Projector Augmented-Wave Method. Phys. Rev. B: Condens. Matter Mater. Phys. 1999, 59, 1758.

19. Wang, Y.; Lv, J.; Zhu, L.; Ma, Y. CALYPSO: A Method for Crystal Structure Prediction. Comput. Phys. Commun. 2012, 183, 2063−2070.

20. Jiang, D.-e.; Walter, M. Au_{40}: A Large Tetrahedral Magic Cluster. Phys. Rev. B: Condens. Matter Mater. Phys. 2011, 84, 193042.

21. Perdew, J. P.; Wang, Y. Accurate and Simple Analytic Representation of the Electron-Gas Correlation-Energy. Phys. Rev. B: Condens. Matter Mater. Phys. 1992, 45, 13244−13249.

22. Sekine, R.; Kondo, R.; Yamamoto, T.; Onoe, J. Geometric and Electronic Structures of Tc and Mn Clusters by Density Functional Calculations. Radiochemistry 2003, 45, 233−236.

23. Kerpal, C.; Harding, D. J.; Rayner, D. M.; Lyon, J. T.; Fielicke, A. Far-IR Spectra and Structures of Small Cationic Ruthenium Clusters: Evidence for Cubic Motifs. J. Phys. Chem. C 2015, 119, 10869−10875.

24. Waldt, E.; Ahlrichs, R.; Kappes, M. M.; Schooss, D. Structures of Medium-Sized Ruthenium Clusters: the Octahedral Motif. Chem. Phys. Chem. 2014, 15, 862−865.

25. Waldt, E.; Hehn, A. S.; Ahlrichs, R.; Kappes, M. M.; Schooss, D. Structural Evolution of Small Ruthenium Cluster Anions. J. Chem. Phys. 2015, 142, 024319.

26. Kabir, M.; Mookerjee, A.; Kanhere, D. G. Structure, Electronic Properties, and Magnetic Transition in Manganese Clusters. Phys. Rev. B: Condens. Matter Mater. Phys. 2006, 73, 224439.

27. Sun, Y.; Fournier, R.; Zhang, M. Structural and Electronic Properties of 13-Atom 4 d Transition-Metal Clusters. Phys. Rev. A: At., Mol., Opt. Phys. 2009, 79, 043202.

28. Alonso, J. Electronic and Atomic Structure, and Magnetism of Transition-Metal Clusters. Chem. Rev. 2000, 100, 637−678.

7.7 Supplementary

Coordinates for the structures in Figure 1 of the main article.

Tc_4

4

Tc	6.605139	7.863131	3.826899
Tc	6.575552	5.900373	4.106532
Tc	7.855294	6.177839	6.101682
Tc	7.876111	8.142362	5.828027

Tc5

5

Tc	8.622577	5.058203	6.434958
Tc	7.463801	6.904989	6.459774
Tc	7.077801	4.530112	4.187826
Tc	8.046647	6.507484	4.305968
Tc	6.384046	4.640835	6.278943

Tc6

6

Tc	8.275673	6.202207	8.700737
Tc	6.557453	6.420604	5.799219
Tc	7.725196	4.682042	6.951553
Tc	8.841904	6.725224	6.425637
Tc	7.122623	7.942880	7.547261

Tc 5.988555 5.897967 8.062558

Tc_7

7

Tc 3.344689 8.494651 6.109771

Tc 3.667915 6.298438 5.545708

Tc 4.918565 6.901265 3.361375

Tc 5.621172 8.886290 6.092441

Tc 5.831408 6.605270 5.618861

Tc 3.300462 8.473086 3.806581

Tc 5.680595 8.977481 3.798353

Tc8

8

Tc 6.550091 8.620362 9.719332

Tc 4.403282 9.252318 7.081266

Tc 6.314817 6.352168 7.079581

Tc 4.078627 6.936374 9.098470

Tc 6.651886 8.673905 7.366238

Tc 4.374033 9.244969 9.380507

Tc 6.363363 6.369700 9.371536

Tc 4.143901 6.995508 6.751002

Tc9

9

Tc	7.420670	3.844887	8.574400
Tc	4.705546	5.860687	6.484896
Tc	6.912028	6.103146	8.434300
Tc	5.185043	3.347415	8.946706
Tc	5.477009	4.360535	4.724743
Tc	4.405201	3.520330	6.745209
Tc	7.031054	5.533481	6.173073
Tc	4.676813	5.601672	8.808541
Tc	6.731414	3.191675	6.448152

Tc10

10

Tc	10.857943	7.612972	11.374175
Tc	9.155792	9.055482	11.987849
Tc	12.835703	11.408915	10.745342
Tc	10.833187	10.336361	12.779984
Tc	10.847099	12.203768	11.474225
Tc	12.512546	10.849955	8.574481
Tc	12.874106	8.702120	9.311946
Tc	12.712221	9.094438	11.733563
Tc	10.909650	7.612575	9.083666
Tc	10.884104	9.899866	10.305793

Tc11

11

Tc	6.778654	7.446468	9.041682
Tc	10.942282	6.920550	5.951371
Tc	7.888355	5.009048	6.343226
Tc	6.489535	6.693253	6.735433
Tc	7.816254	8.674633	6.000055
Tc	10.190356	8.970984	8.856559
Tc	10.252875	8.969103	6.541733
Tc	8.837975	7.126001	7.571695
Tc	5.868172	8.954258	7.450237
Tc	8.904928	6.622385	5.056379
Tc	8.068436	9.411511	8.388215

Tc12

12

Tc	12.541349	13.452715	13.610496
Tc	12.432636	11.815511	11.838281
Tc	9.483476	13.071252	11.186551
Tc	12.620106	11.528620	9.429433
Tc	9.367344	11.444062	9.394640
Tc	10.981253	12.932423	8.666687
Tc	10.921878	11.975554	14.333103
Tc	11.547032	13.894955	10.838945
Tc	9.274812	13.374437	13.571027
Tc	11.011515	9.976281	10.029900
Tc	10.892702	14.909166	12.986108

Tc 10.356147 10.984974 12.164753

Tc13

13

Tc 7.485796 8.144383 7.066212

Tc 5.374977 5.622173 3.667972

Tc 5.965306 7.915322 4.960073

Tc 5.417209 6.740055 7.083797

Tc 8.458972 7.177034 5.325075

Tc 6.787545 9.015575 2.730642

Tc 6.335071 10.170195 6.324672

Tc 3.664647 8.712363 4.432679

Tc 4.464567 9.006365 6.725735

Tc 4.993552 7.739187 2.520131

Tc 5.535660 10.309563 4.038187

Tc 3.914837 6.365237 5.157663

Tc 6.958994 5.560205 5.546861

Tc_{14}

14

Tc 18.124124 12.217490 11.784458

Tc 19.807916 13.177205 13.018353

Tc 18.526461 13.683122 10.072402

Tc 17.825899 14.783908 12.373561

Tc 16.189781 16.429073 13.335059

Tc	16.668557	14.429274	14.643573
Tc	18.517024	16.744762	13.910825
Tc	18.955591	14.667739	14.794023
Tc	19.379965	16.880982	11.787925
Tc	15.290542	14.647424	11.942756
Tc	16.132939	12.833394	13.065346
Tc	20.225334	14.630352	11.298694
Tc	16.530132	15.079301	10.049858
Tc	17.165784	16.976524	11.182443

Tc15

15

Tc	10.447242	12.643660	9.873528
Tc	9.922674	14.979077	12.522249
Tc	9.838648	12.608734	12.311746
Tc	7.853848	12.098878	9.239335
Tc	10.714929	9.973474	10.318142
Tc	11.802065	14.155499	11.364894
Tc	9.880783	15.192225	9.915893
Tc	8.254350	13.838827	10.671520
Tc	12.659710	14.087989	9.063830
Tc	10.651554	14.423228	7.847460
Tc	9.558205	12.340335	7.536096
Tc	11.221897	10.767524	8.164478
Tc	12.976096	11.859133	9.275316
Tc	8.739834	10.826772	11.006744

Tc 12.055992 11.556170 11.463493

Tc16

16

Tc 11.639569 12.154565 13.839175

Tc 9.866163 10.972295 12.410156

Tc 11.610643 9.617104 13.693265

Tc 13.365072 10.935553 12.397127

Tc 13.682088 13.332091 12.668375

Tc 11.652705 14.535191 12.827032

Tc 9.596887 13.371257 12.772312

Tc 11.662174 11.862092 16.381918

Tc 11.631749 12.147799 11.290653

Tc 11.629957 9.398271 16.137406

Tc 13.381700 10.757106 15.122774

Tc 13.703106 13.164363 15.070074

Tc 11.668053 14.368359 15.180116

Tc 9.610792 13.199065 15.156676

Tc 9.911338 10.781241 15.155856

Tc 11.604505 9.676974 11.279260

Tc17

17

Tc 10.448296 11.769464 14.578112

Tc 11.878065 11.392338 12.563024

Tc 12.753327 8.777676 11.976158

Tc 10.098463 12.402765 11.110591

Tc 11.110976 9.871344 10.535829

Tc 12.850918 12.593954 14.717825

Tc 8.658678 12.713406 13.050186

Tc 14.051371 13.015766 12.739133

Tc 11.457643 9.353360 14.042788

Tc 12.567657 13.464184 11.020335

Tc 9.567223 10.439269 12.445734

Tc 14.280573 10.676966 11.994902

Tc 13.718400 10.335125 14.393224

Tc 10.910078 13.648802 13.064267

Tc 10.526322 8.051583 12.178683

Tc 12.874922 11.374029 10.062293

Tc 12.112113 10.611693 16.093741

Tc18

18

Tc 15.208509 9.975626 13.839763

Tc 16.240502 8.562994 11.963923

Tc 17.508251 10.497217 12.945566

Tc 13.052345 11.284187 13.237259

Tc 14.900762 7.781030 15.117800

Tc 15.932760 6.451557 13.220448

Tc 15.630241 11.990250 12.278763

Tc 11.983255 9.446587 12.339164

Tc 17.164081 8.375832 14.262897

Tc 16.738096 11.755967 14.937665

Tc 12.926132 9.274362 14.685613

Tc 16.565453 10.708434 10.614750

Tc 14.283844 10.062721 11.486573

Tc 13.973200 7.958513 12.820282

Tc 18.472133 10.292057 15.275530

Tc 14.125612 11.081331 15.896893

Tc 13.853787 9.090688 17.026926

Tc 16.156014 9.683546 16.156159

Tc19

19

Tc 5.080804 8.588070 6.761929

Tc 5.108144 9.447162 9.117830

Tc 8.770731 6.304052 6.196732

Tc 7.926380 10.576266 6.001327

Tc 7.291468 9.926663 10.261099

Tc 7.270757 9.060660 7.900814

Tc 8.821613 8.044561 10.951741

Tc 6.608087 6.686967 7.429664

Tc 5.769442 10.962798 7.216651

Tc 9.435719 8.674175 6.685755

Tc 6.618114 7.543993 9.799749

Tc 9.460613 9.544059 9.042892

Tc 5.742443 10.100989 4.845553

Tc 7.255606 8.202245 5.541151

Tc 4.416932 7.067972 8.663762

Tc 7.954530 11.433811 8.365113

Tc 10.128204 11.055314 7.124033

Tc 8.785074 7.170799 8.577186

Tc 5.778134 11.835769 9.585412

Tc20

20

Tc 4.996767 8.187110 5.785647

Tc 8.464360 12.308322 8.926724

Tc 7.915200 10.571439 7.219259

Tc 8.926983 10.755612 4.894880

Tc 6.975101 12.874012 6.980365

Tc 6.308550 8.636697 7.778446

Tc 9.349876 9.953232 9.160844

Tc 10.907767 11.851484 8.636923

Tc 10.341064 10.110440 6.911272

Tc 9.447022 12.464097 6.685398

Tc 6.882923 10.425031 9.542046

Tc 7.659483 8.132469 9.788327

Tc 8.735587 8.226394 7.405211

Tc 7.329319 8.804013 5.442303

Tc 6.402648 11.203512 5.232146

CHAPTER EIGHT

Conclusions & Future work

8.1 Conclusions

One key component of this work is to provide appropriate steps to modelling uranium in a "real system" utilizing various computational methods. An ideal real system consists of poly(AO) braids latched to a carbon base material on the sea floor free-floating in a seawater related conditions containing other competing ions. However before achieving this huge goal, intermediate questions need to be asked to move towards the development of an ideal chemical system. In this work theoretical model systems address how surrounding seawater mediums interact and influence complexed uranium and vanadium species towards uranium recovery.

In the beginning we wanted to address the solvation effects on the coordinated uranium specie. Starting with work on the dominant neutral $Ca_2[UO_2(CO_3)_3]$ specie, we investigated the influence of surrounding water molecules on coordinating calcium ions from a pure DFT perspective. From this QM perspective, interesting polarization effects are observed from the electrostatic interaction of surrounding water molecules. This first hydration shell causes one Ca counterion to bind stronger to the $[UO_2(CO_3)_3]^{4-}$ than the other Ca counterions. This asymmetrical of binding between the two Ca ions is reflected in several aspects: the stronger-binding Ca ion has shorter $Ca–O_{carbonate}$ bonds, shorter Ca–U distance, and four coordinating water molecules, while the weaker-binding Ca has longer

$Ca–O_{carbonate}$ bonds, longer Ca–U distance, and five coordinating water molecules.[1] Following this work, other simulation related to calcium binding and influence of seawater on Ca2[UO2(CO3)3]. As such, utilizing CPMD-type calculations found that as one of the coordinating calcium ions dissociates leads to the conversion a bidentate chelating motif to a monodentate chelating motif follows. Also, simulation on the solvation of $Ca_2[UO_2(CO_3)_3]$ ternary complex in model seawater revealed one Na^+ closely associates with the dominant uranium complex which could play a role designing ligands.[2] Along the same lines, calculating free-energy binding process of Ca^{2+} with $[UO_2(CO_3)_3]^{4-}$ in the presence of NaCl simulated seawater revealed the complexation chemistry of uranyl is influence by the presence of Na^+ by changing the coordination mode of one of the interacting carbonate groups.[3]

Next step is to address coordination uranyl-AO type systems in seawater related conditions. Using a combinational computational study using DFT-MD and CMD explored uranyl-amidoxime type, open-ligand binding utilizing umbrella sampling, to pry into uranyl-AO coordination in seawater-related environments by calculated relative binding-free energies. We simulated the free energies of sequential ligand binding to form UO_2B, $[UO_2B_2]^{2–}$, and $[UO_2(HB)B]^–$ with umbrella sampling. The work revealed a cooperative binding mode consisting of distorted eat2 and k2 binding bonds for seawater related composition. Very good agreement with the experimental values was achieved, which corroborates our structural insights into the binding mode.[4] Further work utilized CMD assisted umbrella sampling to map the displacement of three carbonates in $Ca_2[UO_2(CO_3)_3]$ by the simple acetaamidoximate (AO^-) and the more complex glutaradiamidoximate (B^{2-}

/BH^-). Simulations exposed Ca^{2+} ions can facilitate the displacement of two carbonate groups to depart as the neutral CaCO3 and the last carbonate chemical departure is assisted with an additional Ca^{2+}. Also, the work illustrated the presence of Na^+ is can mediate the carbonate displacement.[5]

The next step is to reveal insight to the role of inclusion of carboxylate functional groups to the polymer system. A bifunctional AO-Ac model was then constructed to explore the enhanced adsorption stability of uranyl-(AO/Ac), along the so called "synergetic effect" of an incorporated hydrophilic functional group, such as carboxylate. Employing umbrella sampling to model the binding strength by the inclusion of a carboxylate functional group into a poly(AO) will increase the binding stability towards uranyl. In this, a cis- and trans- analysis illustrated the cis- conformation shows the increased intermolecular interaction between carboxylate groups increases sodium ion and water hydration around the uranyl-$(hybrid)_2$.

Additionally, DFT-MD and CMD assisted umbrella sampling explored the solvation of the most aggressive competing metal ions, vanadium, interaction with one of the dominant vanadium species, HVO_4^{2-}. Molecular dynamics simulations show that vanadium(V) exists as $NaHVO_4^-$ in seawater. Modelling the Na^+ dissociation utilizing umbrella sampling shows the solvation of states of Na^+ ion in $NaHVO_4^-$ has two interchangeable states: bidentate and monodentate. In the bidentate state, the Na^+ ion interacts with two vanadate oxo- groups, whereas in the monodentate state, the Na^+ ion interacts with only one vanadate oxo- group.[6] Free energy calculation reveal a small energy barrier separating two states in $NaHVO_4^-$ after dissociation.

Finally, as training, technetium nanocluster evolution is explored with a global minimization technique called DFT-BH to provide insight to putative structures along with chemical property analysis. This work demonstrates the unique structural evolution of Tc_n (n=4-20) nanoclusters and the power of first-principles global minimization. Computed binding energy per atom varies monotonically from 3.5 eV for Tc_4 to 5.2 eV for Tc_{20} with higher relative stability appearing at n = 6, 10, 12, 14, and 18. Tc_{12} corresponds to the closure of the first geometric shell around a central atom, while Tc_{19} signifies the formation of the high-symmetry octahedral structure with all corner sites filled. The chemical reactivity of the Tc_{19} corner sites was probed by halogen adsorption.[7]

8.2 Future directions

As mentioned, one key endeavor of this project is to eventually model a real system. This is a challenging endeavor because modelling the real system requires a completely explicit solvation environment. Although DFT can provide the most accurate calculations, one of the shortcomings is that its implementation is limited to small model systems. To circumvent this, CMD methods can scale to very large systems containing large amounts of water molecules. However calculations require careful parameterization of interatomic force fields. Despite these differences, utilizing the combination of the two computational methods permits the further quest to continuing addressing intermediate steps to the real model system.

First, one chemical importance of amidoxime-type ligands is protonation state of binding uranyl-AO-type ligands in seawater related environments. There is a confusing amount of work inconsistently modeling amidoxime protonation states. The next step is to

address dominant protonation states to encourage common consensus. Currently, it is suggested, given the relatively high pK_a of 13 for amidoxime, that protonation (R-C=N-OH) occurs before displacement. In short, the protonated oxime-oxygen hydrogen protonates a binding uranyl-carbonate specie to initiate carbonate displacement, with a subsequent dissociated calcium carbonate ($CaCO_3$).[8] Even after binding what is the dominant tautomerized form resulting uranyl-AO specie in seawater related waters? Explicit DFT modeling provides the most accurate results, but is challenging because it requires very expensive quantum computational calculations to model bonds breaking in a solvated system that requires at least need 100 or so explicit water molecules in order to treat the entire system quantum mechanically. Sampling a system to model the tautomerization of a hydrogen transfer can present convergence issues that yield unreasonable results. One way to circumvent this is to treat the system as a combination of explicit and implicit modeling. An example would be to provide a first hydration shell of water molecules into a cavity that represents the continuum of water molecules beyond the first hydration shell.

Second direction for this project is to move from small molecule models to larger oligomer models as to take another step towards investigating coordination in polymer systems and oligomer-oligomer influence on the system. Devising longer chain models containing open, cyclic, and carboxylate functional groups at different rations, like 1:1:2, can provide a deeper insight to the chemical behavior of neighboring interactions upon binding uranyl. It would be interesting to observe the chemical influence on coordinating uranyl-oligomer systems by arranging the different functional groups in different

combinations. It would also be interesting to pry into how oligomer-oligomer interactions influence the binding behavior. CMD-based calculations would be the most appropriate direction, as this model is outside the scope for DFT-type calculations. One will need to utilize sampling methods with defined collective variables to express the coordination of uranyl-oligomer interface for a single and dimer base oligomers.

Along that same notion, one of the properties impeding uranium uptake is lack of diffusion through the polymer system. Continuing from the previous notion of devising oligomer models, one can devise polymer containing blocks or regions containing concentrated amounts of AO-types and Ac functional groups. For exampling, a model can be devised to contain AAA-BBB to study $Ca_2[UO_2(CO_3)_3]$ diffusion of the dominant uranium and vanadium specie comparatively diffuses through an oligomer model. This can bring insight to influences of diffusion and explore ways to increase uranium diffusion. The diffusion behavior can be calculated with mean-square-distance MSD analysis along with binding profile with umbrella sampling. Different oligomeric models can be devised to explore polymeric terminal influence along with internal influence based on block-functional groups. Perhaps terminal ends require a block of bulky or non-bulky hydrophilic groups to open terminal sights for diffusion. It would be interesting to investigate how hydrophilic groups influence uranium uptake with oligomeric-AO based models.

Other polymeric systems have been studied experimentally, but not computationally, suggesting that advances towards developing prospective functionals also needs to be explored. For example, a renewable biopolymer called chitin has been investigated for the past few years experimentally, yet very little computationally.[9] Chitin

is a long-chain polymer of N-acetylglucosamine, which is a derivative of glucose, and is the primary component in exoskeletons of crustaceans like crabs, lobster, and shrimp. Its structure is comparable to another polysaccharide, cellulose. Computational research on uranyl-chitin interactions can be done with CMD software packages, such as AMBER. One unique feature of AMBER is the glycam force fields, which are predetermined force fields devised for the package, making designing polysaccharides feasible. For example, one can devise a cellulose-like model from the monosaccharide, glucose. In fact, many of the computational methods can be applied to investigating uranyl-chitin based systems by calculating binding free energies using umbrella sampling. These are uncharted waters for a computational chemist and seems like and ideal direction to take for a future thesis project.

Computationally extending research towards uranium recovery from seawater is endless. Many intermediate theoretical questions still remain, such as: how and does tautomerization happens before and after binding of uranyl-AO systems, what are the coordination influence of uranyl-oligomer based systems, and are there better polymers to utilize, like chitin? This work provides a benchmark of computational methods that can be utilized and extended for future work on the recovery of uranium from seawater.

8.3 References

1. Priest, C.; Tian, Z. Q.; Jiang, D. E. First-principles molecular dynamics simulation of the Ca2UO2(CO3)(3) complex in water. Dalton Trans. 2016, 45 (24), 9812-9819 DOI: 10.1039/c5dt04576b.

2. Wu, W. H.; Priest, C.; Zhou, J. W.; Peng, C. J.; Liu, H. L.; Jiang, D. E. Solvation of the Ca2UO2(CO3)(3) Complex in Seawater from Classical Molecular Dynamics. J. Phys. Chem. B, 2016, 120 (29), 7227-7233 DOI: 10.1021/acs.jpcb.6b05452.

3. Li, B.; Zhou, J. W.; Priest, C.; Jiang, D. E. Effect of Salt on the Uranyl Binding with Carbonate and Calcium Ions in Aqueous Solutions. J. of Phys. Chem. B 2017, 121 (34), 8171-8178 DOI: 10.1021/acs.jpcb.7b04449.

4. Priest, C.; Li, B.; Jiang, D. E. Uranyl-Glutardiamidoxime Binding from First-Principles Molecular Dynamics, Classical Molecular Dynamics, and Free-Energy Simulations. Inorg. Chem. 2017, 56 (16), 9497-9504 DOI: 10.1021/acs.inorgchem.7b00711.

5. Li, B.; Priest, C.; Jiang, D. E. Displacement of carbonates in Ca2UO2(CO3)(3) by amidoxime-based ligands from free-energy simulations. Dalton Trans. 2018, 47 (5), 1604-1613 DOI: 10.1039/c7dt03412a.

6. Priest, C.; Zhou, J. W.; Jiang, D. E. DSolvation of the vanadate ion in seawater conditions from molecular dynamics simulations. Inorg Chim Acta 2017, 458, 39-44 DOI: 10.1016/j.ica.2016.12.027.

7. Priest, C.; Tang, Q.; Jiang, D. E. Structural Evolution of Tc-n (n=4-20) Clusters from First-Principles Global Minimization. J. Phys. Chem. A, 2015, 119 (33), 8892-8897 DOI: 10.1021/acs.jpca.5b04015.

8. Wang, C. Z.; Lan, J. H.; Wu, Q. Y.; Luo, Q.; Zhao, Y. L.; Wang, X. K.; Chai, Z. F.; Shi, W. Q. Theoretical Insights on the Interaction of Uranium with Amidoxime and Carboxyl Groups. Inorg. Chem, 2014, 53 (18), 9466-9476 DOI: 10.1021/ic500202g.

9. Bandomir, J.; Kelley, S.; Shamshina, J.; Gurau, G.; Rogers, R. Homogeneous blending of chitin with biopolymers for advanced biodegradable sorbents for uranium extraction from seawater. Abstr. Pap. Am. Chem. S 2015, 249.